Ultraschallthermoformen

Ultrasonic Thermoforming

Von der Fakultät für Maschinenwesen der Rheinisch-Westfälischen Technischen
Hochschule Aachen zur Erlangung des akademischen Grades eines Doktors
der Ingenieurwissenschaften genehmigte Dissertation

vorgelegt von

Yujiang Peng

Berichter: Universitätsprofessor Dr. rer. nat. Werner Karl Schomburg
apl. Prof. Dr.-Ing. Uwe Schnakenberg

Tag der mündlichen Prüfung: 25. 08. 2021

Acknowledgements

First, I would like to express my deepest gratitude to my advisor, Professor Werner Karl Schomburg, for his support and patient guidance, helping me to complete my doctoral study. I am grateful for spending time under his mentorship, and his model role also helps to shape my attitude in research and life.

I also thank Professor Uwe Schnakenberg and Professor Andreas Jupke for taking on the second review and chairing the examination.

I would like to thank our former senior engineer Dr. Johannes Sackmann, the current and former doctoral students Andreas, Felix, Julia, Wei, Sönke, and our secretary Mrs. Inge Schleiden and workshop manager Mr. Thomas Janhsens. I really appreciate their help and support during my study at RWTH. I have learned a lot from the discussions with them on the research and culture. Special thanks to Mr. Janhsens for his support on technique works and cooperations throughout my doctoral study. Many thanks to Chong, Ruiqi, Chunhao, Zhexin, Yanru, and Ruya for their contributions to this work. I thank all the friends met at Aachen, and I really enjoy the numerous hours we spent.

Last but not the least, I would like to gratefully thank my supportive parents and family. Thousands of miles away, I can still feel their love and care. Without their support and encouragement, I could not have made it through my doctoral study.

Zusammenfassung

Ultraschallthermoformen ist ein neues Verfahren zur Herstellung dreidimensionaler Mikrostrukturen aus theromplastischen Kunststoffen. Diese Dissertation konzentriert sich auf die Grundlagen des Verfahrens. Andere Ultraschallfertigungsverfahren werden auch diskutiert.

Beim Ultraschallthermoformen werden Polymerlagen zwischen zwei Werkzeugen eingeschlossen und durch Ultraschallschwingungen erwärmt. So passt sich das Polymer Mikrostrukturen auf den Werkzeugen innerhalb von Sekunden an.

Im ersten Teil dieser Arbeit werden grundlegende Untersuchungen des Ultraschallthermoformens beschrieben. Testwerkzeuge mit Mikrostrukturen unterschiedlicher Formen und Kantenverrundungen wurden entworfen, um das Prozessfenster und die Grenzen des Verfahrens zu ermitteln. Die Abmessungen der hergestellen Mikrostrukturen wurden mit denjenigen der Werkzeuge verglichen. Dabei wurde kein offensichtlicher Schrumpf des Polymers festgestellt.

Die Experimente zeigten, dass feste Werkzeuge aus Aluminium besser geeignet sind als solche aus weicheren Materialien, weil das Prozessfenster dann viel größer ist. Besonders dünne Folien im Bereich von 16 bis 20 µm wurden erfolgreich mit Werkzeugen aus festem Material umgeformt, indem Pufferfolien auf die Werkzeuge platziert wurden.

Die Messungen zeigten, dass das an der Sonotrode befestigte Werkzeug einige 10 °C wärmer wurde als das auf dem Amboss angebrachte. Beide Werkzeuge wurden mehrere °C wärmer, wenn das Werkzeug mit den konvexen Mikrostrukturen an der Sonotrode anstatt auf dem Ambuss befestigt war. Beide Werkzeuge waren in ihrer Mitte einige °C wärmer als an ihrem Rand. Die Temperatur der thermogeformtn Folien war ungleichmäßg verteilt, korreliert mit der Form der Mikrostrukturen.

In weiteren Untersuchungen wurden elektrische Bauteile in mit Ultraschll gefertigte Mikrosysteme integriert. Mikrokanäle mit unterschiedlichen Abmessungen, Geometrie und Anschlüssen wurden erfolgreich in Folien (3 × 5 cm) aus PET-G thermogeformt. LEDs wurden durch Ultraschallverschweißen mit einer ebenen Folie darin integriert. Außerdem wurde ein Mikroflusssensor durch das Verschweißen zweier halbzylindrisch geformter Kanäle hergestellt. Dieser Sensor wurde mit drei Arten von Flüssigkeiten getestet.

Außerdem wurde eine Linse mit verstellbarem Fokus hergestellt, indem drei Folien mit Ultraschall in einem einzigen Schritt thermogeformt, geprägt und gestanzt wurden. Nach der Füllung mit Wasser wurde der Fokus durch das mit einer integrierten Spule erzeugte Magnetfeld verändert.

Im letzten Teil der Arbeit wurden Mikromembranen aus einer einzigen Lage PEEK bzw. durch Verschweißen mit einer thermogeformten Folie hergestellt. Ihre Resonanzfrequenzen wurden gemessen und analysiert.

Abstract

Ultrasonic thermoforming is a novel process to generate three-dimensional micro structures in the production of thermoplastic microfluidic systems. This thesis focuses on basic investigations of thermoforming with ultrasound. Ultrasonic fabrication techniques are also discussed.

For ultrasonic thermoforming, polymer layers are enclosed between two tools and heated up by the vibrations of ultrasound. This way, the polymer adapts to micro structures on the tools within seconds.

In the first part of this thesis, basic investigations of ultrasonic thermoforming were launched. Test tools were designed containing micro structures of varied shapes and edge roundings to find out the process window and to better understand the limits of ultrasonic thermoforming. The dimensions of the micro structures fabricated by ultrasonic thermoforming were measured and compared to the dimensions of the tool. No obvious shrinkage of the polymer caused by the process was observed.

Experiments showed that rigid tools from aluminum are superior compared to tools from softer material. When using a rigid tool, the process window is much larger. Extra thin foils, 16 to 20 μm in thickness, were successfully thermoformed by a rigid tool with the aid of buffer foils.

Measurements showed that the tool fixed on the sonotrode got tens of degrees hotter than the one fixed on the anvil. Both tools got several degrees hotter if the tool with convex microstructures was fixed on the sonotrode compared to fixed on the anvil. On each tool, the temperature in the center was generally higher than in the surrounding area and the difference was about several degrees. The temperature of the thermoformed foils was not homogeneously distributed; it correlated to the shape of the structures.

In further developments, electrical elements were integrated into ultrasonically fabricated microsystems. Micro channels and cavities with different dimensions, geometry, and connection were successfully thermoformed into PET-G foils (3 × 5 cm). LEDs were integrated into it by ultrasonic welding with a flat foil. Furthermore, a micro flow sensor with a cylindrical flow channel was fabricated by welding two semi-cylindrical channels onto each other. The flow sensor was tested with three kinds of liquids.

Additionally, a variable focus lens was fabricated. Three foils for the lens were ultrasonically fabricated in a single step by combining ultrasonic thermoforming, ultrasonic hot embossing, and ultrasonic punching. After filling with pure water, the focal length of the lens was varied according to the magnetic field generated by an integrated coil.

In the last part of this thesis, single-layer PEEK microdiaphragms and composite microdiaphragms were fabricated by ultrasonic thermoforming and welding. Their resonance frequencies were successfully measured and analyzed.

Content

Abbreviations

The abbreviations in this thesis are listed in the following table:

PE	Polyethylene
PEEK	Polyether ether ketone
PET-G	Poly (ethylene terephthalate glycol)
PDMS	Polydimethylsiloxane
PP	Polypropylene
MC-30	30 µm-wide micro channel
MC-60	60 µm-wide micro channel
MC-100	100 µm-wide micro channel
MC-200	200 µm-wide micro channel

Notations and symbols

The symbols from equations in this thesis are listed in the following table:

Symbols	Definition	Unit
A	Vibration amplitude	µm
A_c	Cross-sectional area of flow channel	mm^2
a_M	Length of microdiaphragm in x-direction	mm
b_M	Length of microdiaphragm in y-direction	mm
d	Thickness of foil	µm
d_a	Wall thickness	µm
d_c	Thickness of the lens chamber without deflection of the lens membrane	mm
d_L	Aperture of the lens	mm
d_M	Thickness of the membrane	µm
D_c	Distance between the end of the heater coil and the mid of the sensor wire 1	Mm
D_{cs}	Distance between the heater coil and sensor wire 1	mm
D_f	Diameter of flow channel	mm
E''	Loss modulus	GPa
E_M	Young’s modulus of membrane	GPa
E'_w	Elastic modulus	GPa
f	Focal length	mm
f_{res}	Fundamental resonance frequency	Hz
F_w	Static compression force	N

h	Deflection at the center of the lens membrane	mm
h_c	Height of micro channel	μm
L_c	Length of the heater coil	mm
L_s	Length of sensor wire	mm
L_i	Initial length of foil	mm
n_a	Refractive index of air	
n_w	Refractive index of water	
N	Normal stresses	N
N_d	Dynamic components of normal stresses	N
N_s	Static components of normal stresses	N
r	Radii of curvature of the lens membrane	mm
R	Radii of convex spherical surface on the foil-3	mm
Re	Reynolds number	
s_0	Length of temperature maximum	mm
S_w	Contact area of thermoplastic parts to be joined	mm^2
t_h	Heating duration	s
t_{hf}	Cumulated heating time	s
T_{hf}	Temperature of heated flow	°C
Q	Average heating rate	°C/s
Q_f	Flow rate	ml/h
t_w	Total thickness of welding parts	mm
v	Flow velocity	mm/s
v_M	Poisson's ratio of membrane	
w_c	Width of micro channel	μm
α	Inclination angle	°
Δt_0	Time between the end of the heater pulse and zero crossing	s
Δt_{Max}	Time between the end of the heater pulse and maximum	s
ϵ	Cyclic strain imposed in material	
θ	Angle of the deformed lens membrane	°
μ	Viscosity	Pa·s
ρ	Density	g/cm^3
ρ_M	Density of membrane	g/cm^3
σ_a	Stress of microdiaphragm in x-directions	Pa
σ_b	Stress of microdiaphragm in y-directions	Pa
σ_n	Dynamic stress generated by ultrasonic vibrations	Pa
ω	Vibration frequency	Hz

1. Introduction

Thermoforming is a process in which a polymer foil is softened and deformed over a mold into the desired shape by applying appropriate heating and adequate pressure [1-3]. This process requires a cycle time of up to several minutes to control the mold temperature effectively. Recently, ultrasonic vibration energy has been used as a direct energy source to fabricate microsystems from thermoplastic polymers [4-11]. Ultrasonic thermoforming is a production technique that utilizes ultrasonic vibration to thermoform polymer foils with bilateral structures [9, 10, 12, 13]. It is relatively new and unexplored.

Up to now, there are only limited investigations on the process of ultrasonic thermoforming [12, 14]. The possible shapes and designs of the polymer foil are predetermined by the kind of polymers employed, the thickness of the foils, the design of the tool and the process parameters [15, 16]. The influences of these parameters are not fully understood; therefore further investigations have to be done to generate guidelines for molding polymer foils by ultrasonic thermoforming. Besides, little was known about the influence of the hardness and the installation locations of the tools on the ultrasonic thermoforming and how these processes can be favorably influenced by their use. Some related research will be briefly presented in the following chapter [17]. It is known that the energy absorption and heating below a sonotrode are inhomogeneous on the order of 50% [18]. Therefore, a large process window is required especially if large products are to be thermoformed. It is also important to know the temperature distribution of tools and thermoformed foils.

When two thermoformed foils are welded together, microfluidic channels can be manufactured. For this, it is necessary to find out appropriate parameters for ultrasonic welding of thermoformed polymer foils [19, 20]. Usually, the thermoformed foils have protruding structures on one or both sides and therefore they cannot be welded by the sonotrode directly. Otherwise, the micro structures can deform or be damaged, and micro channels are blocked. Besides, the micro structure need to be aligned if there are micro structures on the thermoformed foil to be welded.

The aim of the present work was therefore to reveal the principal mechanism of ultrasonic thermoforming and further determine its guidelines as well as the reproducibility of the process. Furthermore, a subsequent ultrasonic welding process for the production of sealed micro devices/systems was the topic. The aim was to develop guidelines and suggestions for improving the ultrasonic fabrication from the knowledge gained.

To investigate the ultrasonic thermoforming process, the basics must first be understood. This includes the experimental setup, process windows, and wall thickness distribution of ultrasonically thermoformed foils. Based on this, a guideline of tool designing, choice of tool type, and influence of tools' install locations are determined to accommodate different requirements for each specific application.

To do this, it was necessary to carry out some basic investigations. The influences of parameters were examined by determining process windows. The wall thickness distributions of ultrasonically thermoformed foils were investigated, and guidelines of tool design were derived. The capabilities of rigid and flexible tools in thermoforming amorphous poly (ethylene terephthalate glycol) (PET-G) foils and semi-crystalline polypropylene (PP) foils were compared. The influences of the installation location of tools were also presented by comparing their process windows and the temperature distribution of tools and thermoformed foils. In the rest of this thesis, some application examples of micro devices/systems are presented, and their fabrication process is put in the context of the knowledge gained in the previous parts.

2. State of the art

Ultrasonic thermoforming employs ultrasonic welding machines already known for decades to join metal and polymer parts [21]. Therefore, the principle of these machines and the heating mechanism are introduced here. Ultrasonic hot embossing is another process employing ultrasonic welding machines to produce micro structures, and therefore, it is described here besides the ultrasonic thermoforming process already known before the work of this thesis started. Besides this, some microsystems fabricated by ultrasonic fabrication are shown.

2.1 Ultrasonic welding system

Ultrasonic welding systems (Figure 2.1) [22] consist of three main components: the generator, the oscillating structure, and a (pneumatic) drive module. The generator converts electrical energy of 50 Hz into output frequency in the range between 20 kHz and 70 kHz. The actual working frequency of the generator depends on the resonance frequency of the vibrating structure. Utilizing the inverse piezoelectric effect, the converter of the oscillation structure converts this electrical oscillation into mechanical longitudinal vibration and transfers it to booster and sonotrode. The drive module provides the contact pressure between sonotrode and workpiece, which in turn is attached to the anvil of the machine.

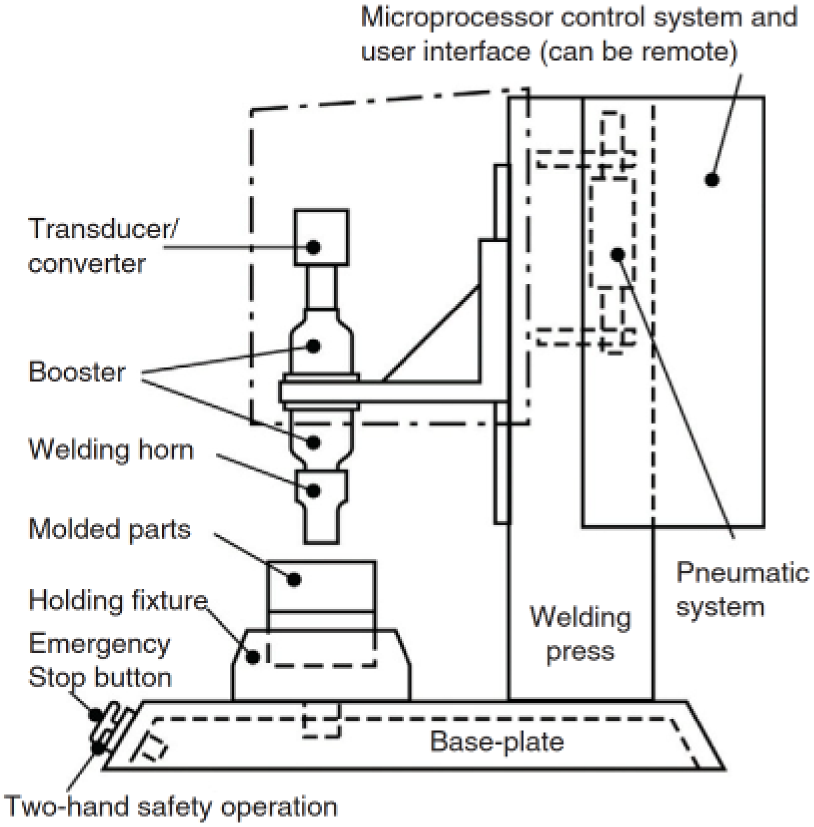

Figure 2.1: Schematic representation of a commercially available ultrasonic welding machine [22].

2.1.1 Theory of energy transfer and conversion

The ultrasonic welding system transmits high-frequency mechanical vibration to the joint interface of thermoplastic parts to be joined, together with a static compression force. When ultrasonic vibrations are transmitted perpendicular to a thermoplastic material, sinusoidal standing waves are generated in that material. A part of this energy is transmitted to the interface where boundary friction provides localized heating, and another part is dissipated through intermolecular friction leading to viscoelastic heating, resulting in heat accumulation in the bulk material [22, 23].

The interfacial frictional heat is the primary heating source of thermoplastic parts from their initial temperature to glass transition temperature [23, 24], whereas the viscoelastic heating dominates after some regions of the polymer reached the glass transition temperature. Viscoelastic heating is a significantly faster heating mechanism and provides the main heat during the welding process. The heat generated by interfacial friction is vital to start the welding process. At this stage, heat is mostly generated at the highly strained joint interface due to surface asperities. When the temperature of some regions on the thermoplastic part reaches the glass transition temperature, the intensive viscoelastic heat is activated.

Evidently, the total heating is a combination of localized heating near the interface and the volumetric dissipation over the entire pressed region of the thermoplastic part. The following are individual contributions of these two mechanisms to the heating during welding.

The heat generated by interfacial friction depends on normal stresses (N) at each region of welding interfaces, which can be divided into its static and dynamic components, N_s and N_d, respectively. Normal stresses can be determined from the following equation:

$$N = N_s + N_d = \frac{F_w}{S_w} + \sigma_n \qquad (2\text{-}1)$$

where F_w is the static compression force (welding force), S_w is the contact area of thermoplastic parts to be joined, and σ_n is the dynamic stress generated by ultrasonic vibrations. A lower bound for the dynamic normal stress can be calculated by considering a vertical uniform sinusoidal deformation leading to the following inequality [25]:

$$\sigma_{\mathrm{n}} > \frac{A \cdot E'_w}{t_w} \qquad (2\text{-}2)$$

where A is the vibration amplitude, E'_w is the elastic modulus of the welding part, and t_w is the total thickness of welding parts. The dynamic normal stress is significantly higher than static ones at ultrasonic welding of thermoplastic parts with typical welding force and vibration amplitude [25]. In an ideal welding process in which the sonotrode permanently contacts the top welding part, the vibration amplitude is expected to make more contribution to the overall heat generation than the welding force.

The viscoelastic heating rate can be described by the following equation [23]:

$$Q = \frac{\omega \cdot \varepsilon^2 \cdot E''}{2} \tag{2-3}$$

The average heating rate Q is dependent on the frequency of the vibration ω, the cyclic strain imposed in the material (ϵ) which is directly related to the amplitude of the vibration, and the loss modulus of the material (E''). When a viscoelastic material is subjected to ultrasonic oscillations, the volumetric dissipation can cause significant internal temperature rises over longer times [23].

These equations provide limiting cases of the heat produced at the interface and the heat generated by intermolecular friction throughout the pressed region of the thermoplastic part.

2.2 Ultrasonic welding

Ultrasonic welding uses ultrasonic vibration to generate heat at the joint interface of the parts being welded, resulting in the melting of the thermoplastic materials and weld formation after cooling [9, 22].

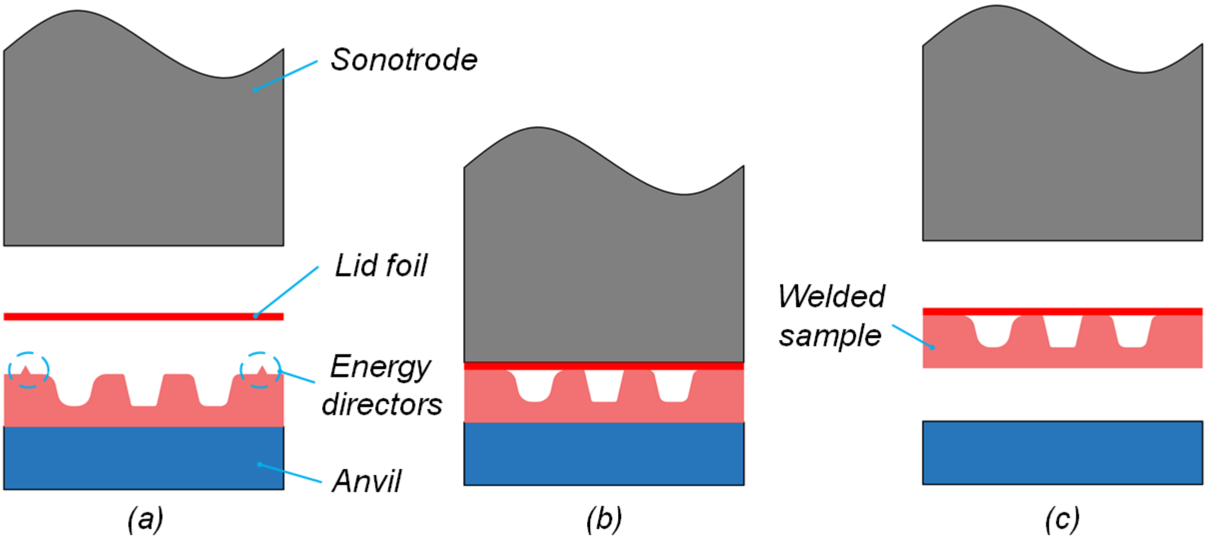

Figure 2.2: Ultrasonic welding process.

The ultrasonic welding process consists of three phases [19] (Figure 2.2). (i) Build up phase. In this phase, the sonotrode contacts and gradually applies an increasing force onto the parts to be joined until the predefined force is build up, which is the so-called trigger force. No vibration is applied during this phase. (ii) Vibration phase, in which an ultrasonic vibration with constant amplitude and frequency is coupled into the parts to be joined via the sonotrode, generating heat to melt and mix the material of the parts to be joined. The ultrasonic vibration is maintained until a predetermined criterion is reached. This criterion can either be the welding time, welding path, or welding energy. (iii) Consolidation phase. After the ultrasonic vibration has ended, the parts cool down under a prescribed force for a certain time.

The parameters that govern the heat generation in the ultrasonic welding process are the welding force, vibration amplitude, duration of the vibration phase (welding time, welding path, or welding energy), and vibration frequency. Among these parameters, welding force, welding amplitude, and duration of the vibration phase are variable. It should be noted that welding frequency is fixed for each specific ultrasonic welding machine.

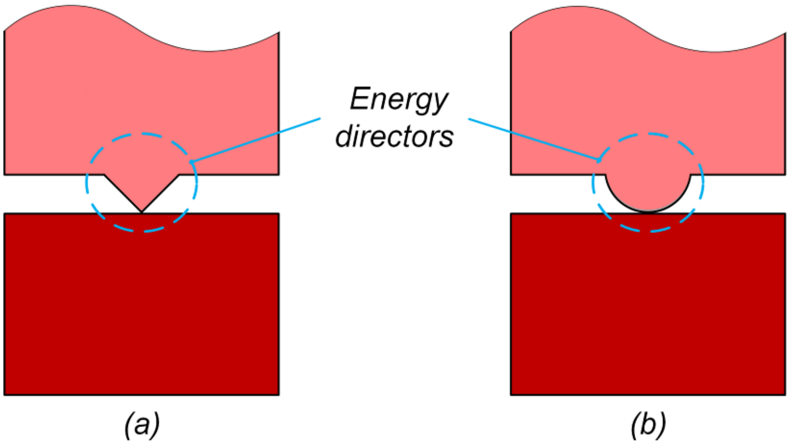

Figure 2.3: Energy directors.

Energy directors (Figure 2.3) are used to concentrate heat generation at the welding interface, causing surrounding polymers to melt and finally creates a welded joint. In ultrasonic welding of thermoplastic parts, energy directors are typically molded on the parts to be joined as raised structures of different size and geometry. Typical energy director shapes are triangular, rectangular, and semicircular.

2.3 Hot embossing

If micro structures shall be generated on a substrate, besides injection molding and injection compression molding, hot embossing is a process often employed. A layer of thermoplastic polymer is placed onto a so-called mold insert showing micro structures on its surface. The polymer is heated up together with the mold insert and a tool in which it is mounted and the polymer softened that way is pressed onto the mold insert adapting to the micro structures on its surface. Then, the tool is cooled down, and after it got hard again, a polymer part with the desired micro structures on its surface is demolded from the mold insert. The cycle time of hot embossing micro structures is on the order of minutes because the entire tool needs to be thermally cycled.

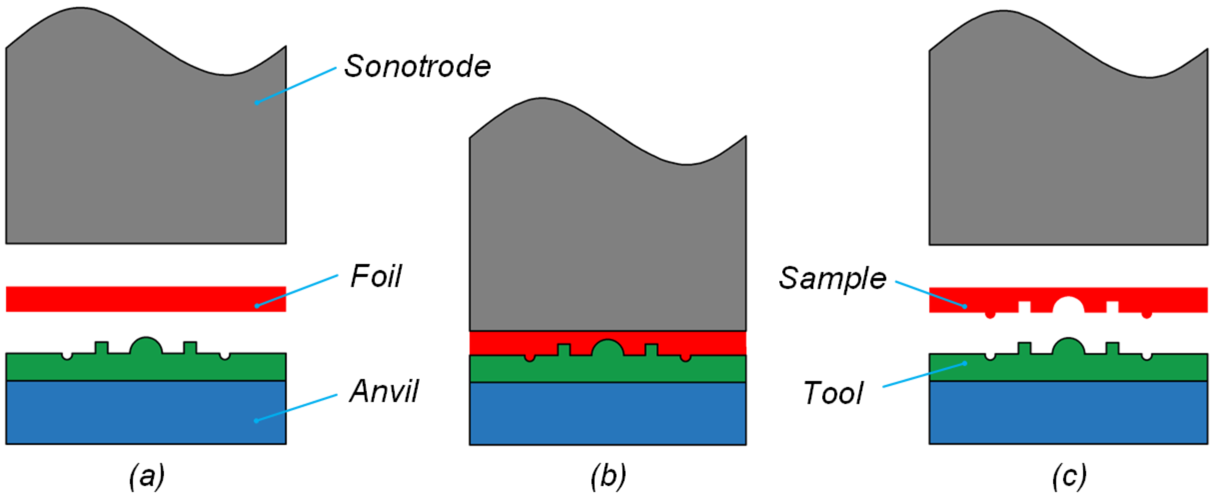

Figure 2.4: Ultrasonic hot embossing.

It has been shown that the cycle time of hot embossing micro structures from thermoplastic polymers can be shortened to some seconds if the polymer is heated by ultrasonic vibrations instead of heating up the entire tool [9, 17, 26-29], as shown in Figure 2.4. Obviously, the polymer is held longer at an elevated temperature even when it gets into contact with a cold tool. Nevertheless, preheating of the tool to an elevated temperature during ultrasonic hot embossing results in better mold filling and the cycle time is not prolonged significantly [9].

2.4 Thermoforming

Thermoforming is a well-known process and applied in industry for the forming of thermoplastic polymer layers, approximately thinner than 2 mm [1, 2]. Typically, this process is employed to fabricate the packaging of sweets or tablets. As shown in Figure 2.5, a foil or thin plate from a thermoplastic polymer is first clamped and softened by heating. Then, pre-stretched by hot gas and adapted onto the surface of a mold with vacuuming. Then the polymer is cooled down and solidifies again in the shape of the mold surface.

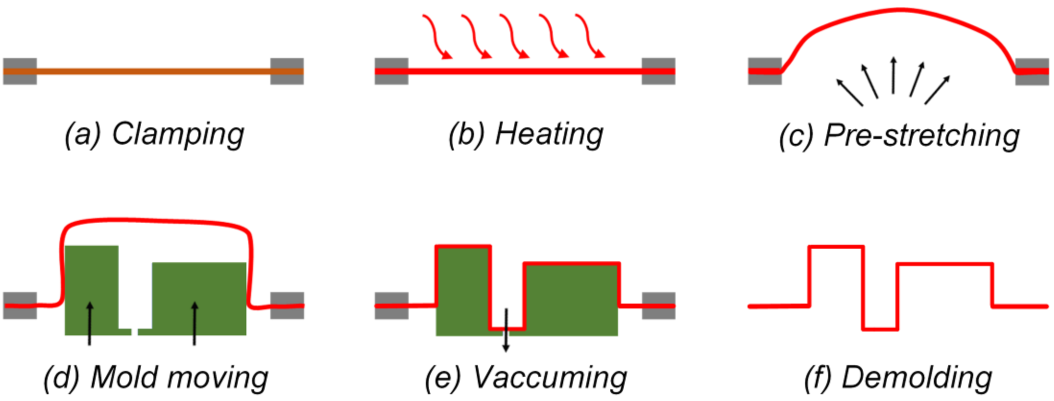
(a) Clamping *(b) Heating* *(c) Pre-stretching*

(d) Mold moving *(e) Vaccuming* *(f) Demolding*

Figure 2.5: Thermoforming process.

Since 1999 several working groups have been showing to which extend thermoforming can also be applied for generating micro structures on polymer layers [3, 15, 16, 28, 30-37]. The cycle times of these processes are on the order of some minutes because the entire tool needs to be heated up to the softening temperature of the thermoplastic foil before the forming stage and cooled down again below that temperature for proper demolding after the forming stage. The heating up of the tool is required because the polymer flow shall not be stopped before it arrives in micro cavities.

Ultrasonic vibration energy has been used for heating and softening polymer in a variety of polymer fabrication processes [9]. It can be a direct energy source [14, 38] or an auxiliary heat source [4, 18, 39, 40] to fabricate micro structures on thermoplastic polymers.

2.5 Ultrasonic Thermoforming

As with ultrasonic hot embossing, ultrasonic vibration energy can also be utilized in the thermoforming process as a direct energy source or an auxiliary heat source. Researches show that ultrasonic thermoforming of micro structures is also possible and the cycle time is also as short as some seconds. [6, 9, 13, 14, 18, 38, 39, 41, 42].

A micro-speaker diaphragm that incorporates rectangular bands and a number of micro-corrugations was thermoformed by using ultrasonic vibration energy [13, 14, 38, 42]. This was realized either without additional heating, or with tool heating by inserted cartridge heaters and foil heating by an infrared lamp. It turned out that the shapes of samples thermoformed with heating corresponded more to the tool than those fabricated without heating.

To ensure well absorption of ultrasonic vibration in a very thin film (e.g., with a thickness of tens of micrometers) and prevent damage of the films, flexible tools made from silicone elastomer were employed as counter tools instead of metal tools. Two types of flexible tools, a flat tool and a curved flexible tool with the inverse of the desired shape of the diaphragm, were compared. Results showed that the curved tool is better in its heating capability and formability. The effect of the installation location of the flexible tool (i.e., whether the flexible tool is installed on the sonotrode or the anvil) was investigated. Results showed that a superior formability and heating capability were provided when the flexible tool was installed on the sonotrode compared to on the anvil. This ultrasonic thermoforming process was estimated to shorten the cycle time of conventional thermoforming from over 160 s to less than 20 s.

Besides, micro patterns were developed on a curved thermoplastic surface by combining ultrasonic hot embossing and thermoforming [39]. This can be achieved in a single step using ultrasonic thermoforming.

Both temperature and pressure distribution during ultrasonic hot embossing was measured inside of a stack of thermoplastic polymer foils by employing polyvinylidene fluoride sensor foils [18]. From the data measured in the lateral direction below a sonotrode with outer dimensions of 8 × 12 cm, the difference in temperature change and ultrasonic pressure are about 12°C and 4 kPa, respectively. Ultrasonic thermoforming is a novel process and it is a variant of ultrasonic welding, like ultrasonic hot embossing. Knowledge in ultrasonic hot embossing may also be applicable and helpful for ultrasonic thermoforming.

2.5.1 Types of ultrasonic thermoforming

Ultrasonic thermoforming is a production technique that allows thermoplastic films to be formed. It can be carried out on a commercially available ultrasonic welding machine. A pair of tools is needed for ultrasonic thermoforming, the desired micro structures have to be patterned on the surface of one tool, whereas the counter tool can be either flexible or rigid. Thus, the ultrasonic thermoforming processes can be distinguished by types of counter tools.

The counter tool can be made from flexible materials such as silicone elastomer or a stack of polymer foils from a polymer which cannot be welded together with the foil to be thermoformed [9, 42].

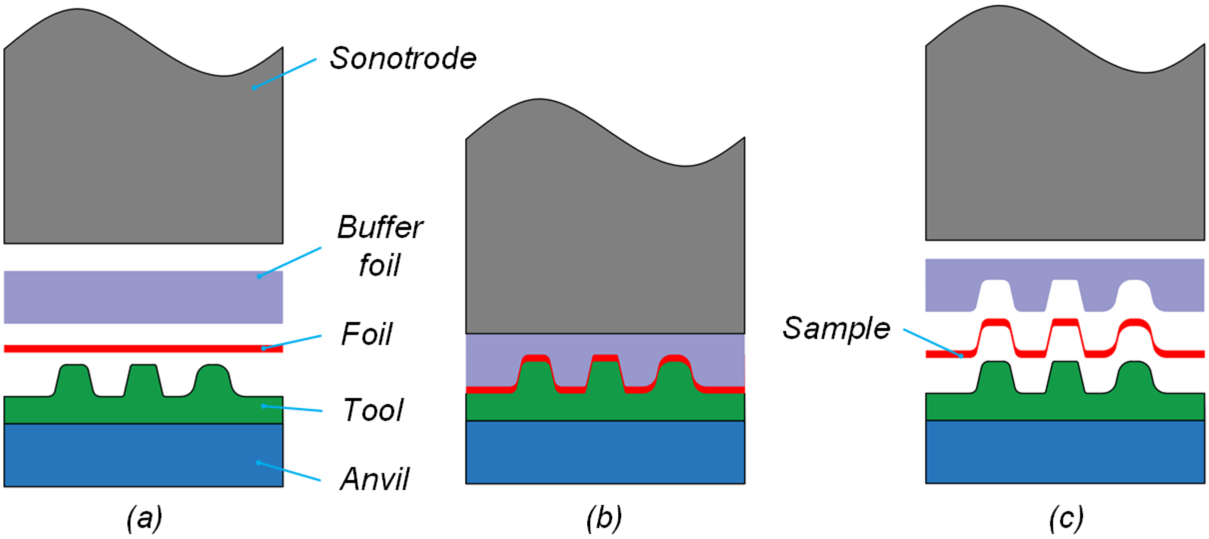

Figure 2.6: Ultrasonic thermoforming by using a buffer foil as a mold.

For ultrasonic thermoforming using buffer foils as a flexible tool (Figure 2.6), a combination of non-weldable polymers is used [9, 18]. A thin foil (e.g., polyether ether ketone (PEEK)) to be thermoformed and a stack of buffer foils (e.g., polyethylene (PE)) are placed between the tool and the sonotrode. When ultrasonic vibrations are applied, the thin foil is thermoformed and buffer foils are embossed by ultrasonic vibrations (Figure 2.7). Afterwards, buffer foils may be discarded or used for another purpose.

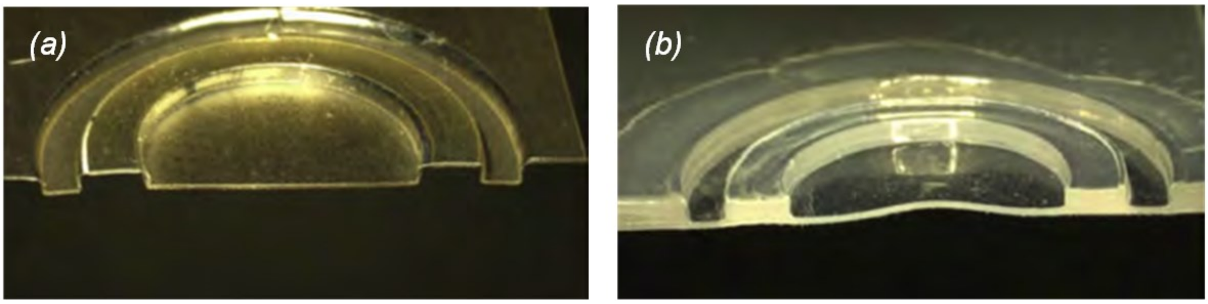

Figure 2.7: Cuts through an ultrasonically thermoformed PEEK-foil (a) and embossed PE-buffer foils (b) [10].

Buffer materials like silicone elastomer can also be used as a flexible counter tool, either with or without the inverse of desired micro structures [13, 42]. This type of flexible tool is reversely deformed after ultrasonic thermoforming. The tool with inverse micro structures provides better heating capability than a flat tool, due to the ultrasonically induced deformation and friction were more focused in the curved region than the flat region [42]. But this also leads to a concentration of the ultrasound in a single spot resulting in a rupture of the thermoformed foil [9]. Flexible tools are especially suitable for the ultrasonic thermoforming of very thin foils (e.g., with a thickness of tens of micrometers), which is too thin to absorb the ultrasonic vibration whose amplitude is only 1 to 25 µm.

If rigid tools are used for ultrasonic thermoforming, a foil from a thermoplastic polymer is placed between an upper and a lower tool (Figure 2.8a), both with micro structures on their surfaces facing the foil. Micro structures on the upper tool are the inverse of those on the lower tool.

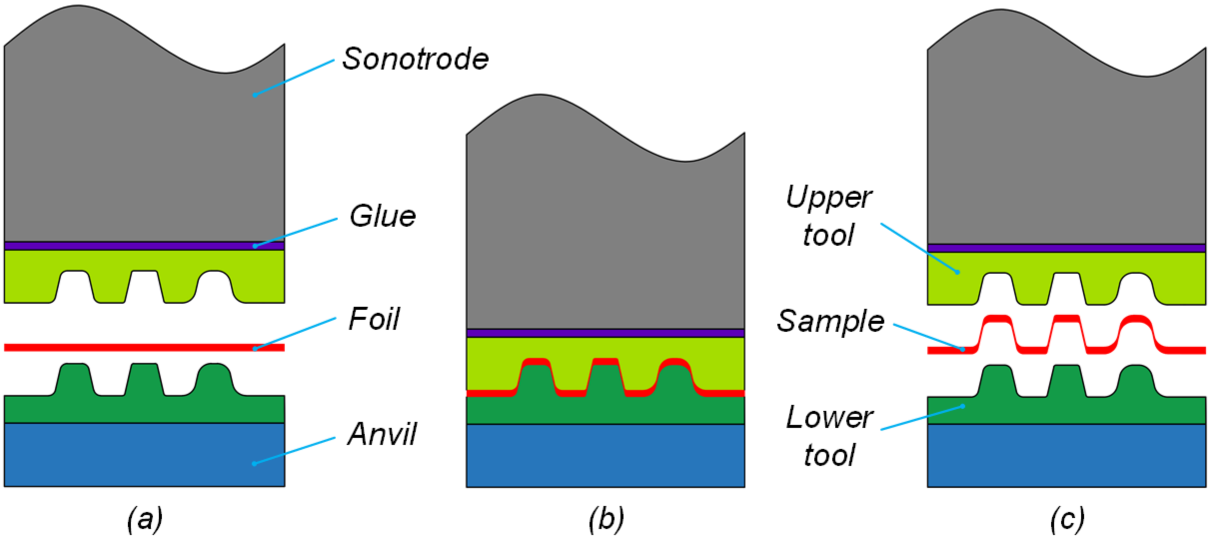

Figure 2.8: Ultrasonic thermoforming with a counter tool.

The sonotrode of an ultrasonic welding machine is pressing the upper tool down onto the foil, and ultrasonic vibrations start when a pre-set pressing force, the so-called trigger force, is reached. The polymer foil is heated up by the friction generated by ultrasonic vibrations and adapted to the shape of the lower and upper tool (cf. Figure 2.8b). Vibrations are stopped after a few seconds and the pressure is retained for some more seconds, the so-called cooling time, to allow for heat dissipation into tools. After the polymer got cold enough and hardened again, the foil is removed from the tools in its new shape (Figure 2.8c).

2.5.2 Fixing methods of tools to the sonotrode

The tools used for ultrasonic thermoforming consist of two separate parts, they need to be fixed on anvil and sonotrode, respectively. Since the ultrasonic vibration is powerful, researchers have figured out several methods to fix the tool on the ultrasonic sonotrode. Typical fixing methods are using double-sided tape, adhesive agent, screw clamping, cooling fit, silver brazing, and direct milling into the faying surface of the ultrasonic sonotrode [17]. Cooling fit means that the tool is first cooled down by dipping into liquid nitrogen. Then, the shrunken fitting parts on the tool are inserted into grooves on the sonotrode. Finally, the tool is firmly fixed on the sonotrode after it is warmed to room temperature. Amongst these fixing methods, the first four are detachable fixing methods (Figure 2.9), and therefore allow for an easy exchange of the micro structure design to be fabricated.

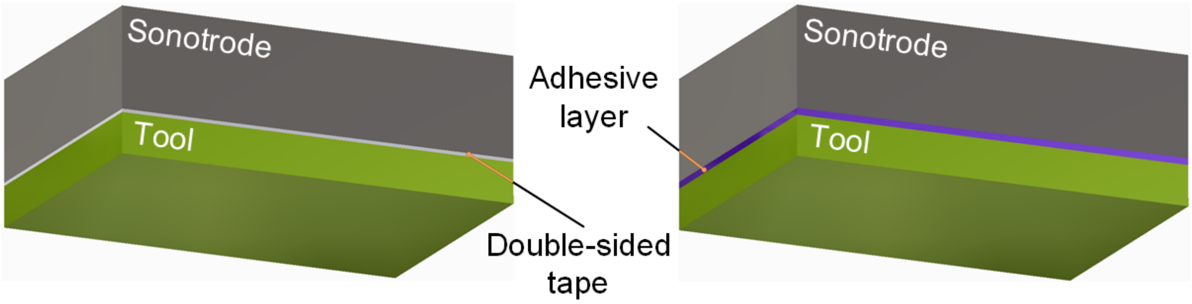

(a) Double-faced tape

(b) Adhesive agent

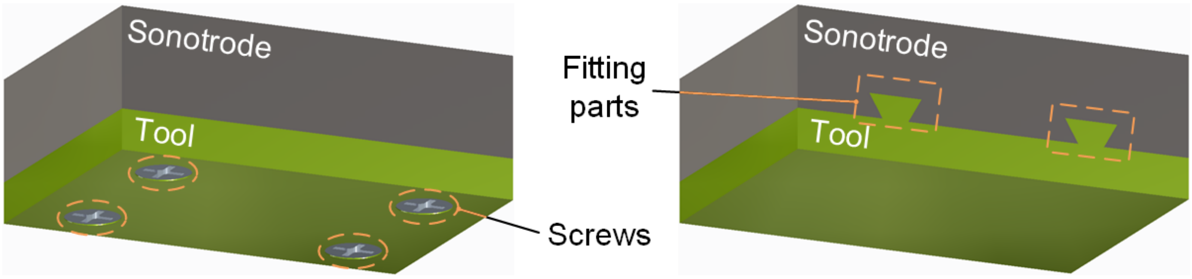

(c) Screw clamping

(d) Cooling fit

Figure 2.9: Schematic diagram of four detachable tool fixing methods.

The results of a comparative evaluation of detachable tool fixing methods [17] reveals the following conclusions. Much frictional heat was generated at the tape when fixing the tool with double-sided tape and cooling fit. On the contrary, tools fixed by an adhesive agent showed no temperature rises from heat generation when transferring ultrasonic vibration. The cycle time and amplitude of the ultrasonic vibrations were significantly altered from the ideal state when using screw clamping and cooling fit. Besides, the sinusoidal curve of ultrasonic vibrations was distorted when using screw clamping. This is because, except around the regions fixed by the screws, both edges of the tool and sonotrode are not constrained, so they can behave as free ends. Therefore, these free edges can deform and hit each other resulting in frictional heat in sonotrode and tool. The inhomogeneous amplification of the transferred ultrasonic vibrational energy over the entire area makes it harder to thermoform good samples.

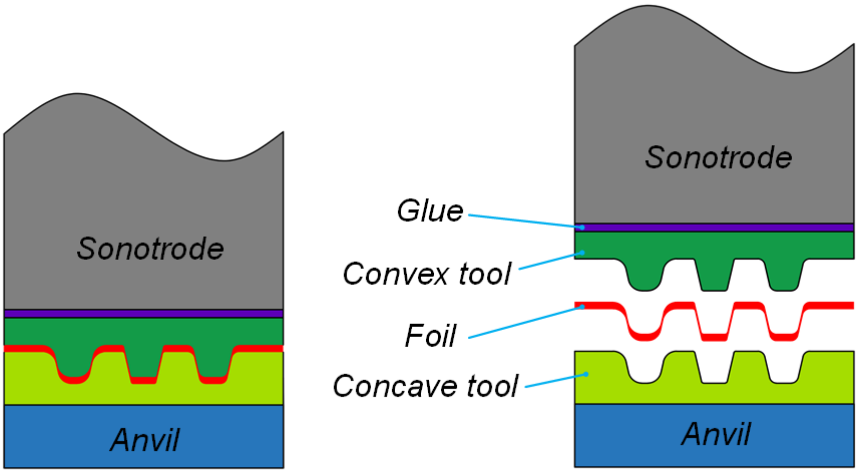

(a) Convex tool on the sonotrode, concave tool on the anvil

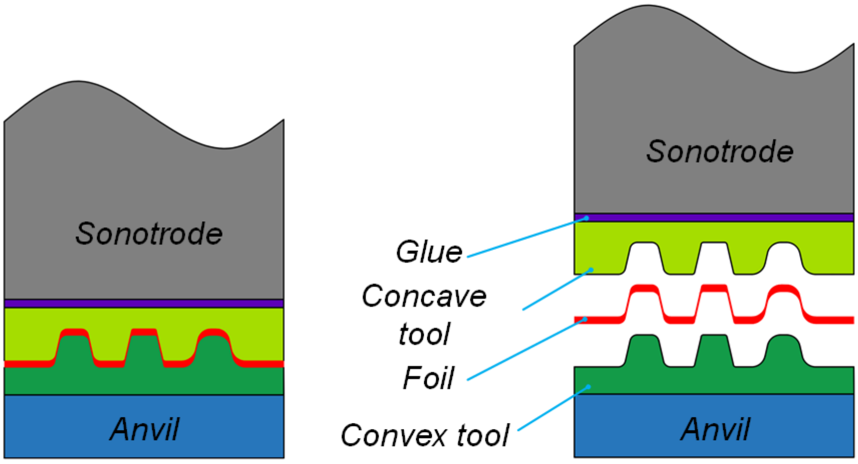

(b) Concave tool on the sonotrode, convex tool on the anvil

Figure 2.10: Configurations of tools in ultrasonic thermoforming [42].

A possible tools' configuration of a detachable tool fixing method is shown in Figure 2.10. As illustrated in Figure 2.10a, the first case is a convex tool pressed onto a foil supported by a concave tool. In the second case, a concave tool was attached to the tip of the flat sonotrode whereas the convex metal tool is fixed below the polymer foil, as shown in Figure 2.10b. The ultrasonic vibrations can be directly transferred from the sonotrode to the foil if direct milling micro structures on ultrasonic sonotrode.

2.5.3 Advantages and limits of ultrasonic thermoforming

Compared to traditional thermoforming, advantages of ultrasonic thermoforming are obvious: less thermal energy consumption, faster and lower cost. The ultrasonic thermoforming is a kind of contact heating but instead of heating the entire wrought material, the thermal energy is concentrated at protruding structures of the tool. It can be performed at room temperature with or without tool heating. By ultrasonic techniques, micro structures are formed and welded with cycle times as short as a few seconds. Besides, not much more than a commercially available ultrasonic welding machine and micro patterned tools are required for fabrication. What's more, the fast change to a new design is an important advantage of ultrasonic thermoforming of micro devices, especially when using detachable tools. New tools are milled from a metal plate within hours and newly designed micro devices can be fabricated within another hour. The ultrasonic thermoforming process can be performed in an open space so that it can be automated for mass production, unlike conventional thermoforming that must be performed in a closed chamber.

Ultrasonic vibrations not only generate heat, they also change the polymer melt viscosity. The viscosity of the polymer melt is significantly decreased by applying high frequency ultrasonic vibrations because they shear the polymer melt. This results in the disentanglement of molecular chains and reduction of their orientation and elastic deformation [43-45]. Aside from those physical effects, chemical effects, such as the molecular weight reduction and a narrowed molecular weight distribution, also contribute to the viscosity reduction of the polymer melt [46].

Experiments on ultrasonic hot embossing have shown that the vibration amplitude on the area of a large sonotrode is inhomogeneous resulting in inhomogeneous heating of the sample [18, 47]. Therefore it is expected also for ultrasonic thermoforming that the area of the sonotrode and thus also the sample is limited to achieve a homogeneous thermoforming.

Besides this, a larger sonotrode needs to be driven with more energy and the energy generated by an ultrasonic welding machine is limited because it is driven by a piezo stack excited to resonance vibrations. The larger this stack is, the more energy can be generated by it. On the other hand, a larger stack is also entailed with a lower resonance frequency. If the frequency is approaching the audible range at less than approximately 20 kHz, it is no longer possible to use such machines without further equipment protecting the people working with the machine and the advantage of low investment costs and easy use of the machine is lost.

2.6 Microsystems fabrication

Ultrasonic welding machines are used industrially primarily for welding, riveting, flanging, and cutting materials [9]. Virtually every thermoplastic polymer used for injection molding or hot embossing can also be processed by ultrasonic fabrication methods. Diverse microsystems have been fabricated by ultrasonic manufacturing, such as a microfluidic device for the observation of yeast cells [48], polymer chips for the detection of calcification [49], chemical analysis chips [11], and flow sensors [50]., a modular micro reactor system [7], polymer circuit boards[8], a micro mixer and micro pump [51], and interconnection devices [5].

In combination with the variety of processes (thermoforming, welding, hot embossing, punching, flanging), the ultrasonic manufacturing methods are well suited for micro-systems applications. A tool for ultrasonic thermoforming can perform various combinations of the process such as thermoforming, punching, and cutting. One or more operations can be performed simultaneously until a finished part is fabricated. Thus, using a tool facilitates the fabrication of semi-finished parts with different functional areas, especially for micro devices/systems.

3. Basic investigations of ultrasonic thermoforming

To investigate the ultrasonic thermoforming process, the basics must first be understood. This includes the experimental setup, process windows, and wall thickness distribution of ultrasonically thermoformed foils. Based on this, a guideline of tool designing, choice of tool type, and influence of tools' install locations are determined to accommodate different requirements for each specific application.

3.1 Experimental setup

The ultrasonic welding machine 2000IW+ from Branson Ultraschall, Dietzenbach, Germany, was used to thermoform samples. For the heating of the lower tool, a heating plate equipped with an electrical heater and a sensor inside was mounted onto the anvil of the machine. The target temperature was maintained by a temperature controller through feedback. This way, a stable temperature was achieved. The ultrasonic welding machine with a heating plate, lower tool, and polymer foil are shown in Figure 3.1.

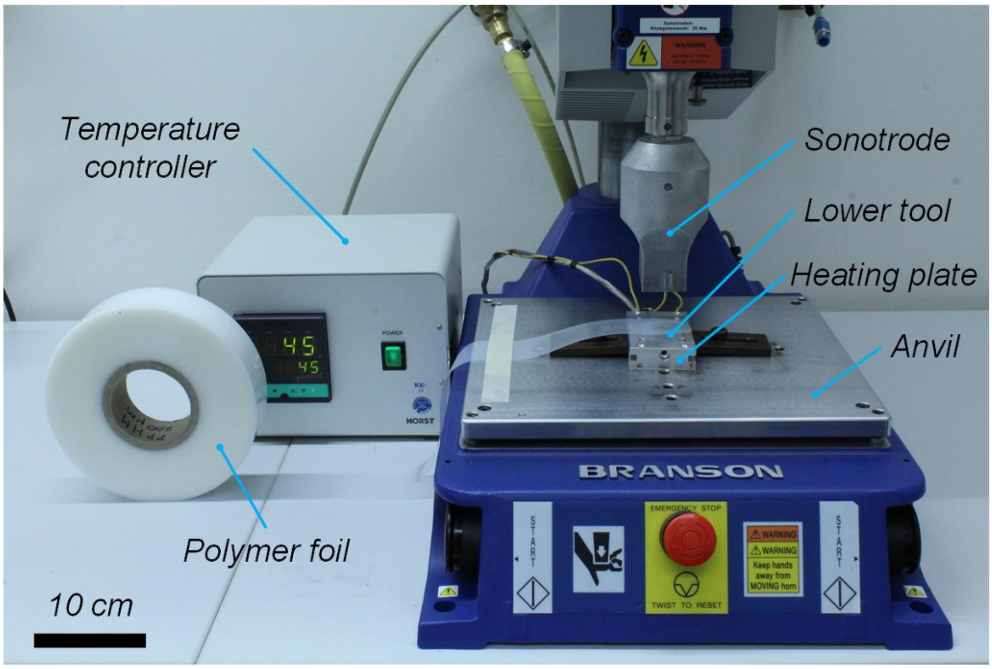

Figure 3.1: Experimental setup.

Detachable tools were used to shorten and simplify the manufacturing process. If micro structures would be milled directly into its surface, the ultrasonic sonotrode would need to be redesigned to ensure the desired vibration characteristics. Aluminum tools used in all experiments were milled by the high precision milling machine M7 HP from Datron AG, Germany employing milling tools from hard metal.

For ultrasonic thermoforming using detachable tools, fixing methods and their possible installation locations are described in chapter 2.5.2. When the upper tool is fixed on the sonotrode by glue, the installation procedures are as follows. The lower tool was first clamped onto the heater with the upper tool positioned on its top. This way, the lower and upper tool were well aligned to each other. Then, glue was applied onto the upper tool's surface facing the sonotrode and the sonotrode was slowly moved down and pressed onto the upper tool. Thus, the upper tool was glued well aligned onto the sonotrode. Finally, the screw on the anvil was adjusted to ensure that both aluminum tools were horizontally leveled.

3.2 Process windows of ultrasonic thermoforming

To investigate the limits of ultrasonic thermoforming, the process window was investigated employing polypropylene (PP) foils [12] as described below.

In this experiment, a pair of tools was used to thermoform the desired structures by ultrasonic thermoforming. Both tools were milled from aluminum plates, 2.5 mm in thickness. As shown in Figure 3.2, nine prism-shaped structures were evenly placed on a square with 20 mm edge length; the distance between each structure and its neighboring structures was 5 mm. These structures on the tool to be thermoformed had varied shapes.

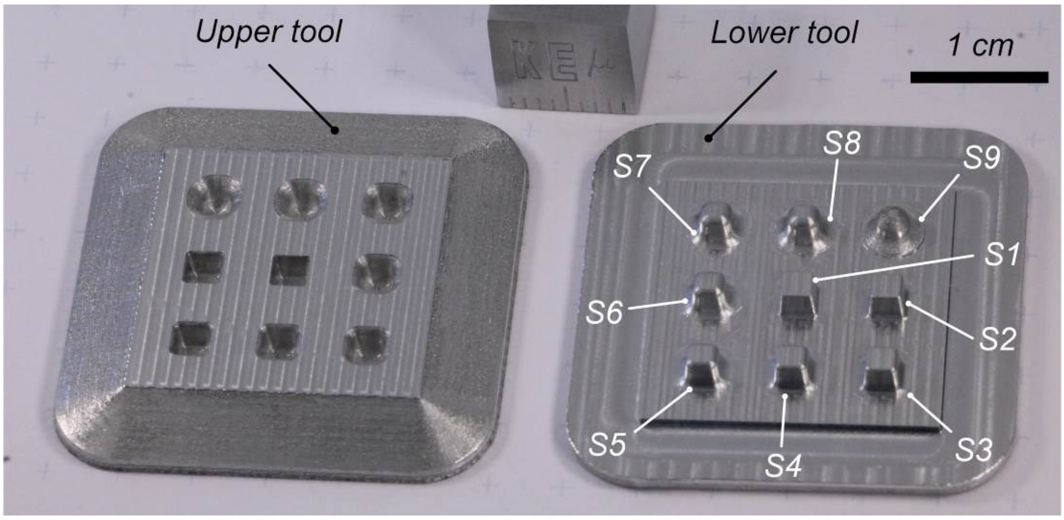

Figure 3.2: Photo of upper and lower tool.

All structures on the lower tool have a height of 2 mm, their lengths and widths are 2 mm at the top and 2.2 mm at the bottom. Walls of these structures have an inclination angle of 5.7° facilitating demolding thermoformed foils from tools. As shown in Figure 3.2, edges of the prism structures S1 through S9 were rounded with varying radii from 0.15 mm to 0.95 mm with increments of 0.1 mm.

Micro structures on the upper tool are the inverse of those on the lower tool. Hence, the gap between upper and lower tool is a function of the thickness d of the foil. As illustrated in Figure 3.3, the part of the foil that forms the sidewall is stretched from its initial length L_i to the length of the sidewall of the structure on the tool. Therefore, the average wall thickness d_a of the thermoformed foil is $d_a = d \sin(\alpha)$. With an inclination angle of $\alpha = 5.7°$ on upper and lower tool, the average wall thickness d_a is 10% of the initial foil thickness d. In addition, rounded edges of prism structures lead to an inhomogeneous stretch of the foil. This way, an inclination angle together with rounded edges of the micro structures results in an even thinner minimum wall thickness (cf. Figure 3.6a and Figure 3.8).

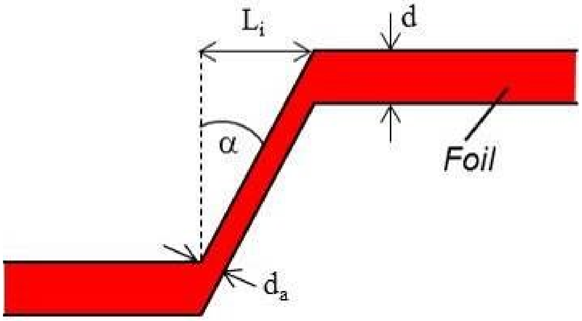

Figure 3.3: Cross-section of a foil after thermoforming.

Ultrasonic thermoforming was performed on the commercial ultrasonic welding machine (2000IW+, Branson Ultrasonics, USA) equipped with a sonotrode, 40 and 60 mm in width and length, respectively. A polypropylene (PP) foil with a thickness of 200 µm was used to thermoform micro structures. The objective of the experiment described here is to investigate the process window of ultrasonic thermoforming.

From the literature of ultrasonic welding and ultrasonic hot embossing, it is known that the most significant parameters for polymer melting by friction heat are pressing force, vibration amplitude, tool temperature, and vibration time. Vibration amplitude and vibration time both enhance the energy absorbed at the interface of polymer and tool and thus have a similar effect. Hence, the pressing force, duration of vibration, and lower tool temperature were varied. Process windows were determined with the pressing force increased from 460 N to 2760 N in increments of 230 N, the welding time was increased from 0.1 s to 6.0 s in increments of 0.1 s, and the lower tool temperature was increased from 25 °C to 65 °C in increments of 10 °C. Other parameters were remained constant, among which trigger force and peak-to-peak amplitude of vibration were 324 N and 16 µm, respectively. Besides, the cooling time was kept constant at 4 s for all experiments ensuring complete cooling and hardening of the polymer foil before demolding.

After each thermoforming, the temperature measured inside the lower tool was raised by about 10 °C due to the heat generated by ultrasonic vibrations. The thermoformed foil was demolded and then the next part of the foil was placed onto the lower tool. The following experiment started again when the tool was cooled down to the desired temperature. Thereby, the polymer foil was also heated up to the tool temperature before ultrasonic thermoforming started.

Samples were divided into four categories according to thermoformed structures on them. Good samples were those with no broken, opaque, or colored areas on all nine structures, as shown in Figure 3.4a. Incomplete samples were those incompletely thermoformed such that at least one of their structures had a total height of less than 2 mm (cf. Figure 3.4b). Damaged samples were those with opaque areas where the polymer was overheated and therefore decomposed (cf. Figure 3.4c). Broken samples were those with one or more holes or cracks on structures (cf. Figure 3.4d).

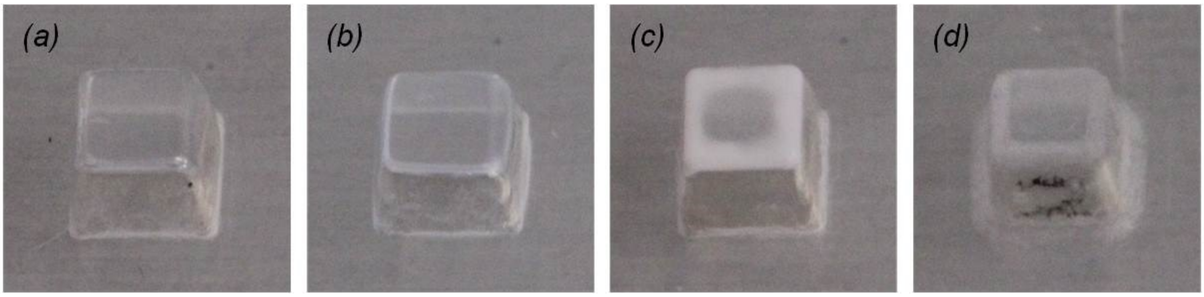

Figure 3.4: Thermoformed structures on samples rated good (a), incomplete (b), damaged (c), and broken (d).

The structure heights of tools and samples were measured with the optical microscope Eclipse LV 100 from Nikon, Japan. The lower and upper surface on structures were successively focused and their corresponding vertical position of the microscope stage were measured. The difference in these two vertical positions of the stage was noted as the height of the micro structure. The vertical position of the focus was determined with an accuracy of approximately 4 µm.

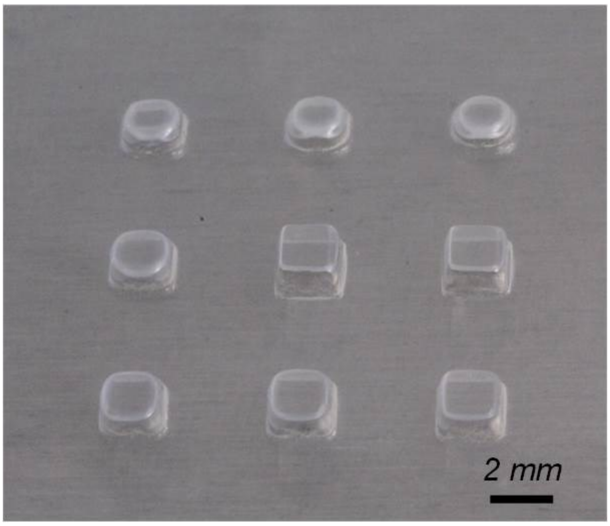

Figure 3.5: Micro structure generated by pressing the PP foil at room temperature without ultrasonic vibrations.

Simply pressing the PP foil between the tools without ultrasound also generated micro structures at room temperature, as shown in Figure 3.5. Pressing force and time were 1380 N and 2 s, respectively. During this process, the foil was completely stretched by tools, whereas these micro structures were incompletely formed due to the viscoelastic properties of PP. The foil tended to restore its shape after releasing the pressing force.

It is difficult to observe the cross-section of micro structures in thermoformed foils because they are too thin and flexible to cut across them without severe deformation. Hence, the edges of two separate foils were placed parallel over the center of the structure on the lower tool with a gap of about 0.5 mm as shown in Figure 3.6b before ultrasonic thermoforming. This way, the cross-section of structures on the thermoformed foil was observed with the confocal digital microscope VHX-500FE-M-E from Keyence, Japan. An example of a microscope photo of two layers of PP foils welded together during thermoforming is shown in Figure 3.6a.

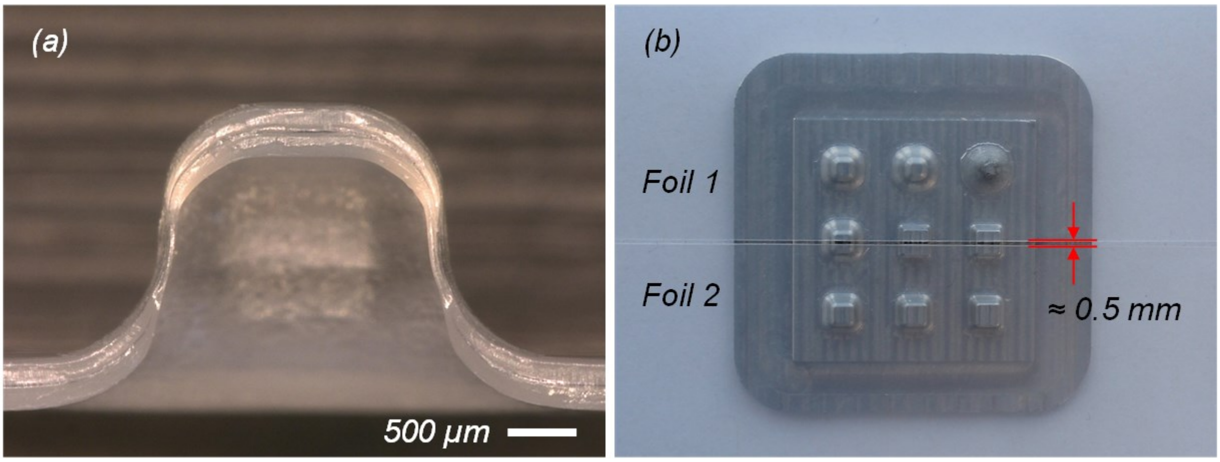

Figure 3.6: Photo of cross-section of two PP foils thermoformed together (a) by placing their edges over the center of structures on the lower tool (b).

The heights of nine structures on tools and on samples were measured and are shown in Figure 3.7. Structures on three samples were measured and their average heights were used. These samples were thermoformed with a pressing force, welding time, and lower tool temperature of 1380 N, 1.7 s, and 45 °C, respectively. Average heights of the nine structures on lower tool, upper tool, internal and external side of the samples are 2002 ± 3.4 µm, 2020 ± 3.0 µm, 1942 ± 12 µm and 1945 ± 23 µm, respectively. The differences between heights of nine structures on the tools are merely several micrometers and some ten micrometers on the samples. The average heights of the micro structures on the samples are approximately 96.5% of the heights on the tools indicating that there was shrinkage of a few percent.

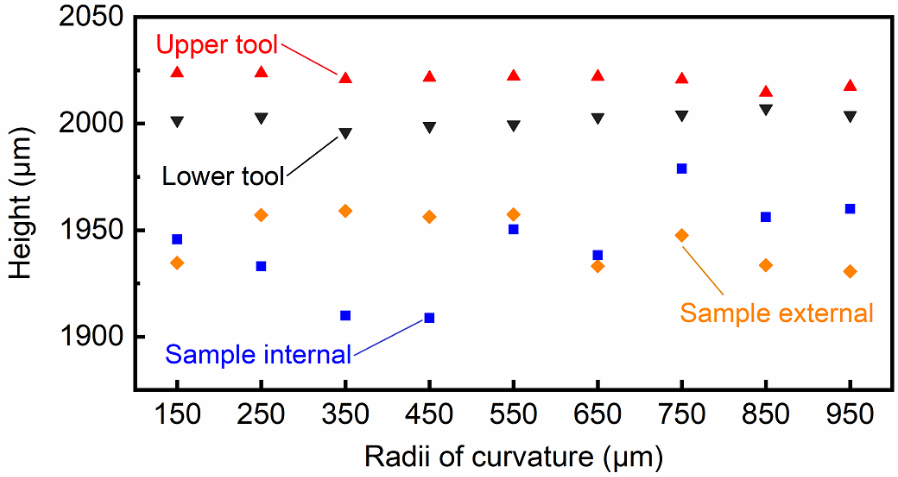

Figure 3.7: Structure heights on tools and samples.

The wall thickness of the nine structures on the samples is reducing where the tools showed a radius of curvature and got constant where the walls are not curved (cf. Figure 3.6a). Thicknesses were measured at these regions and they are shown in Figure 3.8. These samples were thermoformed by placing their edges over the center of the structures on the lower tool and thermoformed with a pressing force of 1380 N and a welding time of 1.7 s. Both sides of each structure were measured from five different samples. The overall average thickness of all measured structures is 16.5 µm, which is close to the aforementioned theoretical calculation (20 µm). The average wall thickness of the nine structures and their standard deviations increases with the radii of curvature in the range of 0.15 mm to 0.55 mm. All larger radii of curvature correspond to wall thicknesses of approximately 15 µm.

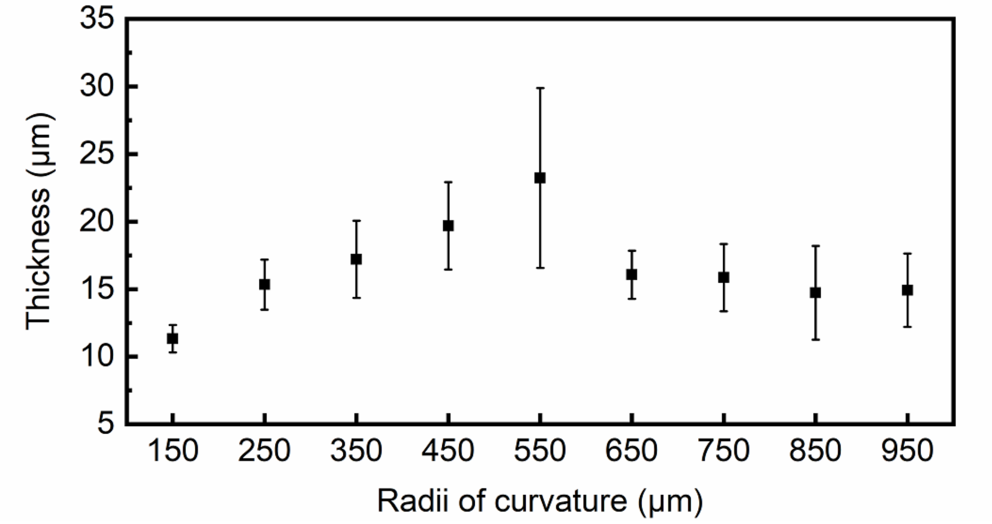

Figure 3.8: Wall thickness of structures on samples.

At different tool temperatures, the pressing force and duration of ultrasonic vibration were varied to find out limits between incomplete, good, damaged, and broken thermoforming as shown in Figure 3.9. The signs marking errors in figures indicate that these parameters caused an overload of the generator and consequently the ultrasonic welding machine reported an error.

The effects of varying the pressing force and the duration of ultrasonic vibrations were examined in terms of the resulting process windows. The thermoforming with a shorter duration of vibrations but the equal pressing force is a truncated version of the thermoforming for a longer duration of vibrations. As mentioned in chapter 2.1.1, the larger pressing force is, the higher the heating rate. That is why the minimum time required for a complete thermoforming is increasing when the pressing force is decreasing. This also explains why the duration of vibrations at which the sample is damaged or broken in general is longer when the pressing force is smaller. Therefore, with larger pressing force and longer duration of vibrations, more heat is generated in samples.

At elevated tool temperatures, the limit at which the foil is damaged or broken is reached at shorter times than at room temperature. Since the foil is already partly heated towards its softening temperature, less heat needs to be produced by ultrasonic vibrations. PP is stable up to a temperature of approximately 110 °C.

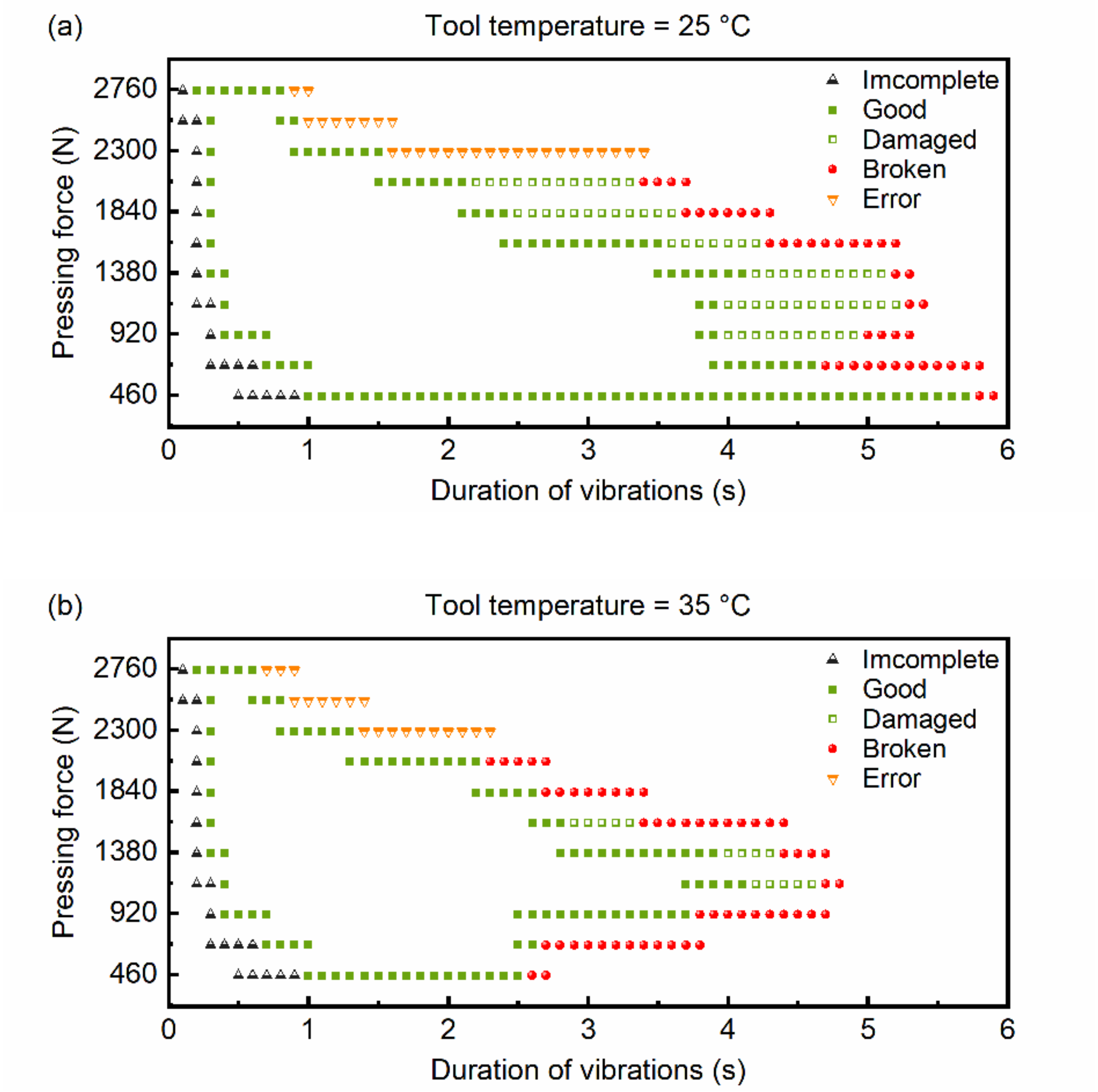

Figure 3.9a-b: Process window of ultrasonic thermoforming at different tool temperatures.

According to the process windows of 200 µm-thick PP foils, heating the tool is not necessary. However, since ultrasonic thermoforming is influenced by temperature, the process may become more independent of the room temperature if the tool temperature is kept constant, e.g., at 45 °C. To shorten the cycle time, the pressing force can be tuned to 1 kN and the duration of vibration to 0.3 s. So that enough heat is generated to heat the foil but the tool is not heated up too much. This way, the cooling time can also be reduced.

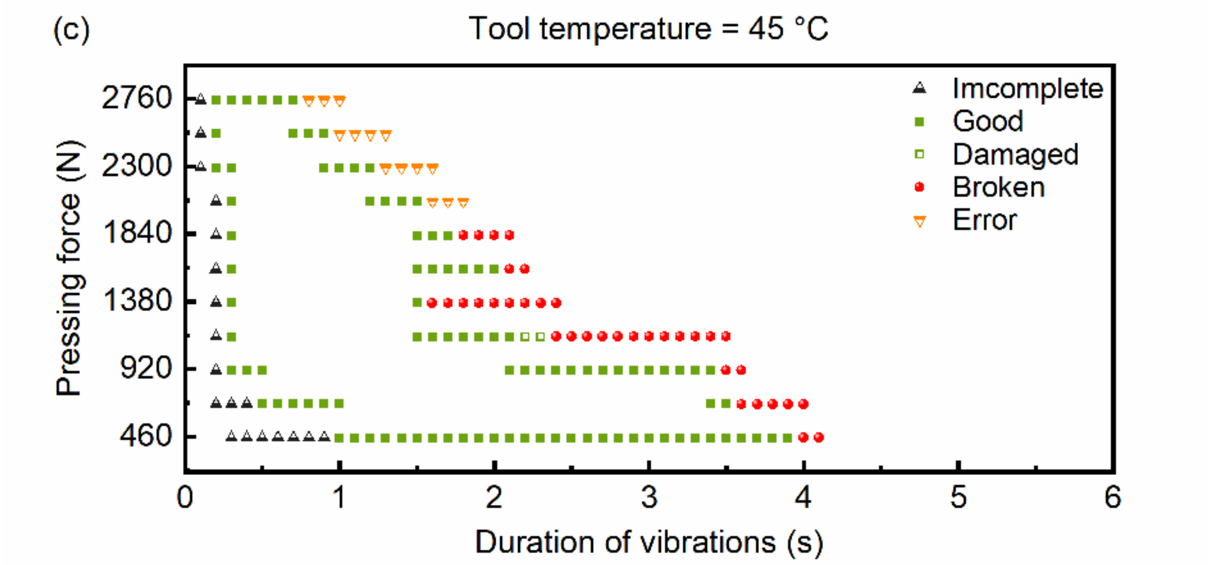

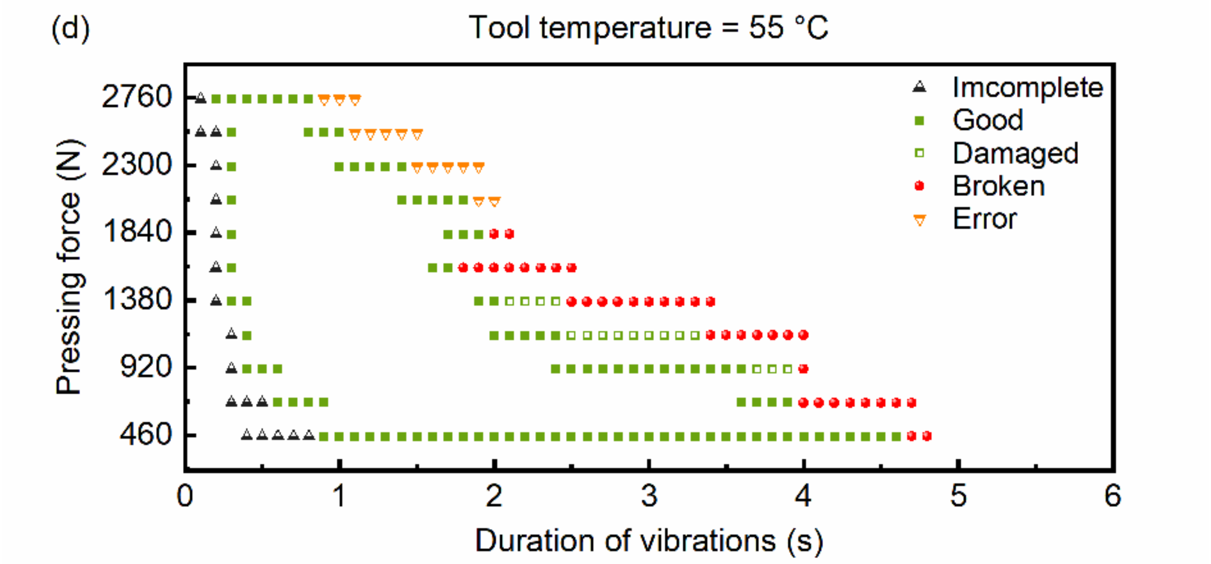

Figure 3.9c-d: Process window of ultrasonic thermoforming at different tool temperatures.

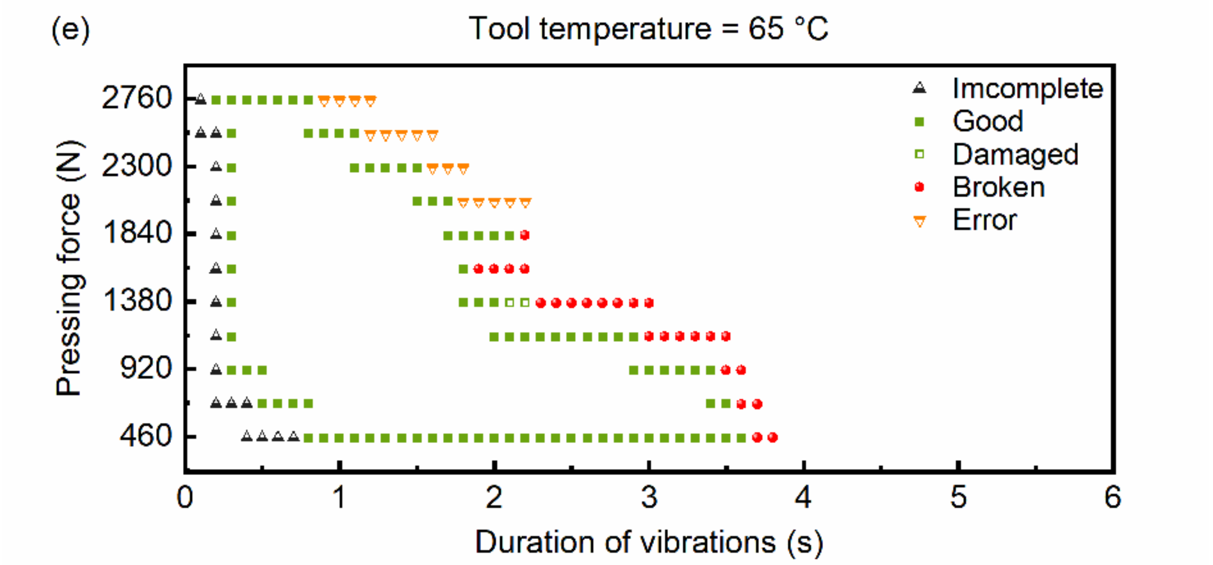

Figure 3.9e: Process window of ultrasonic thermoforming at different tool temperatures.

3.3 Wall thickness distribution in ultrasonic thermoforming

Wall thickness distribution is one of the factors which influence the stability of ultrasonically thermoformed parts [52]. It is also a determinant of the part's rigidity. Uniform wall thickness distribution is not possible in traditional thermoforming, but more uniform wall thickness distribution means rigid and stable structures [52]. Non-uniform wall thickness distribution is caused by differential stretching during thermoforming. Poor control of the material thickness distribution in the walls, the corners, and/or the bottom is a major drawback of traditional thermoforming [52, 53].

The relationship between mold design and the wall thickness distribution of the thermoformed part in ultrasonic thermoforming is still hard to predict. The objective of the experiment described here is to evaluate the wall thickness distribution of ultrasonically thermoformed parts using detachable rigid tools.

Three pairs of tools were designed with different semi-ellipse shaped cross-sections and they were employed to thermoform polymer foils. The profile of the tool is the determinant of the resulting cross-section of the thermoformed part. With different cross-sections of structures on tools, the thickness distribution of the thermoformed polymer differs. To investigate this difference, cross-sections of three pairs of tools were designed to be different, as illustrated in Figure 3.10. The dimension and aspect ratio of the micro structures on the tools are listed in Table 3.1.

Table 3.1 : Dimensions and aspect ratios of micro structures on tools.

Tool	**Height**	**Width**	**Aspect ratio**
A	1 mm	2 mm	0.5
B	1 mm	1 mm	1
C	1.5 mm	1 mm	1.5

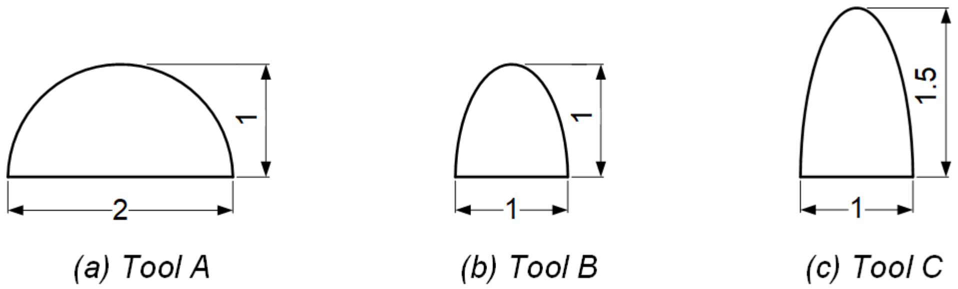

(a) Tool A (b) Tool B (c) Tool C

Figure 3.10: Cross-sections of micro structures on tools. All measures are in mm.

Tools were milled from aluminum plates with dimensions of 40 mm × 60 mm × 4 mm. A cruciform micro structure was placed on the center of each tool, and the length of its arm is 10 mm (cf. Figure 3.11). Cross-sections of the arms of each pair of tools are shown in Figure 3.10. The cross-section of micro structures to be thermoformed was varied on the tool.

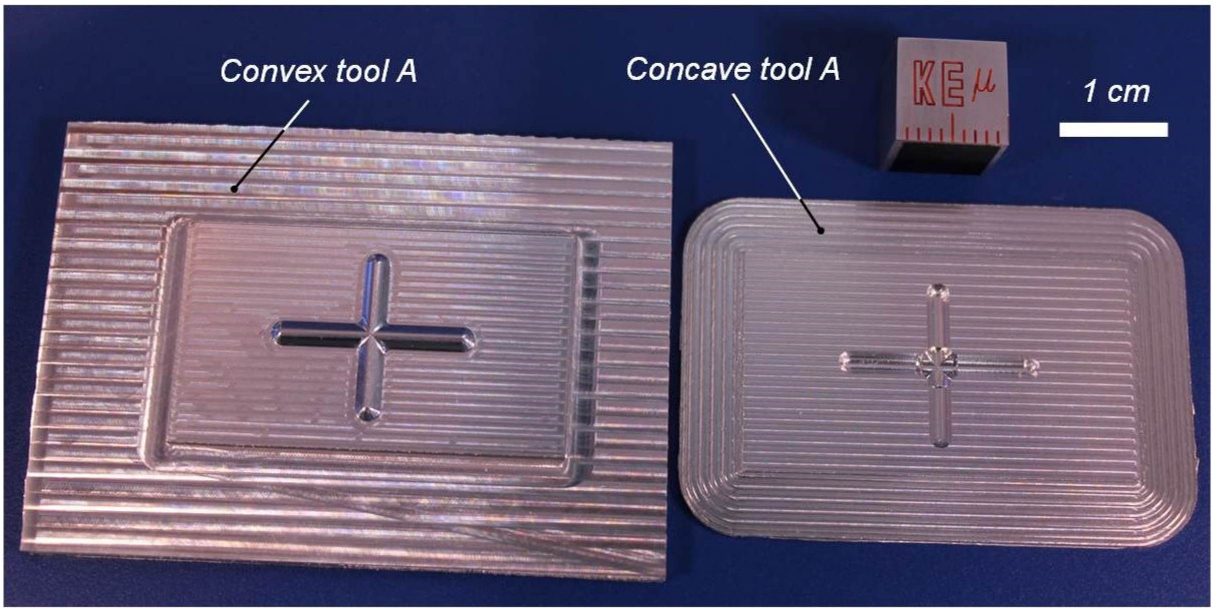

Figure 3.11: Milled tool pair A.

Ultrasonic thermoforming was performed on the ultrasonic welding machine HIQ Dialog 6200 from Herrmann Ultrasonics, Germany, equipped with a sonotrode, 80 and 120 mm in width and length, respectively. A foil from Poly (ethylene terephthalate glycol) (PET-G), 500 µm in thickness, was used in the experiments. The actual thickness of the PET-G foil measured with a micrometer screw gauge is 580 µm. Due to different cross-sections of each pair of tools with different aspect ratios, different parameters were used in experiments to get a good result. Welding time, pressing force, amplitude, trigger force, holding force, and cooling time for thermoforming three samples were 0.8 s, 600 N, 20 µm, 300 N, 800 N, and 3 s respectively. Ultrasonically thermoformed polymer foils of three pairs of tools are shown in Figure 3.12. Sample A, B, and C were thermoformed at room temperature (20 °C). There was no tool pre-heating.

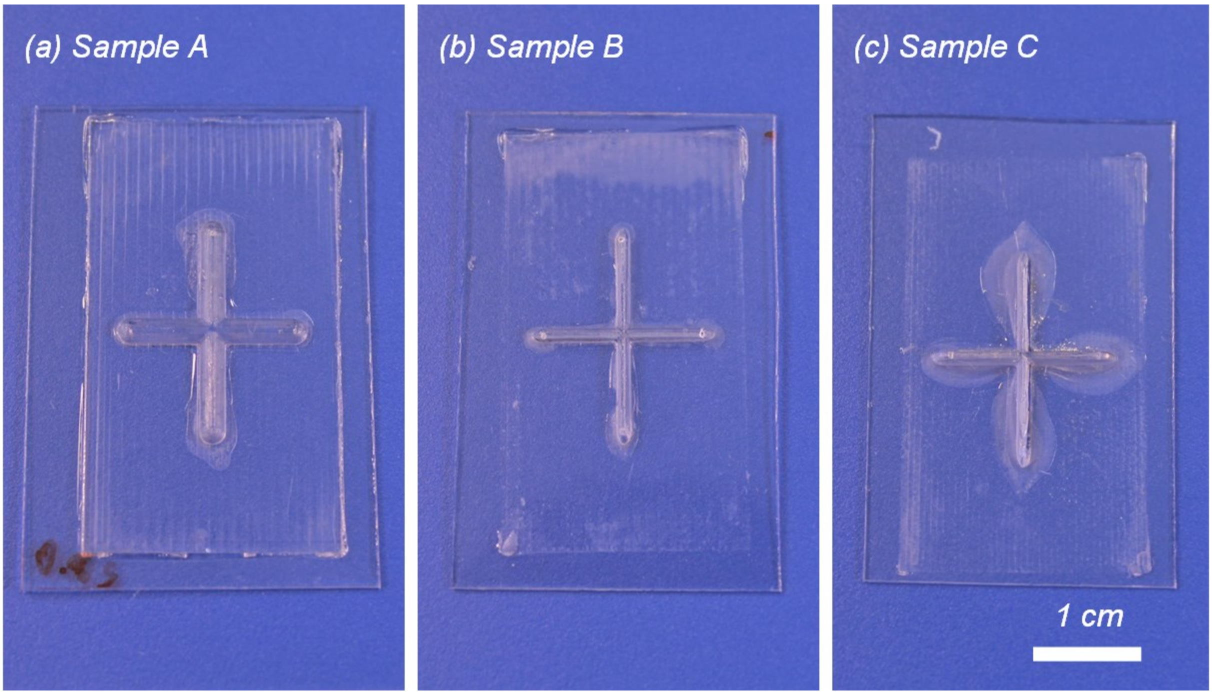

Figure 3.12: Polymer foils of sample A (a), sample B (b), and sample C (c).

The cross-sections of the thermoformed foils were observed by cutting through the middle of one arm of the cruciform structure using a knife. This way, the thickness of the generated structures was observed with the confocal digital microscope VHX-500FE-M-E from Keyence, Japan. The observed microscope photos of cross-sections of each sample are shown in Figure 3.13

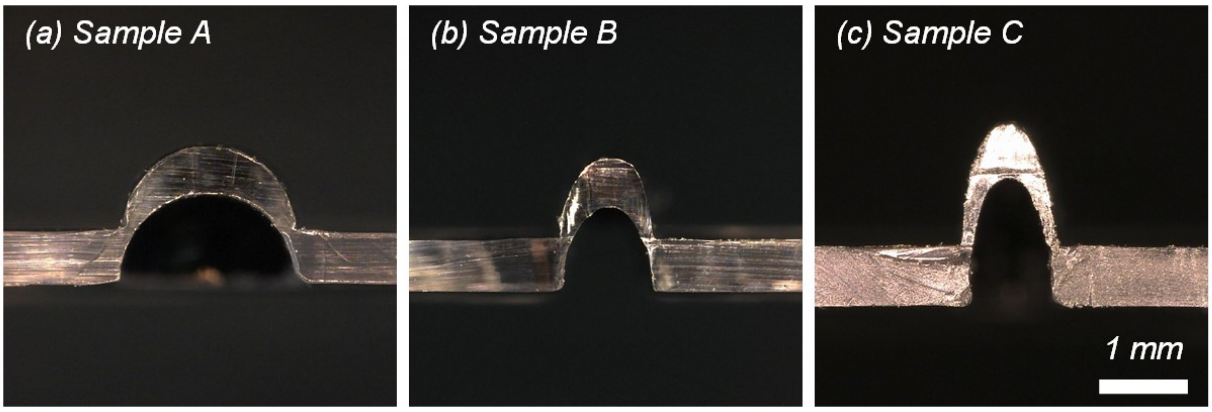

Figure 3.13: Cuts through sample A (a), sample B (b) and sample C (c).

A feasible way to obtain the thickness distribution is image processing. Thus, a self-developed program was used to automatically detect the contours of photos in Figure 3.13 and then calculate the wall thickness point by point. This program utilizes OpenCV on python to process microscope photos. These photos were first turned into grayscale and their edges were detected by the Canny edge detector [54]. After morphology operations and filtering out undesired contours, the main contours were obtained and finally separated into upper and lower contour, as shown in Figure 3.14.

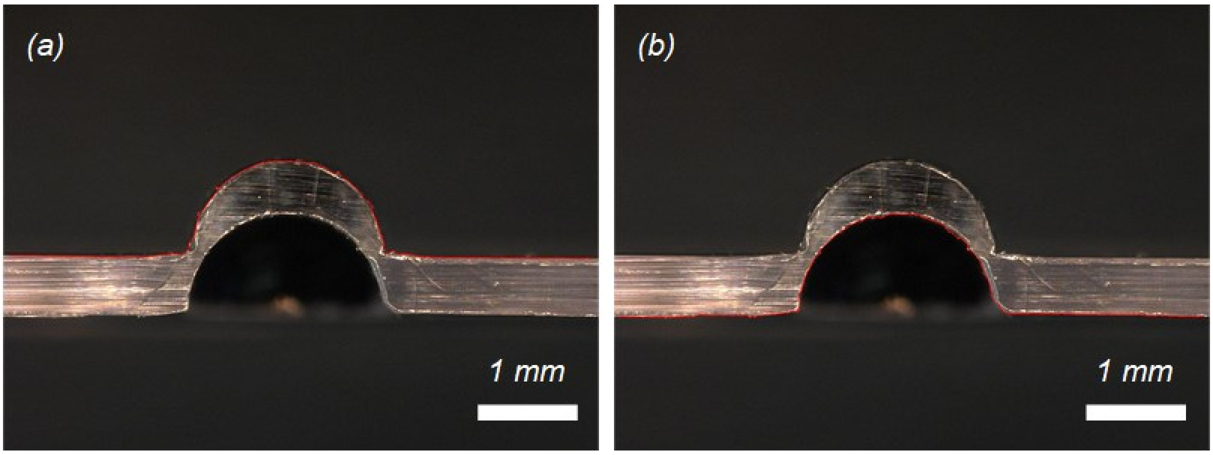

Figure 3.14: Detected upper (a) and lower (b) contour of sample A.

The tangent line of a point on the lower contour was obtained by linear fitting tens of points on both sides. It is already known that the product of tangent slope and vertical slope is -1 if both slopes exist, we can easily know the slope of perpendicular line on this point. Therefore, a perpendicular line is drawn from a point on the lower contour and then find its intersection point on the upper contour, as shown in Figure 3.15. By calculating distance between each point on the lower contour and its intersection point on the upper contour, the actual wall thickness distribution was obtained.

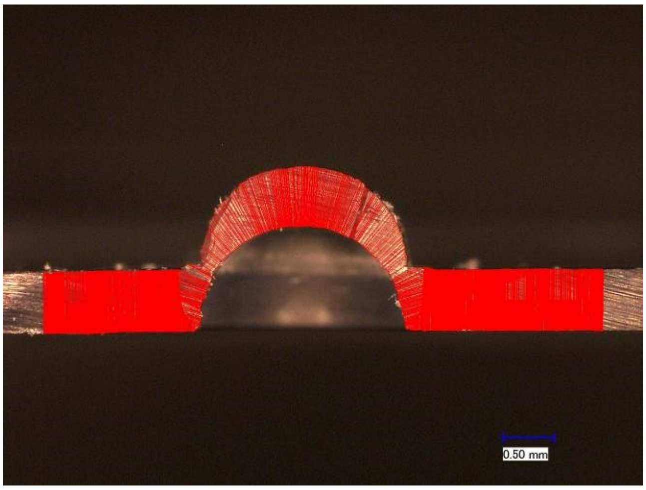

Figure 3.15: Points on the lower contour and their corresponding intersection points.

For each sample thickness, values were also obtained by calculating the gap between the tools and denominated as theoretical value. In order to know the theoretical thickness distribution of samples, cross-sections of the cruciform structure on the three pairs of tools were obtained from their 3D models. In these models, upper tool and lower tool were placed parallel to each other with an interval equal to the thickness d of the polymer foil to be thermoformed, as shown in Figure 3.16.

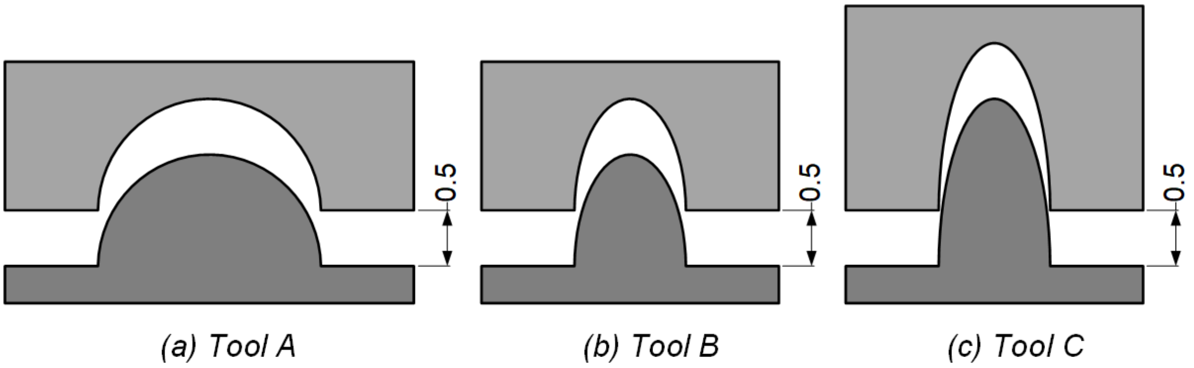

(a) Tool A (b) Tool B (c) Tool C

Figure 3.16: Assembly models of tool A (a), tool B (b), and tool C (c).

To give a better insight into the wall thickness of thermoformed samples, actual and theoretical wall thickness distributions for three thermoformed samples' are shown in Figure 3.17. The distribution is made up of two distinct regions: micro structure and unshaped area on both sides. Across these, there are large variations in the thickness of the micro structure, whereas the thickness of the unshaped area was essentially unchanged compared to the initial thickness of the foil.

As understood from Figure 3.17a, actual wall thickness distribution on sample A showed a decreasing trend from the center of the semicircular structure to both sides. Calculated theoretical thickness in the middle of the semicircular structure is slightly smaller than the initial foil thickness (about 580 µm), while the minimum thickness was calculated to about 200 µm at the corner of both sides. Actual and theoretical wall thickness share the same trend and are nearly the same. The same phenomenon can be observed in Figure 3.17b, c for the semi-oval structure on sample B and C. As for sample B, its actual maximum and minimum wall thickness are about 580 µm and 140 µm, respectively, only the actual minimum wall thickness is slightly larger than the theoretical value, which is 120 µm. The actual wall thickness on sample C is larger than the theoretical value, as shown in Figure 3.17c. This unshaped region on sample C is about 700 µm, 120 µm more than the initial thickness of the foil. This is probably caused by the flow of excessive polymer melt from the micro structure to the unshaped region increasing the gap between the tools. The influenced area surrounding the cruciform micro structure on sample C can be observed in Figure 3.12c. Other samples, such as sample A and B, were also influenced by the flow of excessive polymer melt, but only limited to the adjacent area, as shown in Figure 3.12 a, b and their corresponding wall thickness distribution in Figure 3.17 a, b.

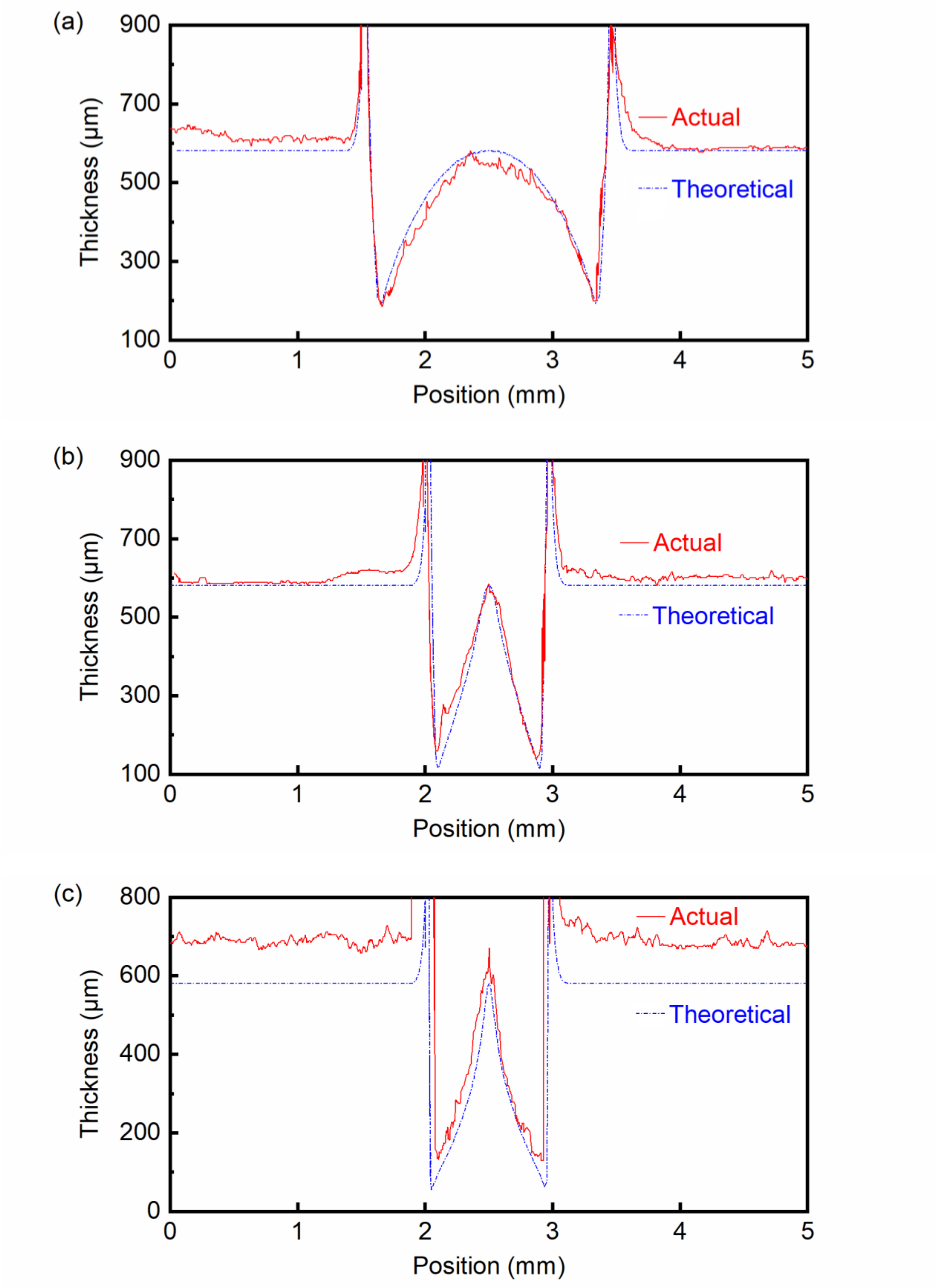

Figure 3.17: Actual and theoretical wall thickness distributions of sample A (a), B (b), and C (c).

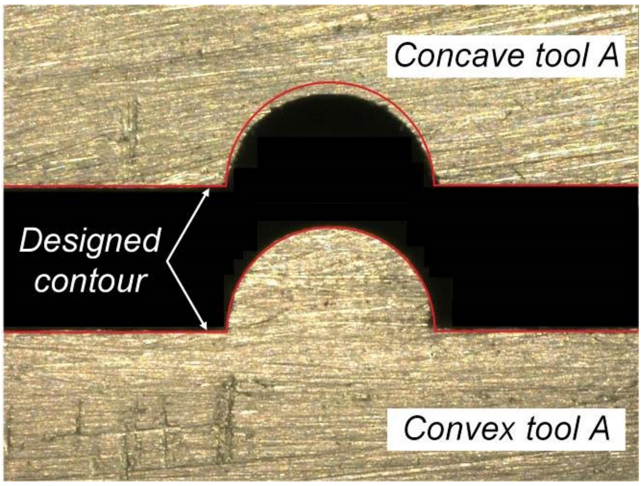

Figure 3.18: Cross-section of milled concave tool A and convex tool A, the red lines are their contour in the original design.

Excessive polymer melt from the micro structure increases the gap between the tools and therefore causes a larger wall thickness of surrounding areas of the micro structure on samples. The main reason for this is that the cross-sections of milled tools are not exactly the same as their original design. As shown in Figure 3.18, the shape precision of the cross-section on the milled convex tool is quite high, but not on the milled concave tool. Compared to the original design, convex structures tend to have larger cross-sections but concave structures tend to have smaller cross-sections on actual milled tools. Hence, the gap between milled tools is narrower than expected and that is why excessive polymer melt flows from micro structures to unshaped regions during ultrasonic thermoforming. This deviation of milled tools from their original design can be ascribed to a machining error during milling. The problems caused by excessive polymer melt possibly can be partly solved by decreasing the deviation of milled tools from their original design, or by locally increasing the gap between tools to prevent excessive polymer melt flowing into an unshaped region.

Only one side of the traditionally thermoformed part is a perfect replica of the tool’s geometry. By comparison, both sides of the ultrasonically thermoformed part have replicated the exact geometry of the tools. Parameters in ultrasonic thermoforming have less influence on wall thickness distribution compared to the tools.

3.4 Guidelines of tool design

Thermoformed parts have non-uniform thickness distributions due to strain localization during the thermoforming process [55], which leads to defects such as excessive local thinning or even fracture. As the aspect ratio of structures on thermoformed foils increases, it becomes difficult to successfully thermoform foils without cracks and the needs arise for tools to shape the foil in order to create a more even and more controlled wall thickness distribution. Since for ultrasonic thermoforming rigid tools can be used, the geometry of the tool plays a more important role. Typically, mechanical performance of a thermoformed foil would be dictated by these thinnest regions at corners, and therefore it is desirable to locally increase thicknesses of these regions by redistributing material from a relatively thick region or from excessive polymer melt during thermoforming. Changing the geometry of the tool is one option to achieve this. The overall objective of this chapter is to investigate the tool geometry that may be adjusted to control the wall thickness distribution of ultrasonically thermoformed foils, and provide guidelines for tool design.

Since the thermal energy is concentrated on protruding structures on tools during ultrasonic thermoforming, the foil is heated at such structures and adapts to the shape of the tools. At the same time, polymer melt is also generated in surrounding areas and flows into the cavity between concave and convex tool. Ideally, perfectly matched convex and concave tools are desired, and once achieved, the melted polymer fills the cavity between the tools and micro structures from polymer foil with a desired thickness are thermoformed.

Besides this, compared to the perfectly matched convex and concave tool, the gap between tools should be neither too narrow nor too wide. If the gap is too narrow, the concentration of thermal energy on a certain spot would lead to overheat, or even decomposition of the polymer material. In addition to this, excessive polymer melt could increase the gap between tools; hence the overall wall thickness of the influenced area on the thermoformed foil is increased as mentioned in chapter 3.3. On the other hand, when the gap is too wide, the cross-section of the thermoformed micro structure is hard to control, and chances are high that the foil is incompletely thermoformed.

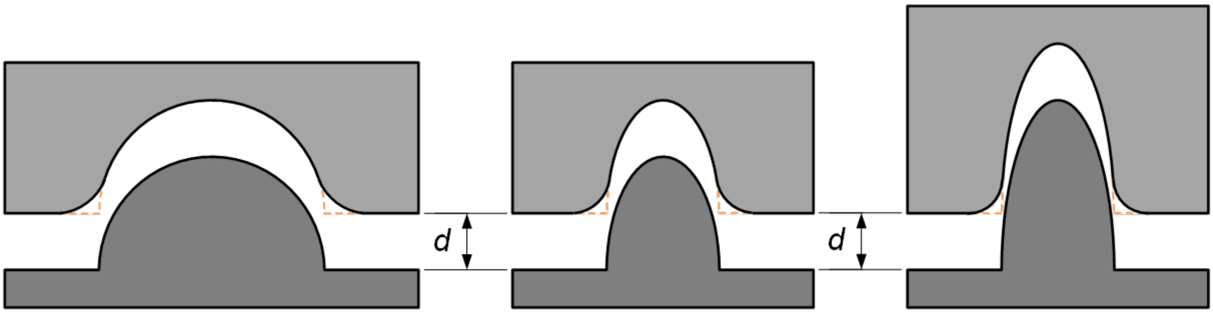

(a) Tool A (b) Tool B (c) Tool C

Figure 3.19: Assembly models of tool A (a), tool B (b), and tool C (c) with rounded concave tool.

A feasible strategy of optimizing the design of tools is to round edges at corners on the concave tool as shown in Figure 3.19. The dotted line marks the unrounded corners on the concave tool. Hereinafter, the concave tool with or without rounded corners is referred to as rounded concave tool and unrounded concave tool, respectively. With rounded corners, the gap between tools at corners is increased. This way, extra space is available at corners for excess polymer melt. The wall thickness distributions described in chapter 3.3 show that the minimum gap between tools and the minimum wall thickness on thermoformed samples are located at the corners of thermoformed micro structures. Rounding corners of a concave tool on the one hand increases the minimum gap between tools, and on the other hand, prevents potential fracture caused by sharp edges at corners.

Tool A was further used to investigate the influence of rounded edges at corners on thermoformed foils. The unrounded concave tool A and its rounded version with rounding radii of 0.5 mm were used. Both rounded and unrounded concave tools were milled from aluminum plates with the dimensions 46 mm × 31 mm × 2 mm.

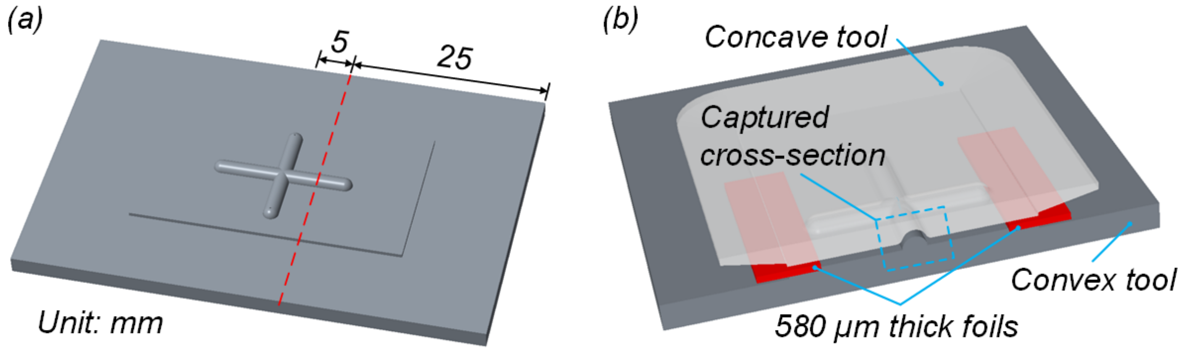

Figure 3.20: Tools were cut along the red dash line (a) and 580 µm thick foils were sandwiched between cut concave tool and convex tool to observe the cross-sections of tool pairs (b).

Convex tool, rounded concave tool and unrounded concave tool were cut through the middle of one arm of the cruciform structure by milling as shown in Figure 3.20a. 580 µm thick foils were sandwiched between cut concave tool and convex tool (cf. Figure 3.20b), and tools were clamped by a fixture allowing for the observation of the cross-section of the gap between the tools. The cross-section of the tool pair with a rounded concave tool and with an unrounded concave tool are shown in Figure 3.21. The vertical distance between concave tool and convex tool is 580 µm, equal to the thickness of used PET-G foil. It is clear that the gap at corners between the tools is wider when the concave tool is rounded.

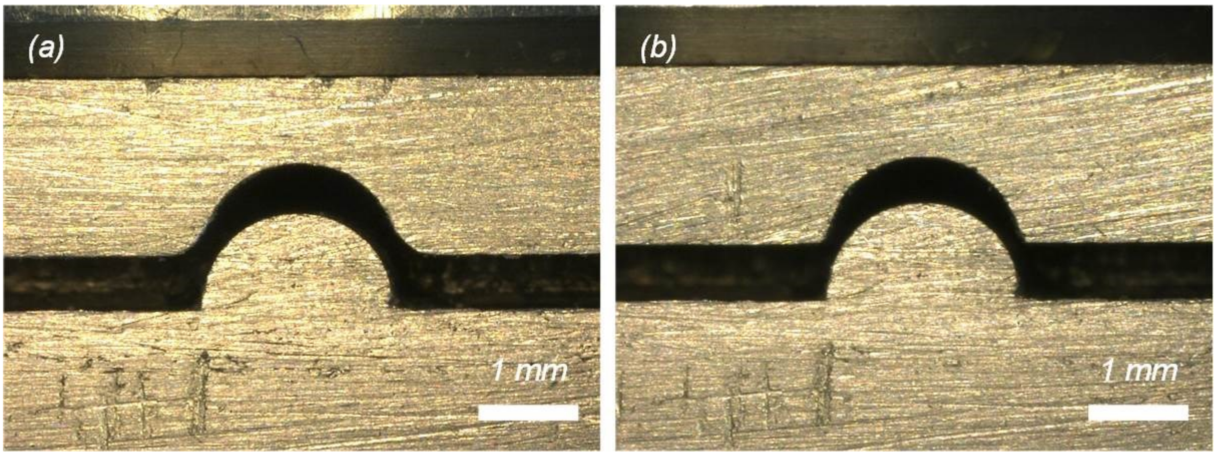

Figure 3.21: Cross-section of tool pair with rounded concave tool (a) and with unrounded concave tool (b).

Two samples were ultrasonically thermoformed from a PET-G foil with an actual thickness of 580 µm using rounded and unrounded concave tools as shown in Figure 3.22, and they are referred to as rounded sample (cf. Figure 3.22a) and unrounded sample (cf. Figure 3.22b) in this chapter. Both samples described here were thermoformed using the convex tool A (cf. Figure 3.11) as another part of the tool pair with identical parameters. The welding time, pressing force, amplitude, trigger force, holding force and cooling time are 0.8 s, 600 N, 20 µm, 300 N, 800 N, and 3 s, respectively. There was no tool preheating in both thermoformings.

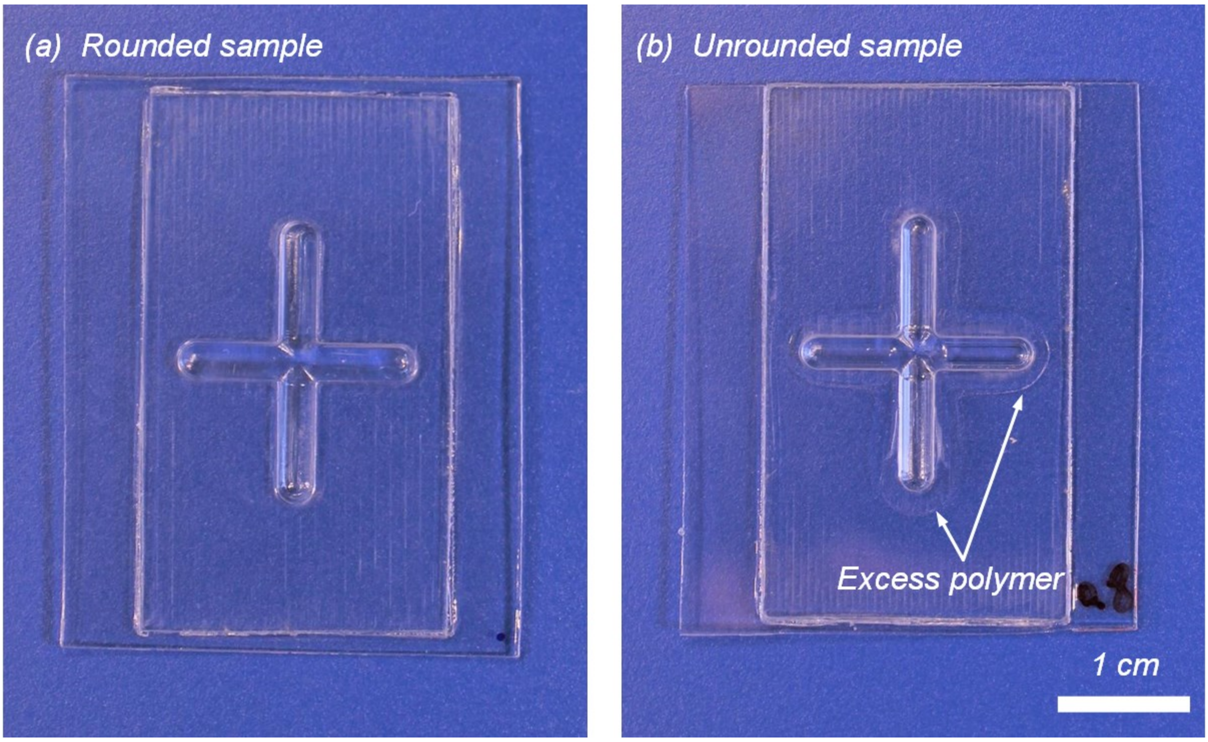

Figure 3.22: Photos of rounded sample (a) and unrounded sample (b)

As seen in Figure 3.22b, there is a mark with a width of about 2 mm surrounding the cruciform micro structure on the unrounded sample, this area was influenced by excessive polymer melt during thermoforming. Due to the difference between original design and milled tool, convex tool and concave tool do not perfectly match. The gap between the two tools was smaller than designed and therefore excessive polymer melt flowed into the surrounding area of thermoformed structures during ultrasonic thermoforming.

It is expected that the wall thickness of micro structures on thermoformed foils slightly decreases with increased process parameters, such as pressing force, welding time, amplitude, and tool temperature, which facilitate the temperature rise of the foil. With elevated foil temperature, more polymer could be melted and squeezed into a larger unshaped area, especially with higher pressing force. Pressing force is the driving mechanism of this laminar viscous squeeze flow. Nevertheless, there is no visible mark surrounding the cruciform micro structure on the rounded sample (cf. Figure

3.22a), which means no polymer melt flowed from the micro structure to unshaped regions.

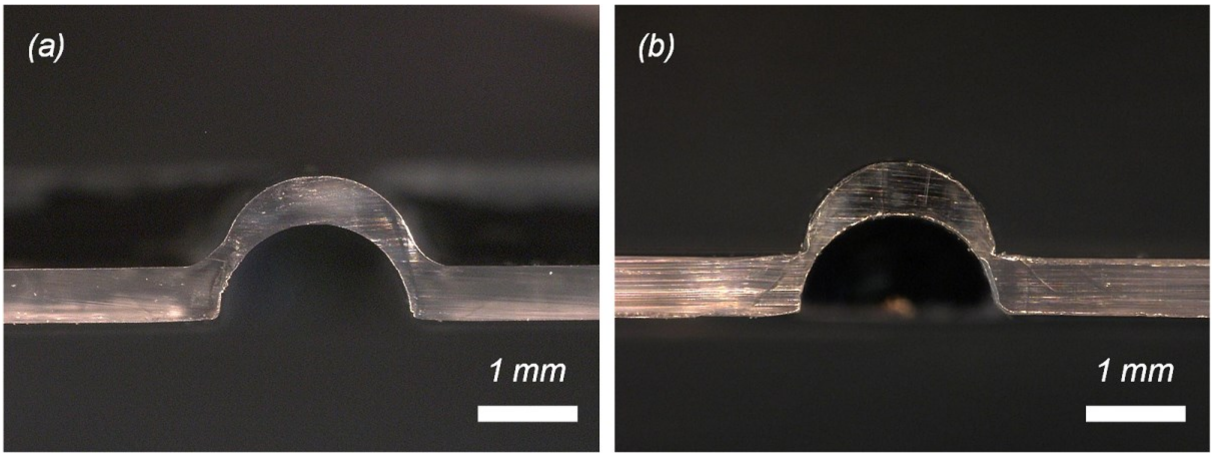

Figure 3.23: Cross-section of rounded sample (a) and unrounded sample (b).

Two samples were cut through the middle of one arm of the cruciform structure on them using a knife to observe their cross-sections. Microscope photos of the cross-sections of rounded and unrounded samples are shown in Figure 3.23. The thinnest area on the rounded sample (cf. Figure 3.23a) is still located near the corners, but it is much thicker than the one of the unrounded sample (cf. Figure 3.23b). Both rounded and unrounded sample were completely thermoformed and their cross-sections are identical to the gap between the tools shown in Figure 3.21. Both sides of the rounded samples have replicated the shape of the gap between the tools.

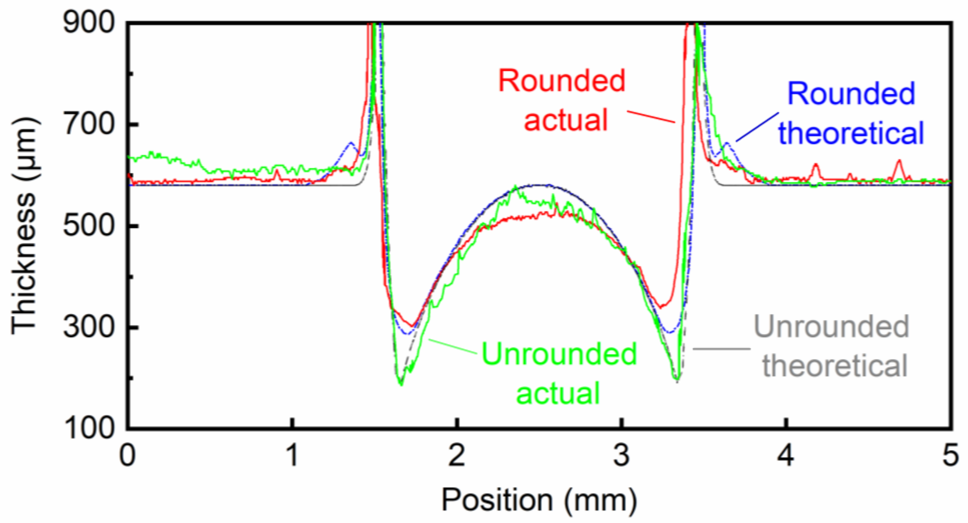

Figure 3.24: Actual and theoretical thickness distribution of rounded and unrounded sample.

As illustrated in Figure 3.24, the thickness distribution of rounded and unrounded sample share the same trend, but the minimum value of the rounded sample is

300 µm which is much larger than the one of the unrounded sample. Clearly, there is a slight reduction of the thickness in the middle of the semicircular structure, but the largest change is at the corners where the minimum thickness increased from 200 µm to 300 µm. These changes are largely consistent with the geometry of concave tool, as the gap at the corner between convex and rounded concave tool is wider than that between convex and unrounded concave tool. For this reason, the excessive polymer melt during thermoforming and part of material in the middle of the micro structure filled the gap between tools. This is presented in Figure 3.19a showing the gaps between convex tool and rounded/ unrounded concave tool.

3.5 Comparison of rigid tool and flexible tool

In ultrasonic thermoforming, there are two types of controlling parameters: process and material. Process parameters include pressing force, welding time, amplitude, tool temperature, trigger force, cooling time, and holding force. Unlike material parameters, these can be adjusted during thermoforming and used to fine tune the outcome of the final thermoformed foil so as to avoid defects. Material parameters refer to the properties of foil and tool. Material selection determines the corresponding thermal and frictional properties of contacting surfaces. If one of the tools is from a soft material such as silicone, it can adapt to the shape of the rigid counter tool, intermolecular friction in the tool can provide additional heating, and the friction between sample and soft tool is different from the one obtained with a rigid tool. Together with this, the design of tools has been found to have the greatest influence on wall thickness distribution and geometry of thermoformed foils.

To simplify this study, the influences of parameters such as the pressing force, amplitude, trigger force, holding force, cooling time, and tool temperature were eliminated from the experiment by selecting a fixed combination of these process parameters for ultrasonic thermoforming. The parameter investigated in this experiment were limited to tool type of concave tool, material of the foil and its initial thickness, and duration of thermoforming.

3.5.1 Fabrication of flexible tools

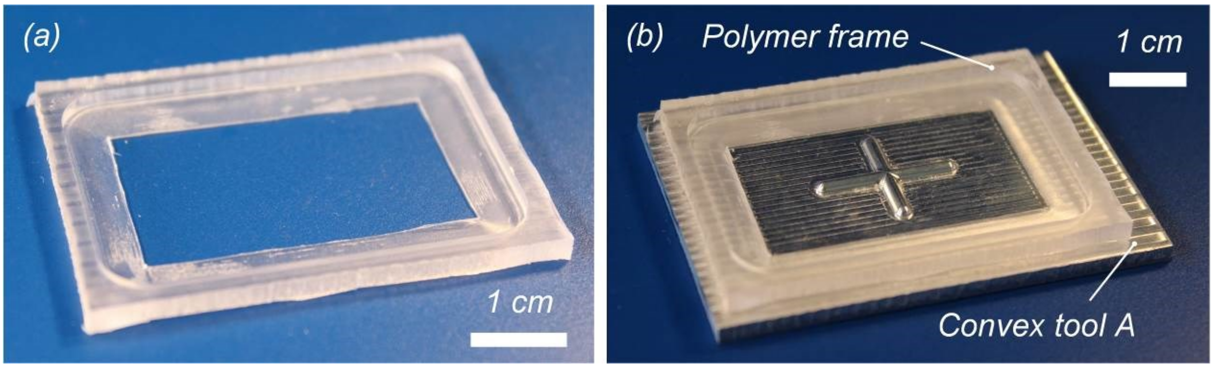

Figure 3.25: Photos of polymer frame (a) and its placement when fabricating flexible tools (b).

Tool pair A was used to compare the effect of the tool type on the formability of micro structures. Besides the rigid concave tool A (cf. Figure 3.11), a flexible concave tool (cf. Figure 3.26a) and a flexible flat tool (cf. Figure 3.26b) were also used. Both flexible tools were fabricated using Dow Corning® 184 silicone elastomer, among which the flexible concave tool has the exact inverse structure of the convex tool A (cf. Figure 3.11). A frame (cf. Figure 3.25a) milled from polymer was placed on the top of the convex tool A with the cruciform structure locating in the center of the frame as shown in Figure 3.25b. The polydimethylsiloxane (PDMS, Sylgard 184, Dow Corning, Midland, MI, USA) with mixing ratio of 10 (silicone resin): 1 (silicone elastomer) was poured into the center of the frame, and then a flat plate was placed on the top of the frame. After curing at 70 °C for 20 min, the flexible tool with inverse cruciform structure was obtained (cf. Figure 3.26a). By replacing the convex tool A with a flat plate, the flexible flat tool (Figure 3.26b) was obtained by the same procedure.

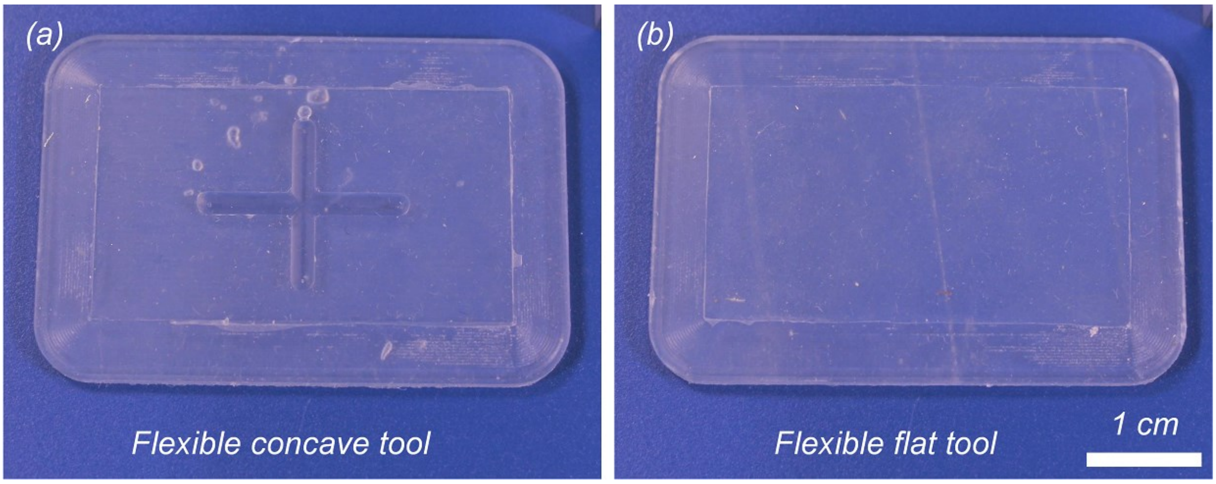

Figure 3.26: Photos of flexible concave tool (a) and flexible flat tool (b).

3.5.2 Ultrasonic thermoforming of amorphous PET-G foils

The convex tool A (cf. Figure 3.11) was used as another part of the tool pair to thermoform polymer foils in this chapter. The pressing force, amplitude, trigger force, holding force, cooling time, and lower tool temperature were kept constant at 600 N, 20 µm, 300 N, 800 N , 3 s, and 22 °C, respectively, because a wide process window has been found in Fig. 3.9 at these parameters. Both amorphous and semi-crystalline thermoplastics were thermoformed using aforementioned tools.

As a clear amorphous thermoplastic, PET-G foil (500 µm in thickness) was thermoformed by rigid concave tool, flexible concave tool and flexible flat tool in this part of the experiment. PET-G samples thermoformed by the rigid concave tool with different duration of ultrasonic vibrations are shown in Figure 3.27. As it can be seen, all samples were well thermoformed, their cruciform structures are clear without obvious defects and unshaped areas are flat. With the duration of vibration increasing from 0.5 s to 2.0 s, thermoformed cruciform structures are essentially unchanged but the area of milling marks replicated from tools increased. This means that the foil can be thermoformed by the rigid concave tool in a wide time range.

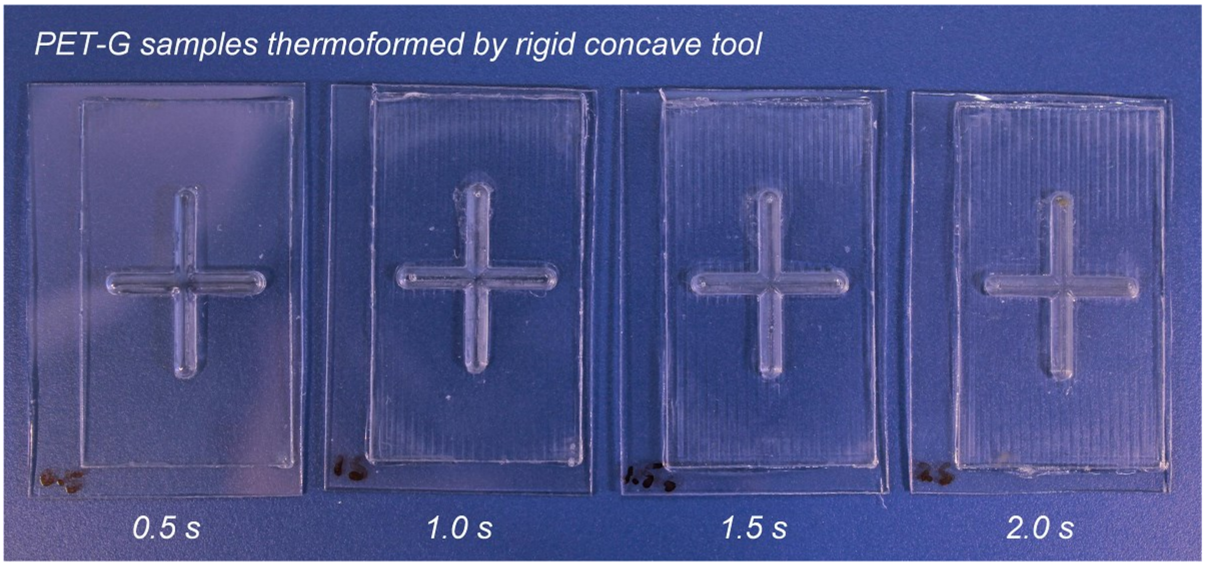

Figure 3.27: Photo of PET-G samples thermoformed by rigid concave tool with different duration of ultrasonic vibrations .

The cruciform structures from PET-G samples thermoformed with the flexible concave tool with different duration of ultrasonic vibrations (cf. Figure 3.28) are all distorted and none is well thermoformed. When fixing the flexible concave tool on the sonotrode, the foil thermoformed with a welding time of 0.3 s was heated and deformed owing to ultrasonic vibration and pressing force, yet not fully adapted to the shape of tools. With an increasing welding time, the height of thermoformed cruciform structure increased. However, there are more white dots on a larger area of the sample, especially at the tip of the cruciform, indicating overheat and decomposition of polymer material. This can be ascribed to the concentrated heat generation and unevenly distributed thermal energy during thermoforming. The heat generated is so concentrated that in some regions the polymer material was decomposed before it was thermoformed, while in other regions the material was not softened because ultrasonic vibrations did not generate enough heat. Besides, because the flexible tool is easily deformed by the pressing force, the geometry of the samples turned out to be rather uncontrollable.

PET-G samples thermoformed by fixing the flexible concave tool on the anvil (cf. Figure 3.28a) are similar to those with the flexible tool of on the sonotrode (cf. Figure 3.28b) when the duration of vibrations are the same. All samples of the former have white dots, while decomposition of polymer material happened in the latter only when the duration of vibration was longer than 0.5 s. Hence, the flexible concave tool has better heating capability when it’s fixed on the sonotrode than on the anvil.

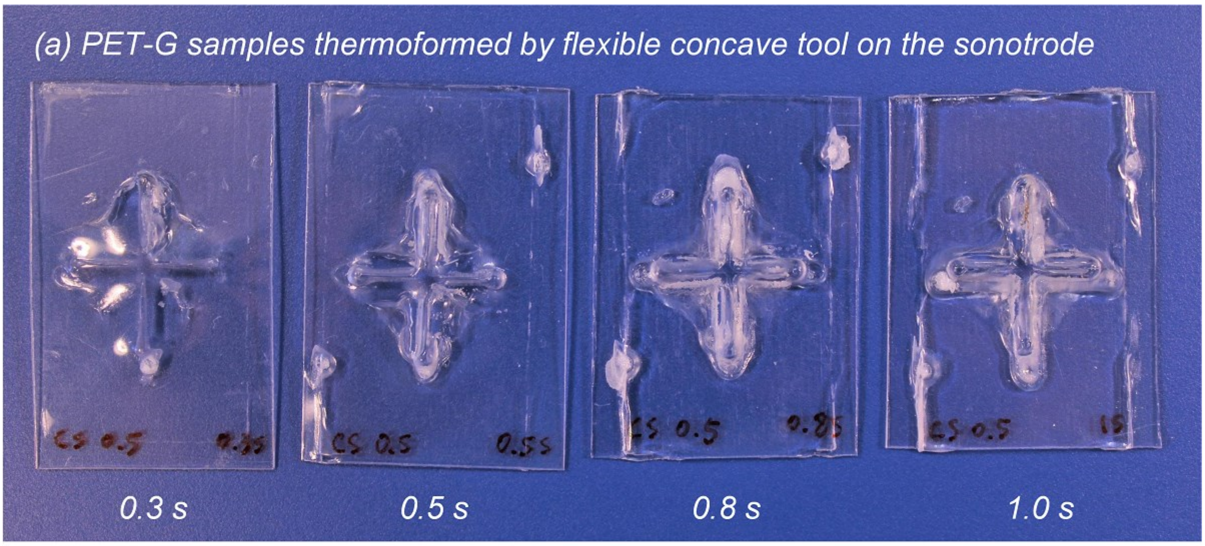
(a) PET-G samples thermoformed by flexible concave tool on the sonotrode

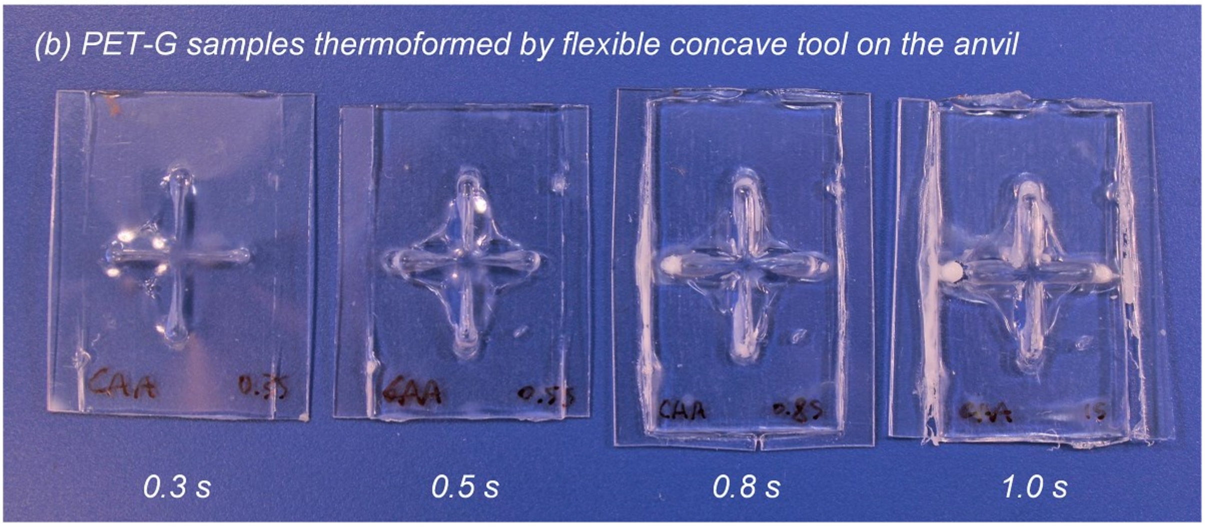
(b) PET-G samples thermoformed by flexible concave tool on the anvil

Figure 3.28: Photos of PET-G samples thermoformed by the flexible concave tool on the sonotrode (a) and on the anvil (b) with different duration of ultrasonic vibrations.

Photos of PET-G samples thermoformed by a combination of flexible flat tool and rigid convex tool are shown in Figure 3.29. Samples were either incompletely thermoformed or irregularly shaped. At the same duration of ultrasonic vibration, samples thermoformed by the flexible flat tool on the sonotrode (cf. Figure 3.29a) are obviously heated to higher temperature compare to the case with the flexible flat tool on the anvil (cf. Figure 3.29b).

Experimental comparisons revealed that the rigid tool is superior to the flexible tool in thermoforming PET-G foils, an amorphous thermoplastic. By comparing samples thermoformed by using a flexible concave tool (cf. Figure 3.28) and a flexible flat tool (cf. Figure 3.29), it can be concluded that the flexible concave tool exhibited a better heating capability than the flexible flat tool. This is attributed to the fact that friction and deformation were more concentrated on a concaved area than on a flat area. From the comparison of samples thermoformed by a flexible tool on the sonotrode (cf. Figure 3.28a, Figure 3.29a) and on the anvil (cf. Figure 3.28b, Figure 3.29b), the installation position of the flexible tool also made a difference in thermoforming foils. Flexible tools demonstrated better heating capability when they were fixed on the sonotrode.

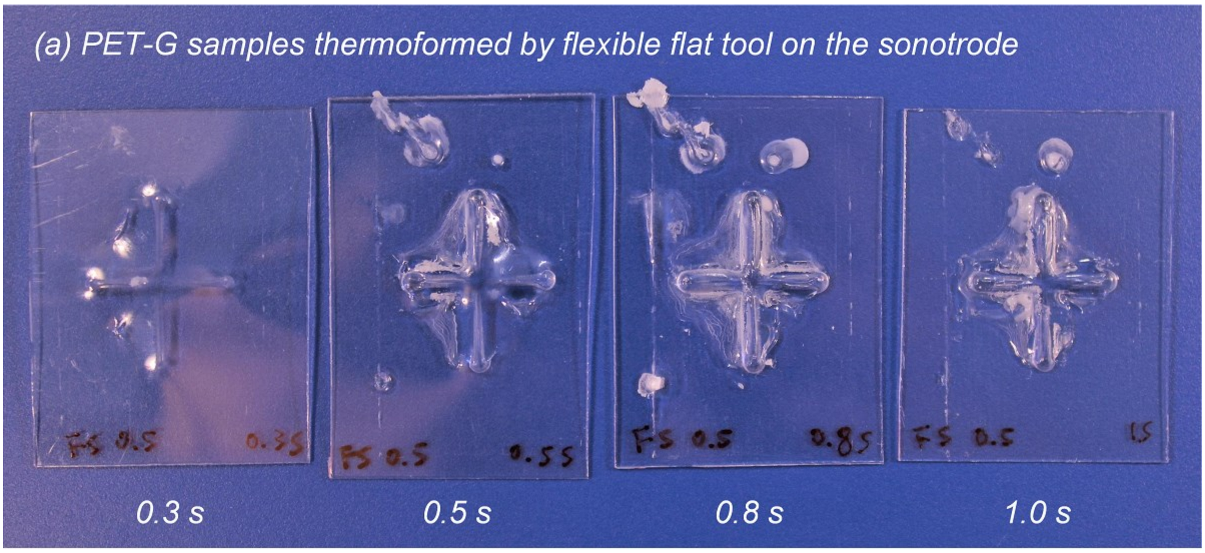
(a) PET-G samples thermoformed by flexible flat tool on the sonotrode

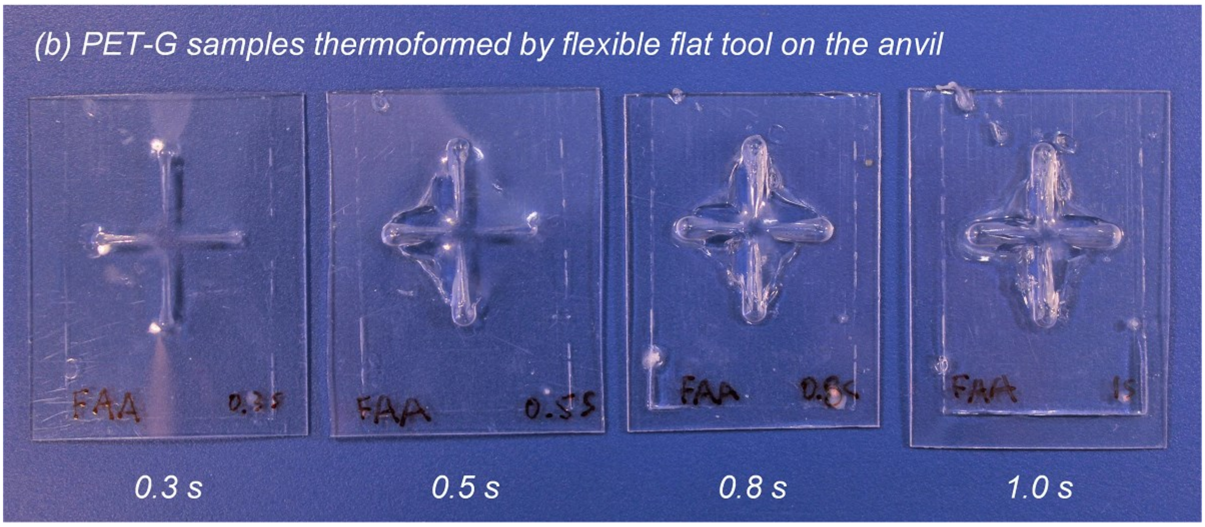
(b) PET-G samples thermoformed by flexible flat tool on the anvil

Figure 3.29: Photos of PET-G samples thermoformed by flexible flat tool on the sonotrode (a) and on the anvil (b) with different duration of ultrasonic vibrations.

Amorphous thermoplastics have a broad softening temperature and heating above its glass transition temperature (T_g) leads to a drop in the elastic modulus due to the decrease in viscosity. At this temperature, amorphous thermoplastics flow more easily and are hence easy to thermoform. This it is not the same for semi-crystalline thermoplastics, it begins to soften above T_g but does not exhibit fluid behavior until the melting temperature (T_m) is reached. So, semi-crystalline thermoplastics are more different to thermoform.

3.5.3 Ultrasonic thermoforming of semi-crystalline PP foils

Semi-crystalline thermoplastics may exhibit a different characteristic in thermoforming, therefore an example of a semi-crystalline polymers polypropylene (PP) was used for further comparison. A PP foil, with a thickness of 200 µm, was thermoformed by rigid concave tool, flexible concave tool, and flexible flat tool in this part of the experiment. Concave tools were fixed on the sonotrode. PP samples thermoformed by the unrounded rigid concave tool are presented in Figure 3.30. Obviously, with different durations of ultrasonic vibrations, cruciform structures on these samples have clear edges and same geometry as the tools. The unshaped area was flat and there are no ruffles caused by locally heating.

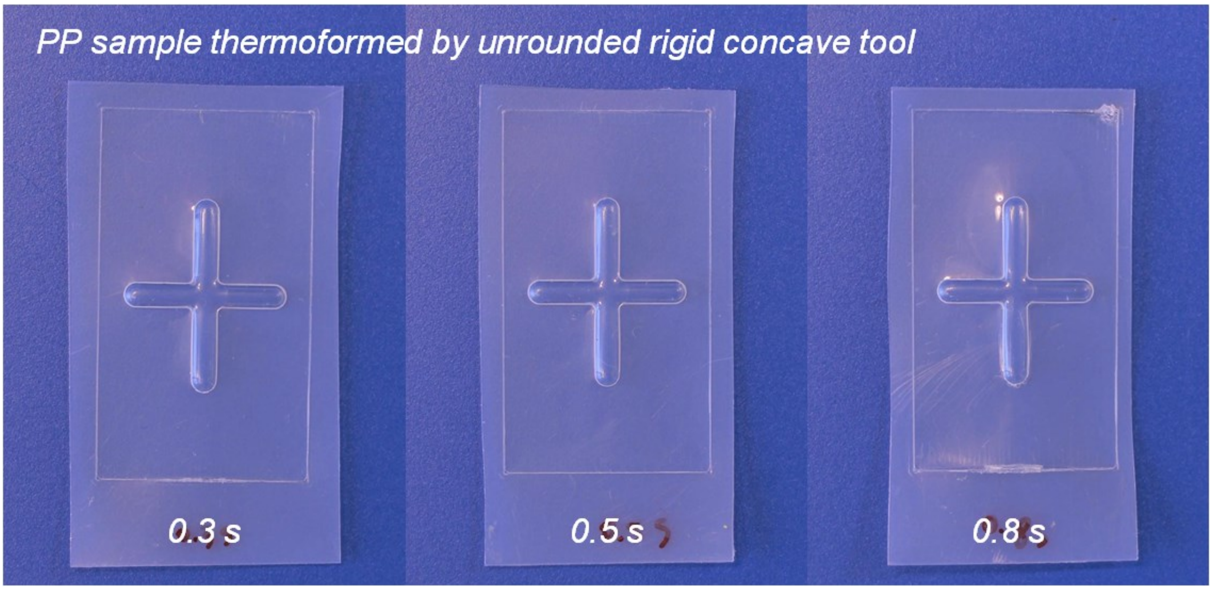

Figure 3.30: Photos of PP samples thermoformed by rigid concave tool with different duration of ultrasonic vibrations.

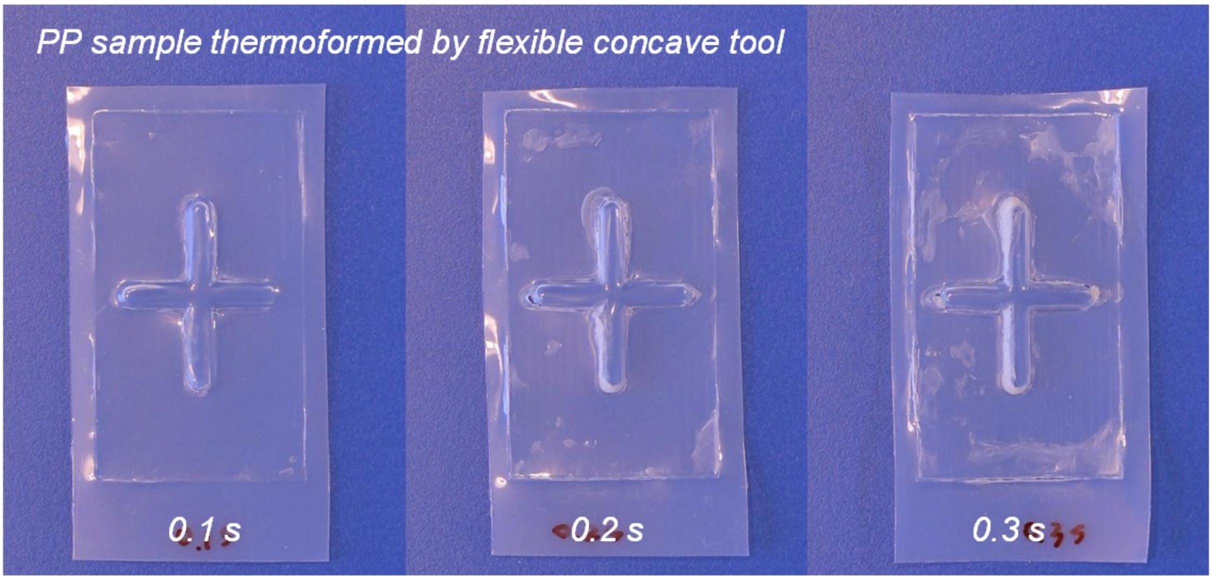

Figure 3.31: Photos of PP samples thermoformed by flexible concave tool with different duration of ultrasonic vibrations.

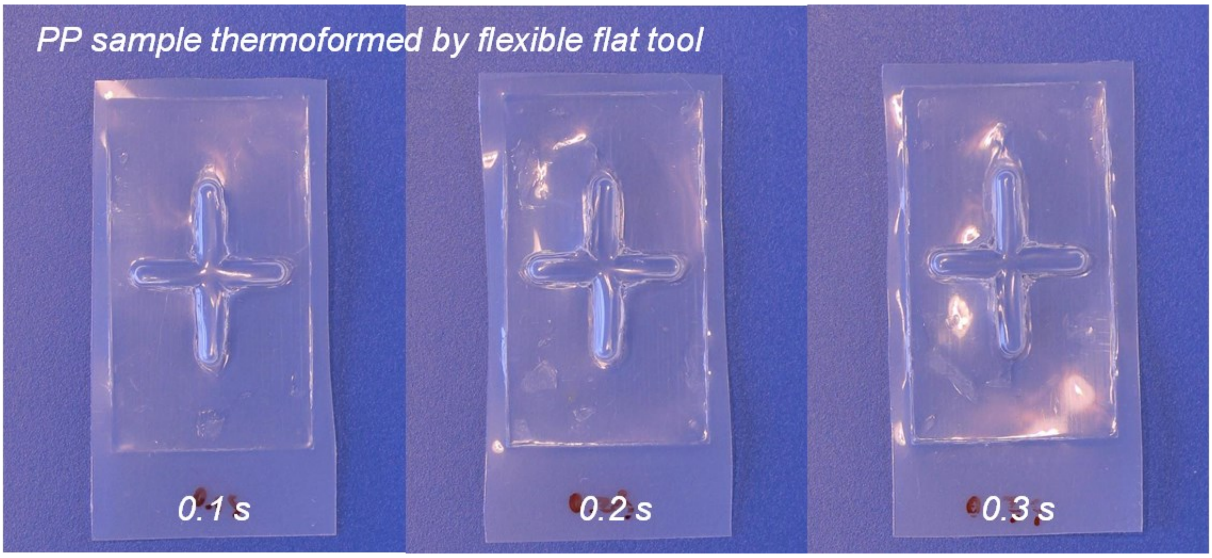

Figure 3.32: Photos of PP samples thermoformed by flexible flat tool with different duration of ultrasonic vibrations.

PP samples thermoformed by flexible concave tool and flexible flat tool are shown in Figure 3.31 and Figure 3.32, respectively. Cruciform structures on samples have elusive edges and all of them have cracks or holes along their edges. Besides, they are poorly thermoformed in the center. In unshaped regions, there is an increased opaque area in terms of both number and coverage with a longer duration of ultrasonic vibrations. A prolonged duration of vibration significantly increases generated heat; however, these heats were largely focused either on edges of the cruciform structure or on a limited area of the unshaped area. Concentrated thermal energy allows for locally melting or even overheating of polymer material, and finally leads to ruffles or white spots at these places.

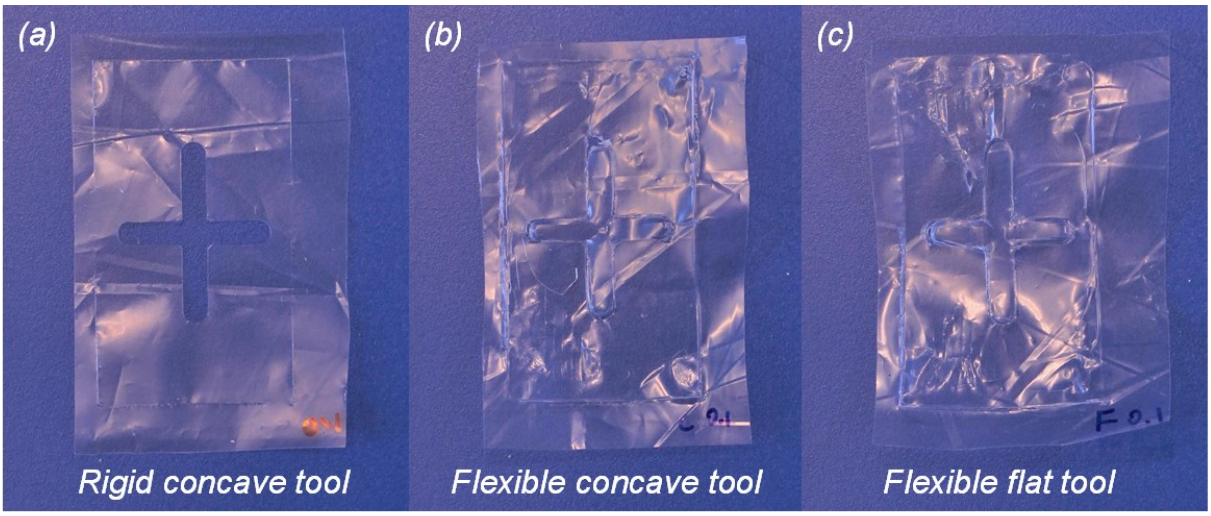

Figure 3.33: Photos of thermoformed PP foils with a thickness of 20 µm by rigid concave tool (a), flexible concave tool (b), and flexible flat tool (c).

3.5.4 Ultrasonic thermoforming of extra thin PP foils

A PP foil with a thickness of 20 µm was used to explore the possibility of thermoforming an extra thin foil. In Figure 3.33 there are three samples thermoformed by rigid concave tool, flexible concave tool, and flexible flat tool, respectively. The ultrasonic vibrations lasted for 0.1 s. The material in the center was punched out from the foil when using the rigid tool. Samples thermoformed using flexible tools (cf. Figure 3.33) are intact even though the cruciform structures were incompletely thermoformed and partly punched. It is expected that the flexible tool is capable of thermoforming this extra thin foil if structures on tools are well designed and thermoforming parameters are well adjusted.

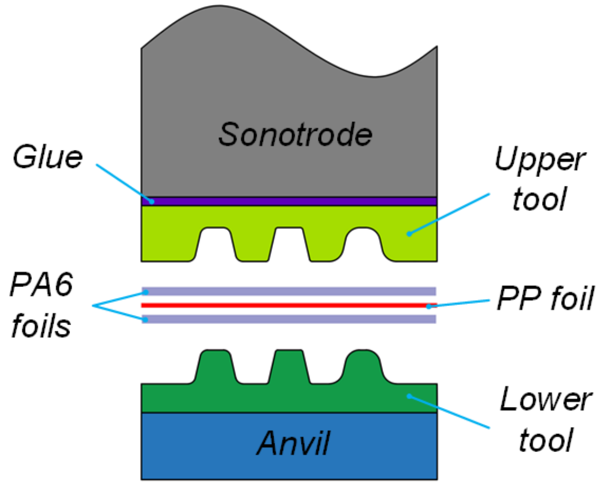

Figure 3.34: Placement of foils in ultrasonic thermoforming of extra thin PP foil.

To explore further the possibilities of ultrasonic thermoforming, an extra thin PP foil (20 µm in thickness) should be thermoformed. Attempts were made to thermoform such a thin foil without buffer foils but they all failed. The thermoformed extra thin foils were either punched or broken. Therefore, buffer foils were employed to protect the extra thin foil and to generate more friction heat in the near of it. The extra thin PP foil was sandwiched between two layers of PA6 foils, each 100 µm in thickness, and this stack of polymer foils was ultrasonically thermoformed as shown in Figure 3.34. PA6 was chosen because it cannot be ultrasonically welded with PP [9]. After ultrasonic thermoforming, the thermoformed PP foil was separated from the foil stack and the PA6 foils were discarded. When using the flexible tools at a pressing force of 600 N, several spots were decomposed. This can be attributed to the concentration of the ultrasound in these spots because of the flexible tool and the friction heat generated between the foils heating the stack from its inside. So the lowest possible pressing force was used to prevent decomposition. The pressing force, amplitude, trigger force, holding force, cooling time, and lower tool temperature were kept constant at 130 N, 20 µm, 130 N, 800 N, 3 s, and 22 °C, respectively.

Figure 3.35 shows the photos of PP foils thermoformed with buffer foils from PA6 by rigid and flexible tool with different durations of ultrasonic vibrations. As shown in Figure 3.35a, with buffer on both sides, the PP foils were well thermoformed. With increased duration of ultrasonic vibrations, there is not much difference between thermoformed cruciform structures. This is because the PP foil was pre-stretched by the rigid tool before ultrasonic vibrations began, and adapted to the shape of the tools for a duration of 3 s.

(a) Thermoformed by rigid concave tool

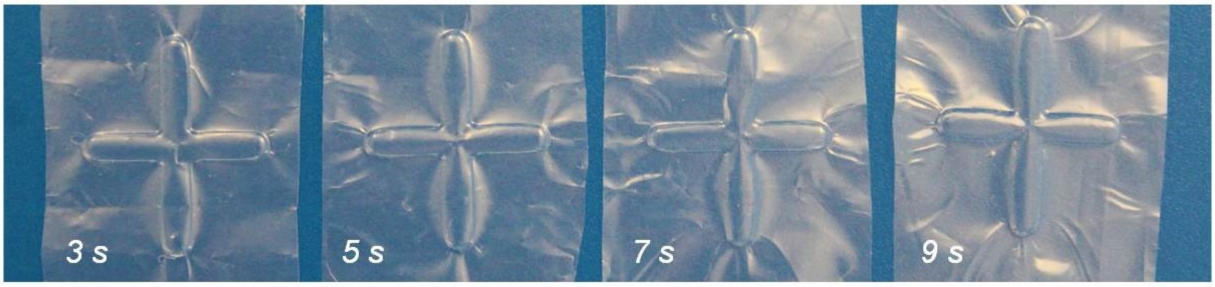

(b) Thermoformed by flexible concave tool

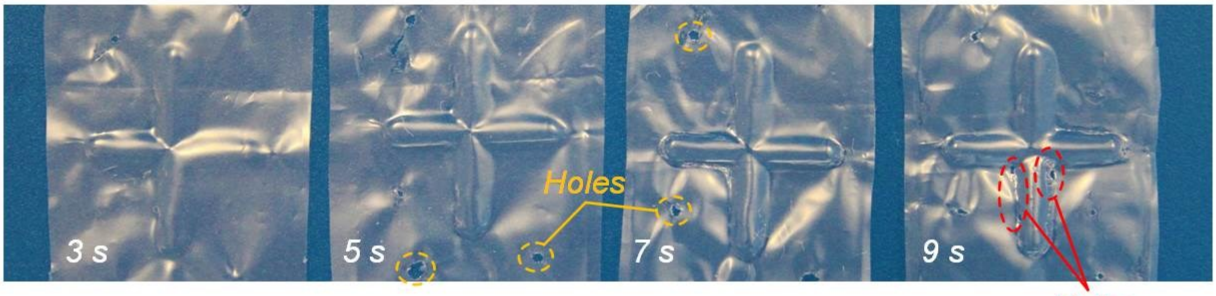

(c) Thermoformed by flexible flat tool

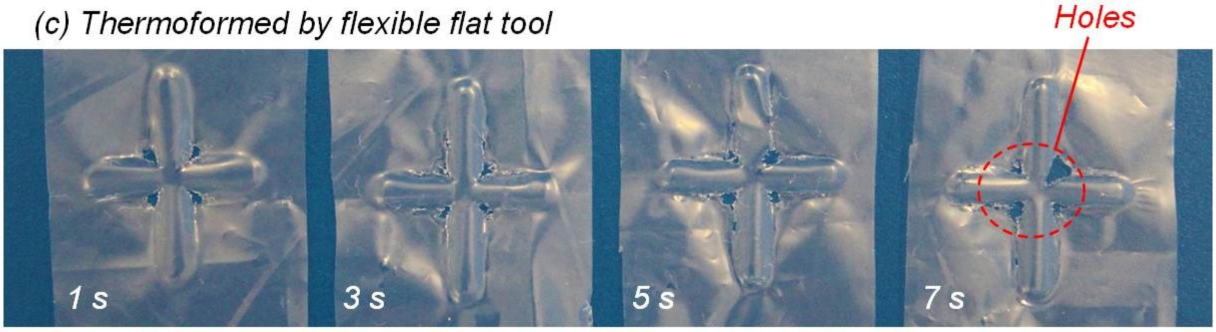

Figure 3.35: Photos of thermoformed 20 µm thick PP foils with help of buffer foils by rigid concave tool (a), flexible concave tool (b), and flexible flat tool (c) with different duration of ultrasonic vibrations.

The cruciform structure on PP foils were better thermoformed by the flexible concave tool with increased duration of ultrasonic vibrations (cf. Figure 3.35b). But a too long duration of ultrasonic vibration (i.e. 9 s) resulted in holes on the edge of the cruciform structure. The holes on unshaped areas of PP foils were mainly caused by holes on the flexible concave tool. These holes were formed after tens of uses. For PP foils thermoformed by the flexible flat tool, holes were generated located at four corners of the cruciform as shown in Figure 3.35c. Even though each cruciform structure was well adapted to the shape of tools, these holes make it inapplicable in practical use. In addition, the holes on PP foils thermoformed by flexible tools (cf. Figure 3.35 b, c) were probably both caused by the concentration of ultrasound in these spots.

Photos in Figure 3.36 show the tilted view of PP foils thermoformed by rigid tool and flexible tools with ultrasonic vibration duration of 7 s. In terms of the replicated shape of the cruciform structure, the PP foil thermoformed by flexible tools is superior to the one by the rigid tool. By adjusting thermoforming parameters, the PP foils thermoformed by the rigid tool were better adapted to the shape of the tools.

In principle, the rigid tool and flexible concave tool were able to thermoform extra thin PP foils with the help of buffer foils.

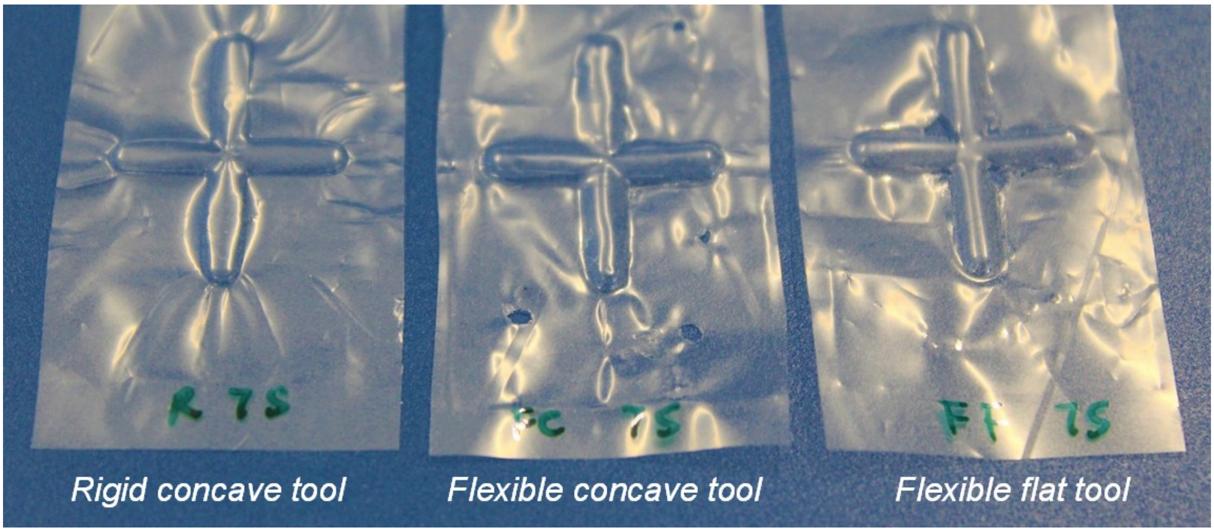

Figure 3.36: Photos (tilted view) of PP foils thermoformed by rigid concave tool, flexible concave tool, and flexible flat tool with same duration of ultrasonic vibrations.

All these results showed very large changes in the outcome of thermoformed foils from different tool materials, and these are attributed to large differences in the hardness of the tools.

The results of thermoforming PET-G foils (500 µm in thickness) and PP foils (200 µm in thickness) showed incomplete thermoforming for a combination of flexible concave tool and rigid convex tool, whereas complete thermoforming was achieved when both rigid concave and convex tool were used. There are limitations and problems in ultrasonic thermoforming using a flexible tool. Depending on the type of tools employed, neither two sides of the molding have a good replica of the tool geometry when using a flexible tool. Contours of surfaces on both sides are poorly defined as a result of stretching by an easily deformable flexible tool. Apart from this, using a flexible concave tool resulted in concentrated heat generation due to the elastic deformation of the flexible tool during ultrasonic thermoforming. By contrast, rigid tools demonstrated much better capability in thermoforming PET-G foils and 200 µm thick PP foils as illustrated previously. Rigid tools are a better choice for thermoforming both semi-crystalline and amorphous thermoplastics.

Thermoforming an extra thin PP foil (20 µm in thickness) is another scenario. It is almost impossible to thermoform a extra thin PP foil by the rigid concave tool with this cruciform structure or by flexible tools. With buffer foils on both sides, an extra thin PP foil was thermoformed by the rigid tool and the flexible concave tool.

3.6 Influence of the installation location of tools

As mentioned in chapter 1.3.3, there are two configurations of fixing detachable tools. Ultrasonic waves are indirectly transferred to the polymer foil through the tool fixed on the tip of the flat sonotrode. To investigate the influence of the installation location of the tools, two parts of experiments were performed. In the first part, the convex tool was glued on the sonotrode and the concave tool was fixed on the anvil. In the second part, the positions of the convex and concave tool were exchanged. And the process windows of the different installation positions were compared and analyzed.

The tools for experiments described here are shown in Figure 3.37. As can be seen, there are protruding structures with different dimensions and geometry on the convex tool and their inverse structures on the concave tool. Besides this, micro grooves surrounding protruding structures on the convex tool are filled with melted polymer during ultrasonic thermoforming, generating energy directors after cooling. These energy directors served as indicators to determine whether the foil is fully thermoformed.

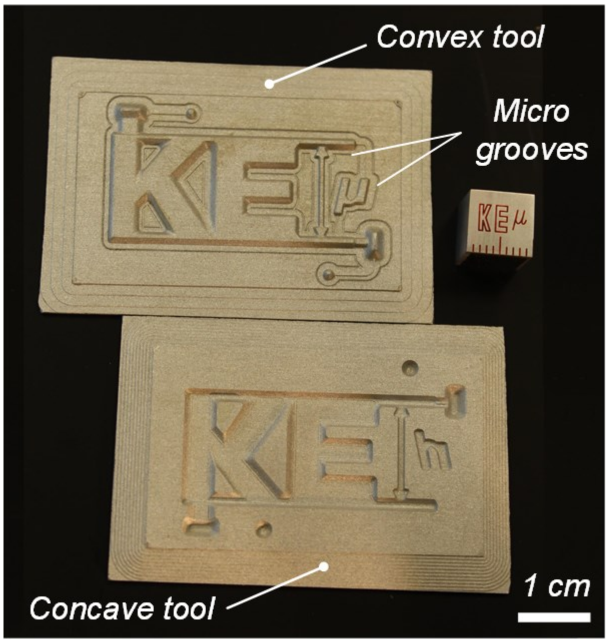

Figure 3.37: Convex tool and concave tool.

A PET-G foil, 500 µm in thickness, was used in all experiments. During thermoforming, the tool fixed on the anvil was preheated to 45 ºC. The peak-to-peak amplitude was varied from 3 µm to 30 µm in increments of 3 µm. The pressing force was starting from 130 N, and then varied from 200 N to 800 N in increments of 100 N. 130 N is the minimum pressing force this ultrasonic welding machine can provide. The welding time was kept constant at 4 s. And the cooling time and holding force were kept constant at 10 s and 800 N, respectively, ensuring complete hardening of the thermoforming foils before demolding.

Figure 3.38: A good sample fabricated by ultrasonic thermoforming.

The good and failure samples are shown in Figure 3.38 and Figure 3.39. As shown in Figure 3.38, a good sample should be completely well-formed and without any damage, brittle, or broken regions.

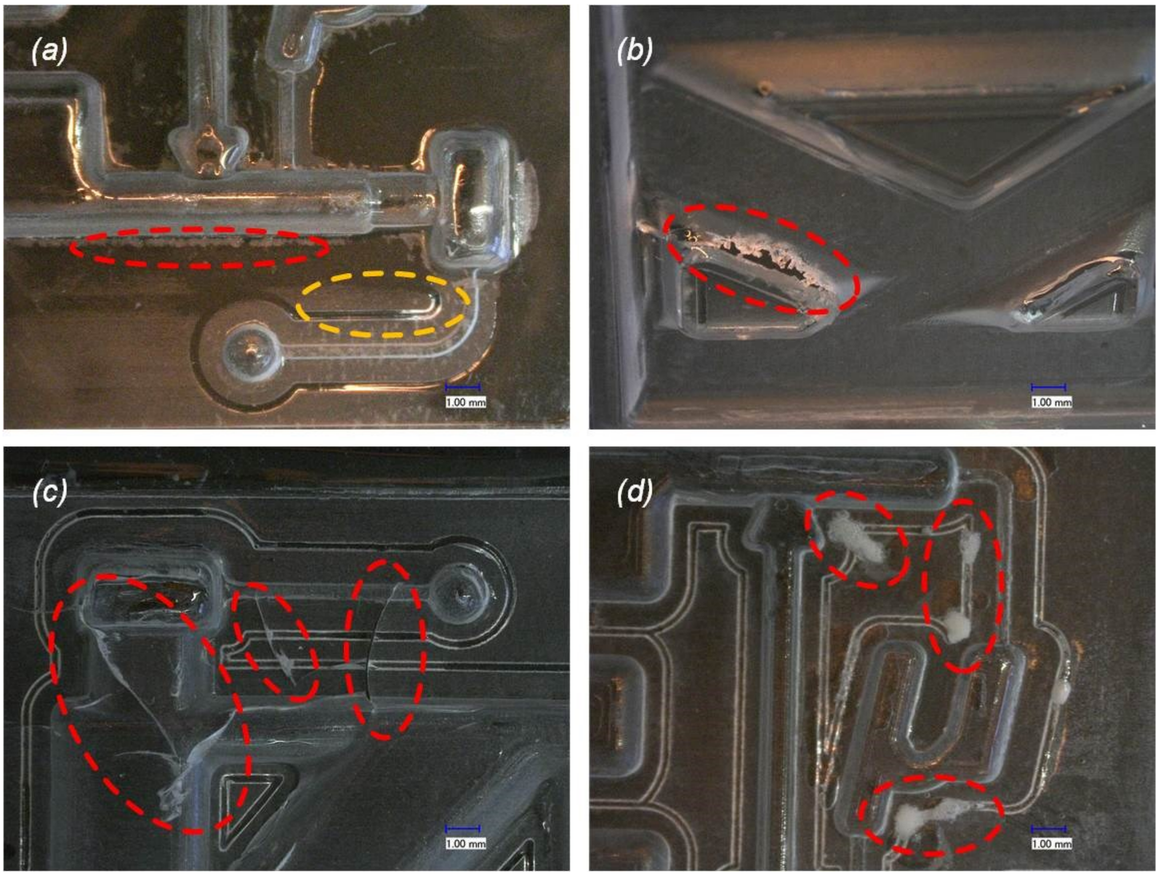

Figure 3.39: Failure samples: Incomplete (a), broken (b), brittle (c), and damaged (d).

Typical failure samples include incomplete samples on which some structures and/or energy director were not fully thermoformed (cf. Figure 3.39a), broken when the foil was broken and/or holes were formed (cf. Figure 3.39b), brittle when the sample fractured during or after demolding (cf. Figure 3.39c) and damaged when a white spot was observed on the polymer foil due to decomposition of the molecules of the polymer (cf. Figure 3.39d).

3.6.1 Process windows with different installation location of the tools

For the first part of the experiment, the convex tool was glued on the sonotrode and the concave tool was fixed on the anvil, as shown in Figure 3.40. During ultrasonic thermoforming, ultrasonic waves were transferred to the PET-G foil through the glue layer and convex tool.

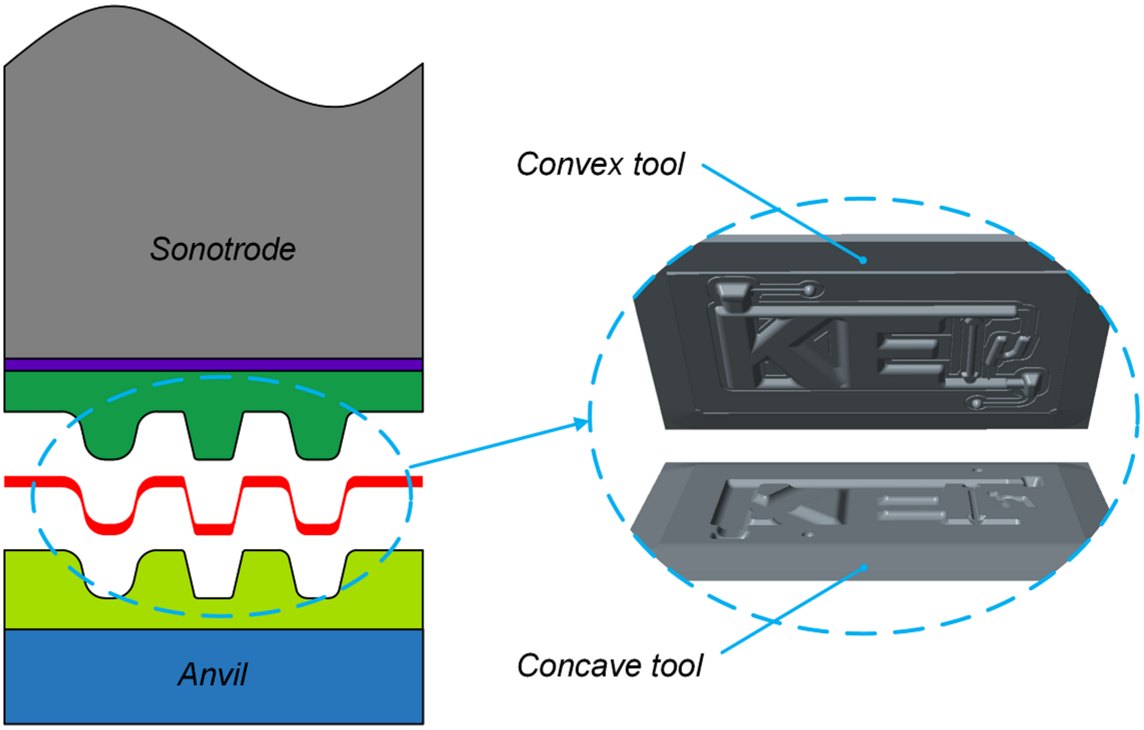

Figure 3.40: Convex tool on the sonotrode, concave tool on the anvil.

The pressing force and amplitude were varied to find out the limits between incomplete, good, broken, brittle, and damaged thermoforming as shown in Figure 3.41. The signs marking errors in the figure mean that the ultrasonic welding machine reported the frequency was below the limit, often caused by a too high pressing force and/or a too low amplitude.

Samples were incompletely thermoformed (cf. Figure 3.39a) at pressing forces of 130 N and 200 N because insufficient heat was generated to melt the polymer foil with such low pressing force. Hence, the micro grooves on the convex tool (cf. Figure 3.37) were not completely filled with polymer melt causing the incomplete samples.

With increased pressing force, the thermoformed polymer foil was broken (cf. Figure 3.39b). This often happened at the sidewall of the thermoformed foil which could be caused by the so-called hammering effect. In an ideal welding process in which the sonotrode was permanently in contact with the polymer foil, the amplitude of vibration could be expected to be more influential in overall heat generation than the pressing force. However, the sonotrode at times lost contact with the polymer foil during the vibration phase of the process [56], which is the hammering effect. The hammering effect is particularly sensitive to the pressing force, as the pressing force decreases the hammering effect has been observed to significantly increase [20]. This is confirmed by the fact that the broken parts vanished when the pressing force was increased as shown in Figure 3.41.

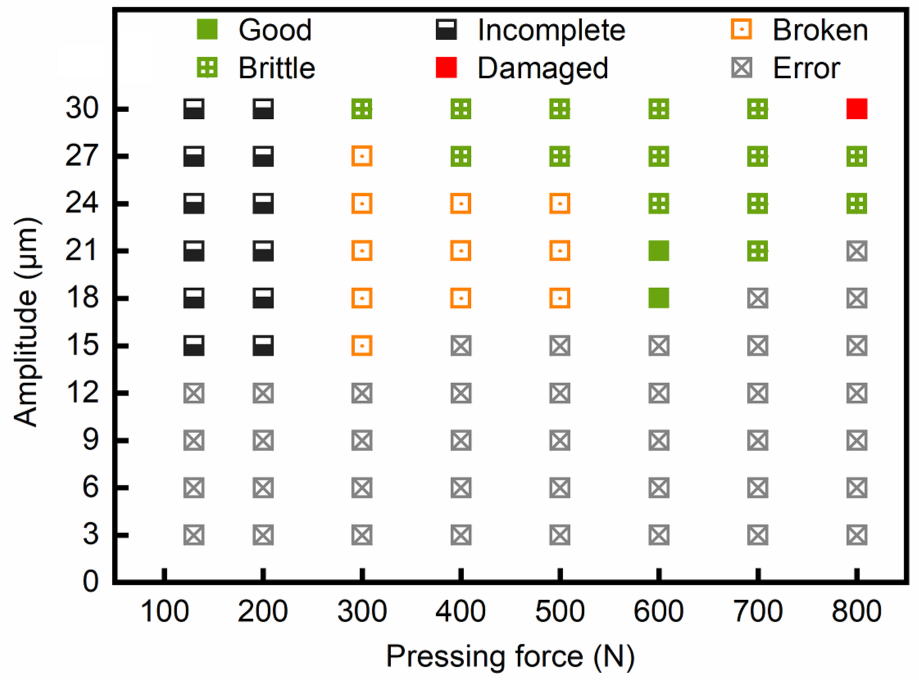

Figure 3.41: Process window of ultrasonic thermoforming when the convex tool was fixed on the sonotrode and the concave tool on the anvil.

Loss of contact reduces the coefficient of friction, so that the slightest deviation from parallelism is sufficient to push the foil in a lateral direction. For the sloped sidewalls on tool and foil in this experiment, a combination of vertical vibration and lateral movement leading to the collision and rub between tools and foil. That is why some polymer particles appeared near the broken hole, as shown in Figure 3.39b. It was estimated that the actual amplitude transmitted to the foil is drastically reduced by the hammering effect, as low as 13% of the nominal amplitude [57]. Consequently, less heat was generated during the whole process.

At the pressing force of 600 N and amplitude in the range of 18 to 21 µm, the structures and energy director on the thermoformed polymer foil are clear and intact (cf. Figure 3.38). The good samples were thermoformed with these parameter combinations. Especially, a greater pressing force causes more flow of heated polymer out of the thermoformed zone to form the energy director, due to the combined effects of higher temperature and greater stresses.

When the amplitude reached a higher level, for instance, the sample thermoformed with a pressing force of 300 N and amplitude of 30 µm, the polymer foil was getting brittle and prone to be torn (cf. Figure 3.39c). This could be caused by an overheating of the polymer foil. So, three parameter combinations were selected to thermoform foils with shorter welding time, as shown in Table 3.2. Good samples were obtained by applying ultrasonic vibrations shorter than prescribed 4 s. With a ultrasonic vibration time shorter than 4 s the overheating of polymer foils was avoided.

Table 3.2: Ultrasonic thermoforming parameters with shorter durations of vibration

No.	Pressing force	Amplitude	Welding time for good sample
1	300 N	30 µm	3.9 s
2	700 N	21 µm	3.1 ~ 3.5 s
3	800 N	27 µm	2.3 ~ 2.6 s

The damaged sample was obtained when the amplitude and pressing force were 30 µm and 800 N, respectively. When the foil temperature was too high and exceeded the decomposition temperature of the polymer, the polymer foil was decomposed in some regions. After cooling down, opaque regions in the thermoformed foil were observed (cf. Figure 3.39d).

For the second part of the experiment, the installation positions of the aluminum tools were exchanged. So that the concave tool was glued on the sonotrode and the convex tool was fixed on the anvil, as shown in Figure 3.42. During ultrasonic thermoforming in this part, ultrasonic waves were transferred to the PET-G foil through the glue layer and concave tool.

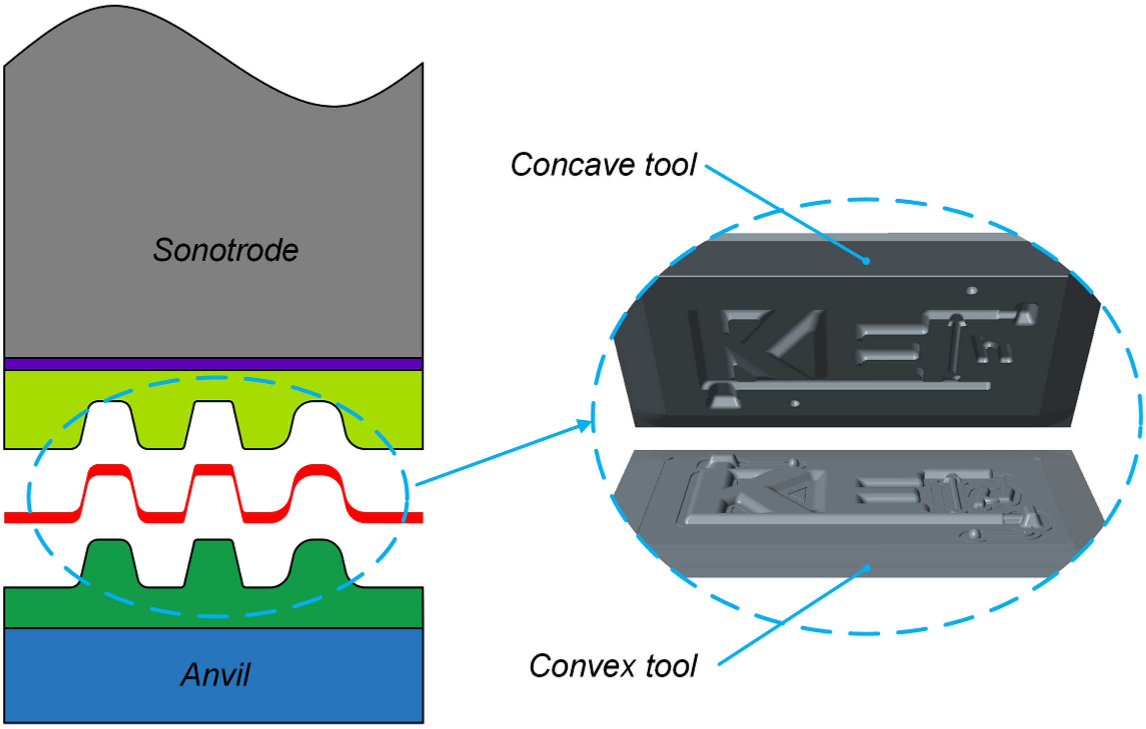

Figure 3.42: Concave tool on the sonotrode, convex tool on the anvil.

Comparing Figure 3.43 with Figure 3.41, there is not much difference between process windows of ultrasonic thermoforming with inversely installed tools. With this arrangement of tools, the good sample was thermoformed by the amplitude of 21 µm and a higher pressing force of 700 N than in the first part of the experiment.

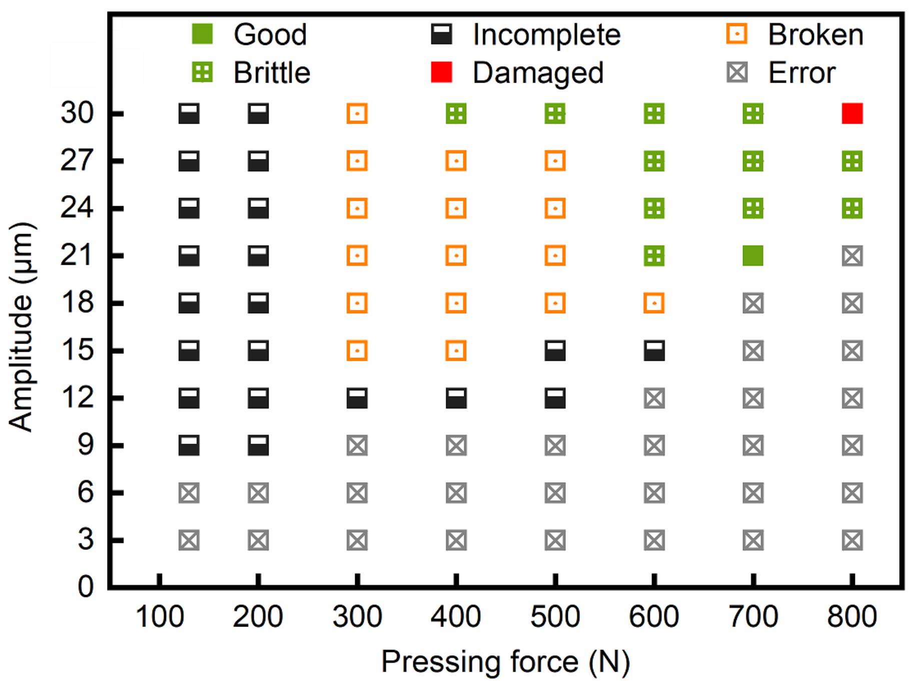

Figure 3.43: Process window of ultrasonic thermoforming when the concave tool was fixed on the sonotrode and the convex tool on the anvil.

The determinant of thermoforming a good sample in these experiments is the formation of the energy director. In most cases, an energy director is necessary for the subsequent ultrasonic welding when ultrasonically fabricating a microsystem. For the tools designed in this experiment, other structures were formed by protruding structures on the convex tool and their inverse structures on the concave tool. The energy directors, on the other hand, go in the other direction. It needs enough melted polymer flow to fill the micro grooves on the convex tool. If the temperature of the foil is too low, the energy director cannot be completely formed. However, when the temperature of the foil is too high, the polymer on some regions of the foil will decompose. Even though, in both cases, other structures were well thermoformed with some parameter combinations. The temperature of the foil needs to be just right for each case to get a good sample. So further investigations of reasons for the difference in process windows of ultrasonic thermoforming with inversely installed tools were conducted.

3.6.2 Temperature distribution of tools and thermoformed foils

To observe the temperature distributions of tools with inverse installation locations, an infrared camera THT70 from HT Instruments GmbH, Germany was used. The foils were thermoformed with an amplitude of 21 µm and pressing force of 700 N for 4 s without tool preheating, to exclude other heat sources. The aluminum tools were removed from the ultrasonic welding machine after each experiment, and then thermal photos of their surfaces were captured. This experiment was performed three times for both installation positions. Thermal photos were taken about 5 s after the thermoforming processes. The infrared camera was located approximately 25 cm above the used tools.

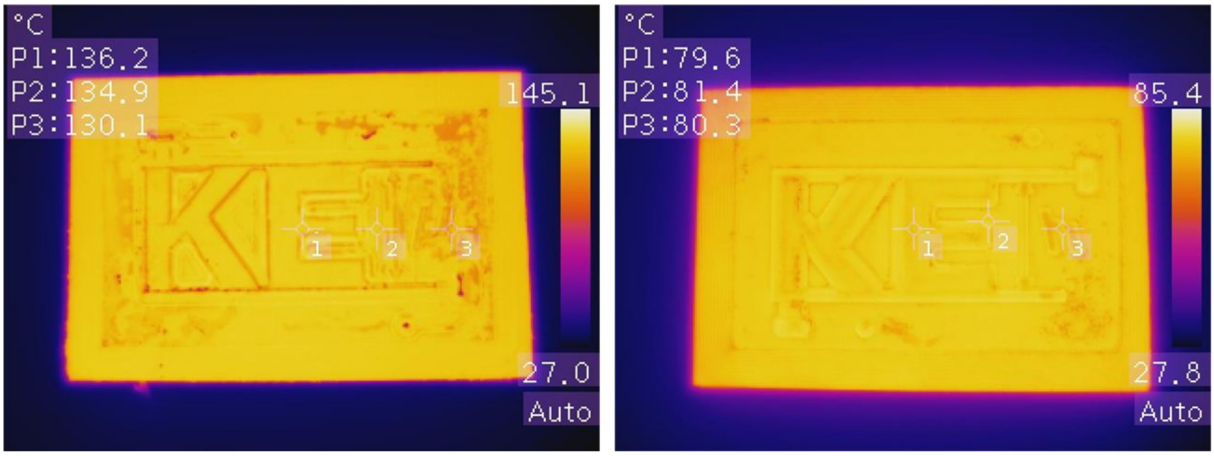

(a) Convex tool on the sonotrode *(b) Concave tool on the anvil*

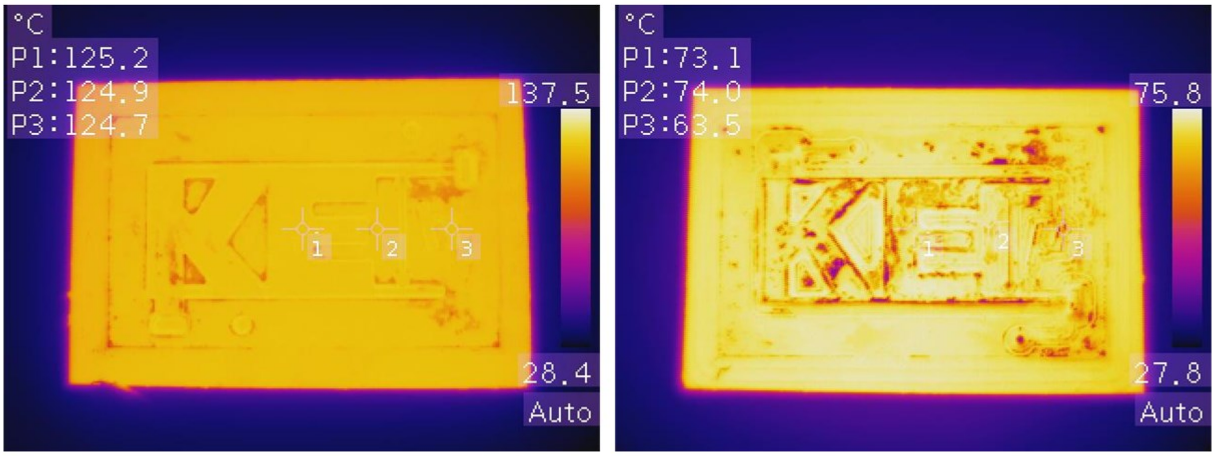

(c) Concave tool on the sonotrode *(d) Convex tool on the anvil*

Figure 3.44: Thermal photos taken after the first part of the experiment with the convex tool on the sonotrode (a) and the concave tool on the anvil (b), and the second part of the experiment with the concave tool on the sonotrode (c) and the convex tool on the anvil (d).

Figure 3.44 shows the photos of the temperature of the first part of the experiment with the convex tool on the sonotrode (Figure 3.44a) and the concave tool on the anvil (Figure 3.44b), and in the second part of the experiment with the concave tool on the sonotrode (Figure 3.44c) and the convex tool on the anvil (Figure 3.44d). Their highest temperatures were 145.1 °C, 85.4 °C, 137.5 °C, and 75.8 °C, respectively. Comparing thermal photos Figure 3.44 a with b, and c with d, respectively, shows that the tools got hotter when they had been fixed on the sonotrode, their maximum temperatures were about 60 °C higher than the ones fixed on the anvil. At the same time, if the convex tool had been fixed on the sonotrode, its maximum temperature (145.1 °C, as shown in Figure 3.44a) was 7.6 °C higher than the concave tool had been fixed on the sonotrode (137.5 °C, as shown in Figure 3.44c). The corresponding maximum temperature of the concave tool on the anvil (85.4 °C, as shown in Figure 3.44b) was also 9.6 °C higher than that of the convex tool on the anvil (75.8 °C, as shown in Figure 3.44d). Furthermore, the temperature of the tool surface was not evenly distributed according to these thermal photos.

According to the temperatures on points P1-3 of each tool in Figure 3.44, the temperature difference of each tool was about several degrees, and the temperature in the center was generally higher than in the surrounding area. Hence, the tool fixed on the sonotrode got tens of degrees hotter than the one fixed on the anvil. Both tools got several degrees hotter if the convex tool had been fixed on the sonotrode compared to fixed on the anvil.

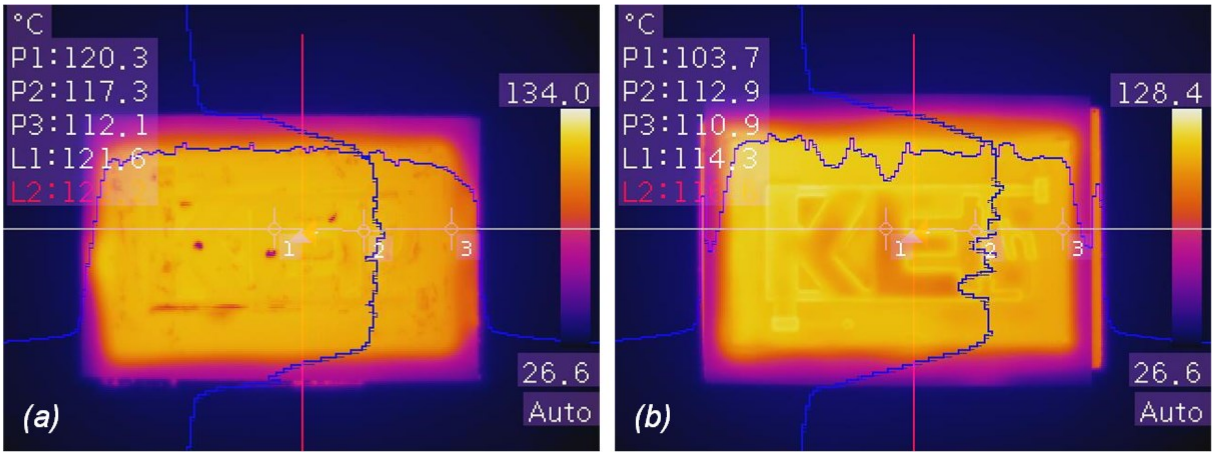

Figure 3.45: Temperature distribution of a thermoformed foil with the convex tool (a) and the concave tool (b) on the sonotrode.

The thermal photos of the thermoformed PETG foils were captured from the surface facing the anvil. These two foils were thermoform with the convex tool and the concave tool on the sonotrode, respectively. Their temperature distributions are shown in Figure 3.45. The maximum temperature of the thermoformed foil was 5.6 °C higher when the convex tool had been fixed on the sonotrode than fixed on the anvil. A rectangular area in the center was thermoformed; hence its temperature was obviously higher than peripheral areas. The thermal photos demonstrate that the temperature of the thermoformed areas were not homogeneously distributed, it correlated to the shape of the structures. The temperature along the horizontal line L1 and the vertical line L2 in Fig. 3.45 are also presented. The differences within the thermoformed area along line L1 and L2 were in the order of several degrees (cf. Figure 3.45a) with the convex tool on the sonotrode, whereas it got larger (cf. Figure 3.45b) with the concave tool on the sonotrode.

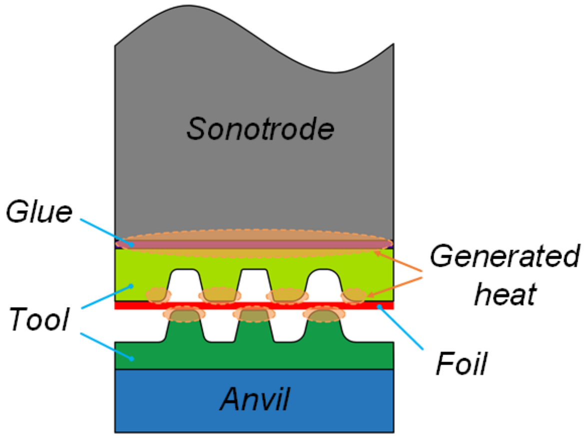

Figure 3.46: Heat generated at different regions during ultrasonic thermoforming.

As shown in Figure 3.46, if the tool was fixed on the sonotrode, friction heat generated between glue, sonotrode, and tool could also contribute to the temperature rise. While the tool fixed on the anvil was only heated by the friction between tool and polymer foil.

With additional heat generated on the side of the foil near the sonotrode, the foil surface facing the sonotrode got more temperature rise and was easier softened. To fill the micro grooves on the convex tool by melted polymer is harder than simply thermoform other structures by protruding structures on the convex tool and their inverse structures on the concave tool. Therefore, the good samples were ultrasonically thermoformed by less pressing force and amplitude when fixing the convex tool on the sonotrode.

According to previous results, it is better to fix the tool on the sonotrode if that tool thermoforms an energy director or structures alike in another designs. As described in chapter 2.1.1, pressing force and amplitude have an appreciable effect on the heating rate, both at the interface and within the interior of the foil. The heating rate at the pressing force of 600 N and amplitude in the range of 18 to 21 µm is suitable for 500 µm thick PET-G foils. This parameter combination can be used in ultrasonic thermoforming of other designs by just varying the duration of vibrations when using the same foil.

4. Microsystems integrated with electrical elements

4.1 Integrating LEDs into micro channels

To explore the possibility of fabricating microsystems, especially microfluidics, by ultrasonic thermoforming, LEDs were integrated into micro channels and cavities with different dimension, geometry, and connection. By ultrasonic thermoforming, micro channels and cavities were fabricated from thermoplastic polymer foils. LEDs were welded in between two thermoformed foils by ultrasonic welding.

The design is the logo “KEµ” composed of two major cavities, as shown in Figure 4.1. The blue lines surrounding the construction mark micro protruding structures on the other side, 200 µm in height. They are employed as energy directors for subsequent ultrasonic welding with a flat foil. LEDs were placed in the LED chambers beforehand and then fixed in the chambers during ultrasonic welding. At the same time, cavities and micro channels were sealed by energy directors melted during ultrasonic welding and bonding the two foils. The micro channels, 200 µm in width and depth, connect each individual cavity, and serve as a passage for liquids inside them. Thereafter, liquids were injected from the inlet.

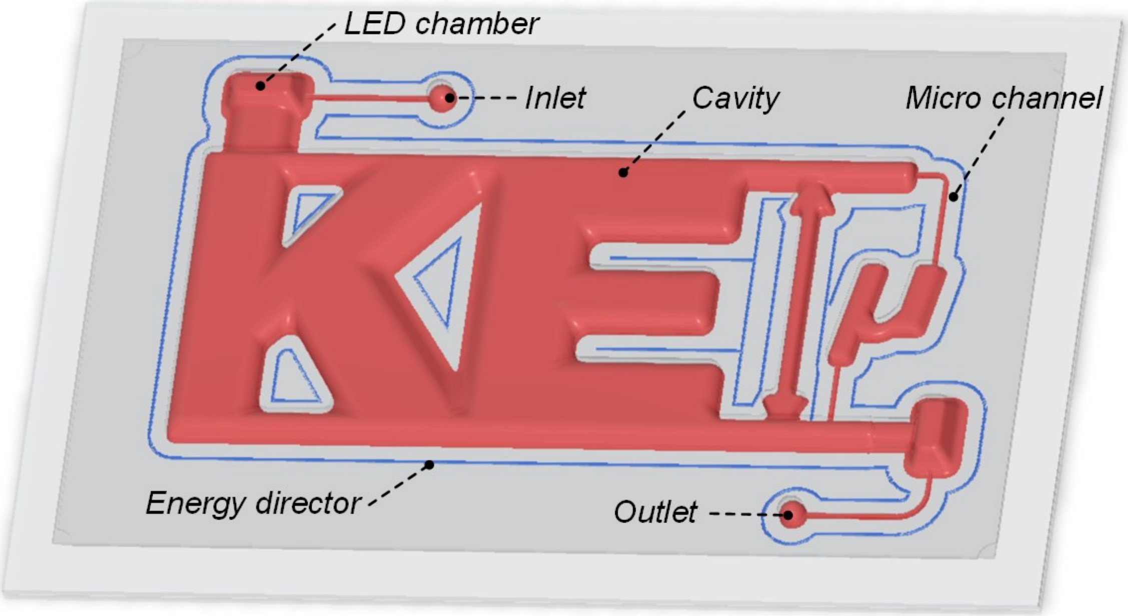

Figure 4.1: Design with the logo ‘KEµ’.

The tools (cf. Figure 4.2) used for ultrasonic thermoforming were milled into aluminum plates, 40 mm × 60 mm × 4 mm in width, length, and thickness, respectively. Micro grooves surrounding the protruding structures on the convex tool were filled with melted polymer during ultrasonic thermoforming generating energy directors after cooling.

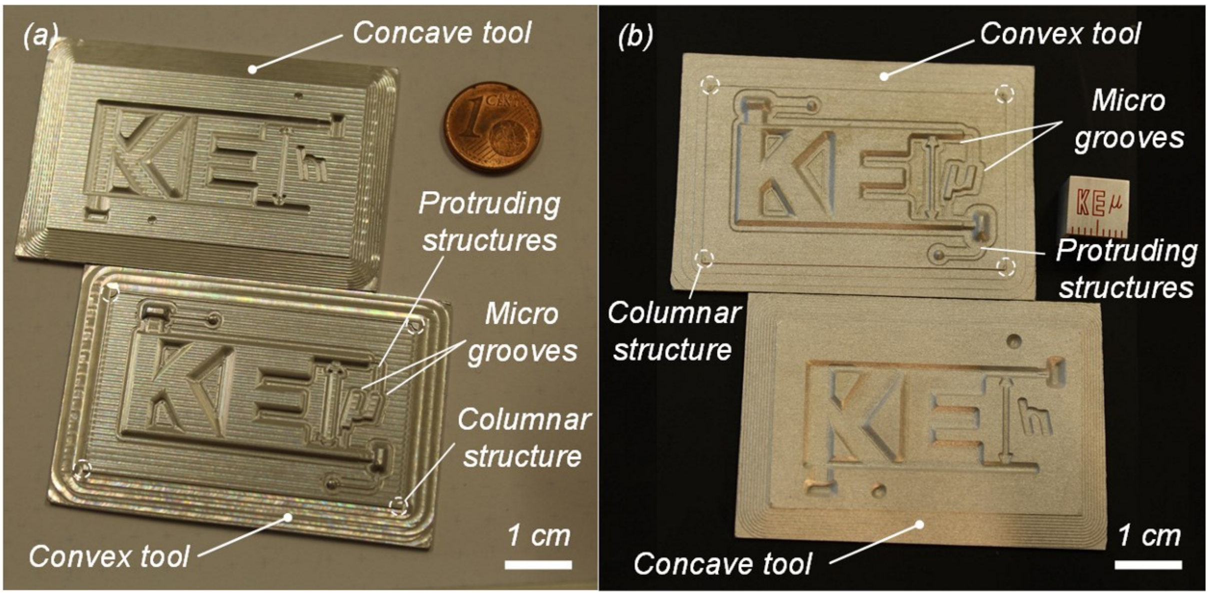

Figure 4.2: Aluminum tools before (a) and after (b) electro-polishing.

As shown in Figure 4.3, narrow (200 µm wide) protruding structures were ultrasonically hot embossed into the polymer foil generating 200 µm deep micro channels. Since there are no inverse structures on the concave tool, these narrow protruding structures can hardly withstand the powerful vibration and pressing force. It is necessary to prevent a direct contact of these structures with the concave tool which could be punched through the polymer foil. To protect the narrow protruding structures during ultrasonic thermoforming, columnar structures with the same height (that is 200 µm) and a diameter of 2 mm were designed at four corners of the convex tool.

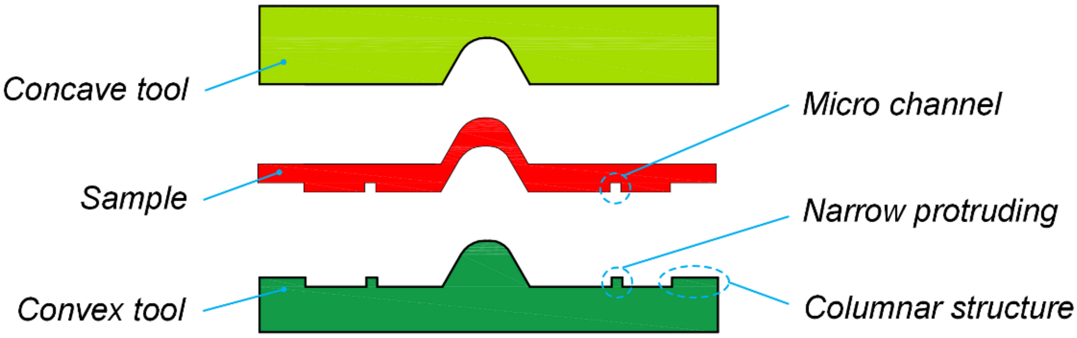

Figure 4.3: Schematic drawing of the cross-section of tools and sample.

All vertical micro structures on the tools were rounded with radii of 0.8 mm and slope angles of 25°, so that the surfaces of the tools are continuous and smooth facilitating thermoforming and demolding.

To reduce surface roughness of thermoformed foils and to ease demolding, the milled tools were electro-polished. By removing a thin layer of material from the aluminum tool, electro-polishing reduces tools' surface roughness by levelling micro-peaks. The electro-polishing was performed with the aforementioned milled tools as an anode and a stainless steel plate as a cathode in an electro-polishing solution, in which the volume ratio of phosphoric acid to pure water is 1:3 at a constant temperature of 75 °C. The electrical field is larger at peaks on the surface enhancing etching. A power supply was used to provide a constant current density of 0.1 A/cm^2. After electro-polishing for 1 minute, the polished tool was taken out of the solution and rinsed thoroughly with water. As seen in Figure 4.2a, there are seen milling marks which vanished by electro-polishing (Figure 4.2b).

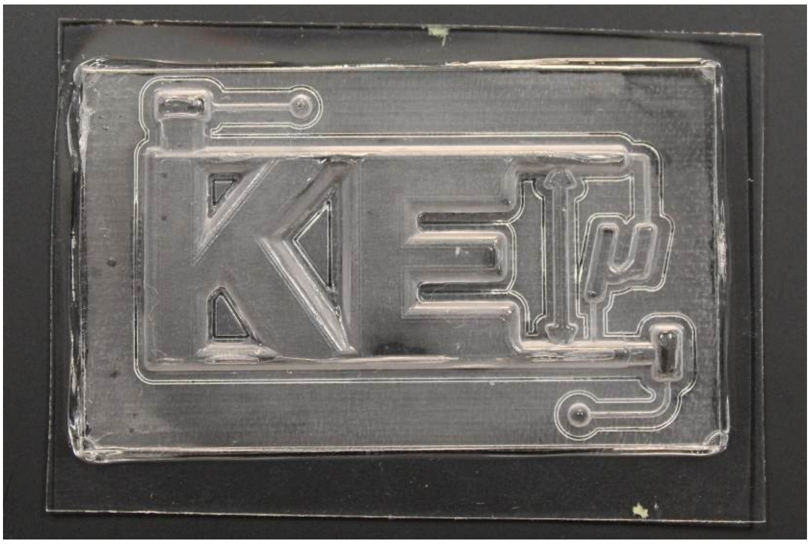

Figure 4.4: Thermoformed foil with structures for cavities and micro channels.

A PET-G foil, 500 µm in thickness, was used to thermoform a foil with structures for cavities and micro channels. According to the results of chapter 3.4, the convex tool was glued to the sonotrode. The concave tool was fixed on the anvil and preheated to 45°C. Pressing force, peak-to-peak amplitude, welding time, cooling time, and holding force were 600 N, 20 µm, 4 s, 10 s, and 800 N, respectively. In Figure 4.4, a good sample is shown completely well-formed and without any damage, brittle or broken regions.

The thermoformed foil was welded to a flat foil by ultrasonic welding. In the welding process, the concave tool was fixed on the anvil and the thermoformed foil (cf. Figure 4.4) was placed onto the concave tool. Pressing force, peak-to-peak amplitude, welding time, cooling time and holding force were 1000 N, 20 µm, 0.2 s, 1 s, and 600 N, respectively. The trigger force was 950 N ensuring that the two foils were firmly pressed to avoid sliding between them.

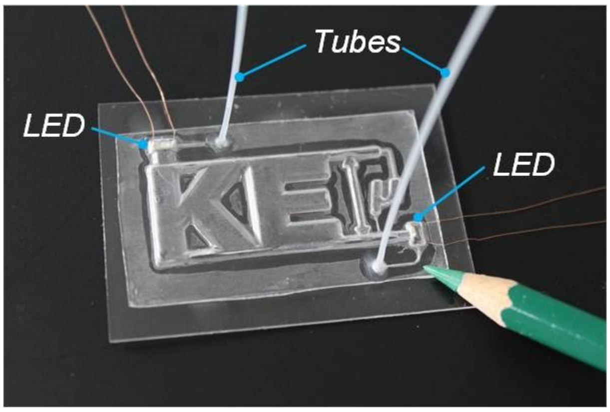

Figure 4.5: Ultrasonic welded sample with integrated LEDs.

LEDs were horizontally placed in the LED chambers of the thermoformed foil with their light-emitting surfaces facing to the designed logo ‘KEµ’, as shown in Figure 4.5. After ultrasonic welding, all energy directors on the thermoformed foil were completely melted to bond the two foils, and there is no congestion in micro channels. Orifices with a diameter of 1 mm for the inlet and outlet of the fluid were drilled, and tubes, with inner and outer diameters of 0.6 mm and 0.9 mm, respectively, were inserted into the holes. Glue was applied to fix the tubes in the orifices. Finally, pure water was injected via the tube into the entire cavity.

The integrated LEDs have a width, height and thickness of 2 mm, 1.2 mm and 0.4 mm, respectively. The voltage applied to the LEDs was 2.2 V. Both LEDs were welded to copper wires and connected to a power supply.

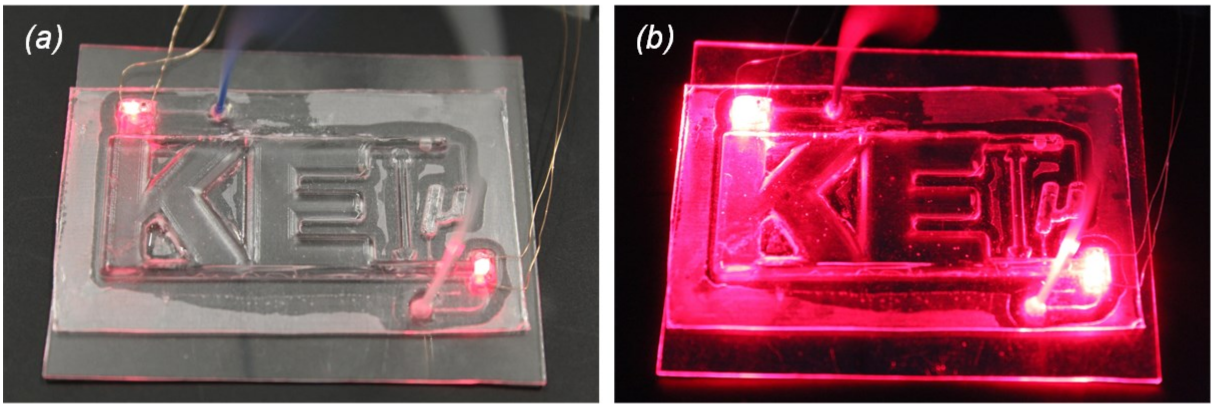

Figure 4.6: Sample with lighted LEDs with (a) and without (b) ambient light.

Lighted LEDs on a sample with and without ambient light are shown in Figure 4.6a and Figure 4.6b, respectively. The micro channels and cavities of the sample were filled with water. The LEDs lighted their surrounding area. The red-light paths can be clearly observed in the structure without ambient light. However, the light was unevenly distributed in the whole sample. To avoid this, the design would need to avoid sharp angles to guide the light around corners.

4.2 Fabrication of the flow rate sensor

Flow rate measurements can serve in microsystems for monitoring and controlling biological, medical, and chemical reagents. Thus, accurate flow rate sensors are vital for the precise manipulation of liquid flow. Among the various types of flow sensors to measure liquid flow rates, thermal flow sensors have been extensively used [58]. They utilize heat transfer to determine the flow velocity of the fluid, either liquid or gas flows. They have been developed in the past using both silicon and polymer materials.

Many thermal flow sensors are made from silicon wafers [58] because it is comparable with most microfabrication processes. However, silicon has high thermal conductivity, resulting in high heat transfer into its surroundings and thus reduced device sensitivity. Attempts to solve this problem make the fabrication process complex and expensive. Polymer materials, on the other hand, have also been used to fabricate thermal flow sensors [59]. They are inexpensive, robust, and have low thermal conductivity. In this chapter, a thermal flow rate sensor was fabricated by combining ultrasonic thermoforming and ultrasonic welding using an ultrasonic welding machine. The total cycle time is within tens of seconds.

4.2.1 Measuring principle of the flow rate sensor

A time of flight sensor is a kind of thermal flow sensors, which requires at least one heater and one downstream sensor to detect the transmission time of a heat pulse over a certain distance [60]. The research suggested that the heat conductivity and viscosity of the fluids influence the heat transition time between heater and fluid and/or fluid and sensor [61]. But with a sensor wire parallel to the flow channel, the characteristic curves of the time-of-flight thermal flow sensor are only a very weak function of fluid properties and temperature [62].

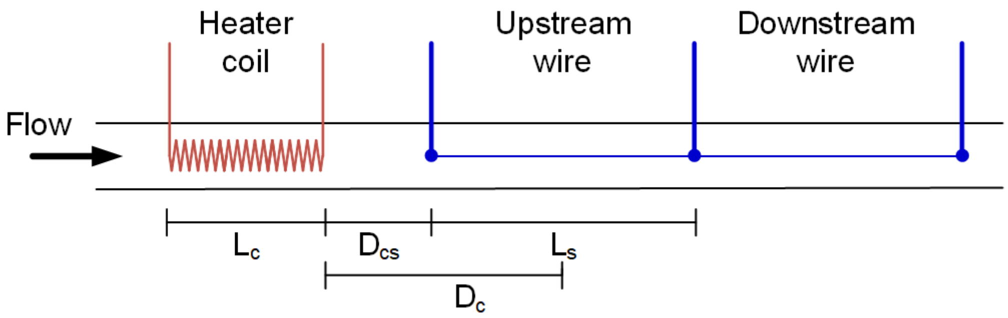

Figure 4.7: Schematic drawing of time-of-flight thermal flow rate sensor.

The schematic drawing of the time-of-flight thermal flow sensor is shown in Figure 4.7. A heat pulse is generated by a heater coil and transferred into a flowing fluid. The heated pulse of liquid flows along the measuring channel. When it is flowing through the upstream wire, the temperature of the wire is elevated, and the electrical resistance of the wire is getting larger.

The upstream and downstream wires are in one branch of a bridge circuit. The temperature rise of the upstream wire increases its resistance, hence breaking the balance of the bridge circuit and a potential difference arises between the two ends of the bridge branch. As the heated length of the upstream wire becomes larger, the measured voltage of the bridge is getting larger until the heated fluid pulse arrives at the downstream wire (heating period of upstream wire, Figure 4.8). When the downstream wire continues to get warm as the heated fluid pulse flows by, the electrical resistance of the downstream wire is also elevated. Thereafter, the bridge circuit gradually goes back to balance again and the voltage and current on the bridge branch are both zero (end of the heating period of the downstream wire, Figure 4.8). After that, the upstream wire is getting cooler while the downstream wire remains to be warmer. The electrical resistance of the former is slightly lower than that of the latter because of the earlier cooling of the upstream wire. Finally, both wires are cooled down to the temperature of the liquid flow past them.

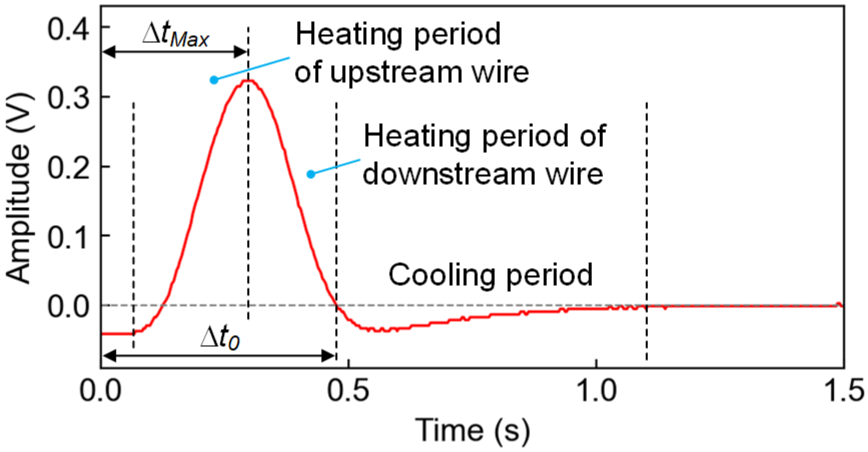

Figure 4.8: Detected signal from the bridge.

From the detected signal, a time is derived which is a correlated with the flow time of the heated fluid pulse between heater and sensor wires. After a calibration, the mean flow velocity is obtained proportional to the inverse of the derived time.

4.2.2 Design and fabrication of the flow rate sensor

Based on the previously elucidated measuring principle, the flow rate sensor was designed and fabricated. This flow rate sensor is composed of a top foil, a base foil, a heater coil, and two sensor wires, as shown in Figure 4.9. The top and base foils were ultrasonically thermoformed from PET-G foils with a thickness of 500 µm. A semicircular channel was thermoformed on each of them. A flow channel was fabricated by ultrasonic welding of the top and base foils. The heater coil and sensor wires were integrated into the flow channel by placing them in prescribed positions right before welding.

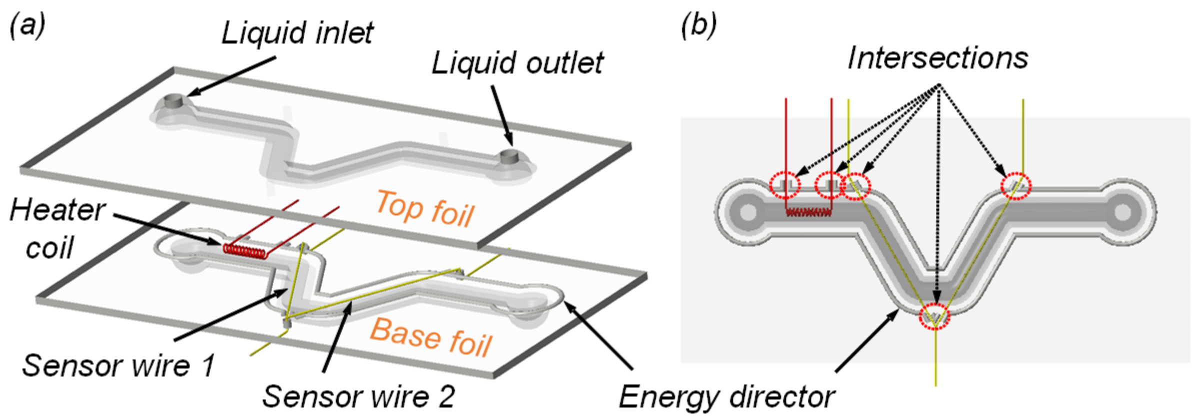

Figure 4.9: Explosive view (a) and top view (b) of the flow rate sensor.

The measuring channel, where the sensor wires are located, was designed in a V-shape (cf. Figure 4.10). This was preferred because with this design the sensor wires can be fixed in the middle of the channel parallel to the flow direction without any bracing. It is also easier to fix the sensor wire in the designed position compared to adopting a straight measuring channel. Both ends of the sensor wires at the joint interface were then welded into the weld joint to be fixed. A micro protrusion with a width of 250 µm and a height of 190 µm along the welding line (red in Figure 4.10) was acting as an energy director during ultrasonic welding of the top and base foils. This energy director not only concentrates ultrasonic energy but also positions the heater coil and sensor wires.

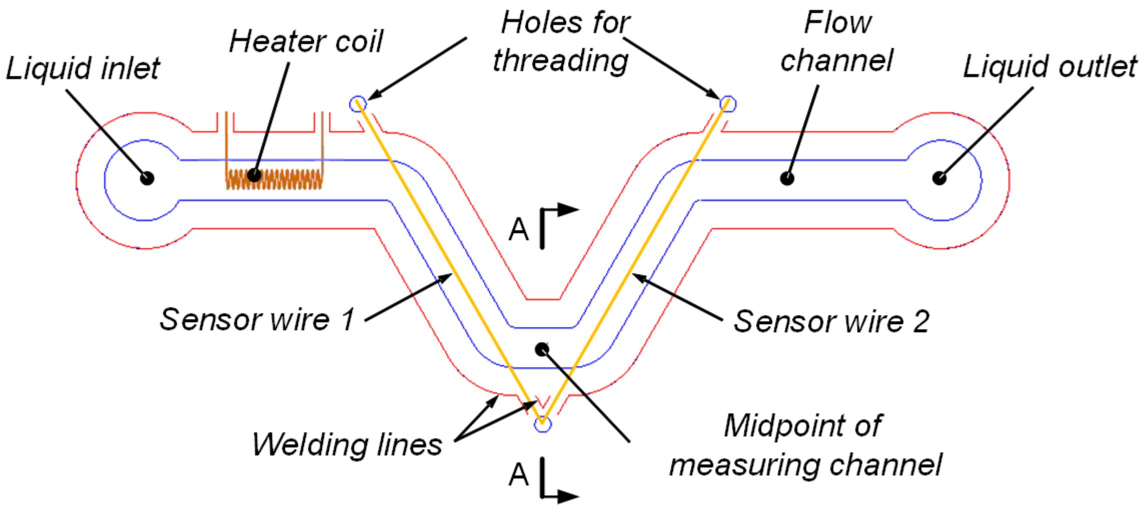

Figure 4.10: Schematic top view of the flow rate sensor.

The cross-section of the flow channel is circular with a diameter (D_f) of 1 mm and its area is calculated as 0.785 mm². The corner of the flow channel was rounded with a diameter of 1 mm to prevent breakage during ultrasonic thermoforming and demolding. The heater coil is 2.4 mm long and has an outer diameter of 0.5 mm. It was fabricated from a resistance wire RD100/0.1 with a diameter of 100 µm and resistance per unit length of 62.40 Ω/m. The distance (D_{cs}) between the heater coil and sensor wire 1 is 1.6 mm. Each sensor wire inside the flow channel is from gold with a diameter of 50 µm and a length (L_s) of 5.4 mm. Hence, the distance (D_c) between the end of the heater coil and the start of the sensor wire 1 is 4.3 mm. Three holes with a diameter of 300 µm were punched into the base foil as shown in Figure 4.9 and Figure 4.10, to position the sensor wires.

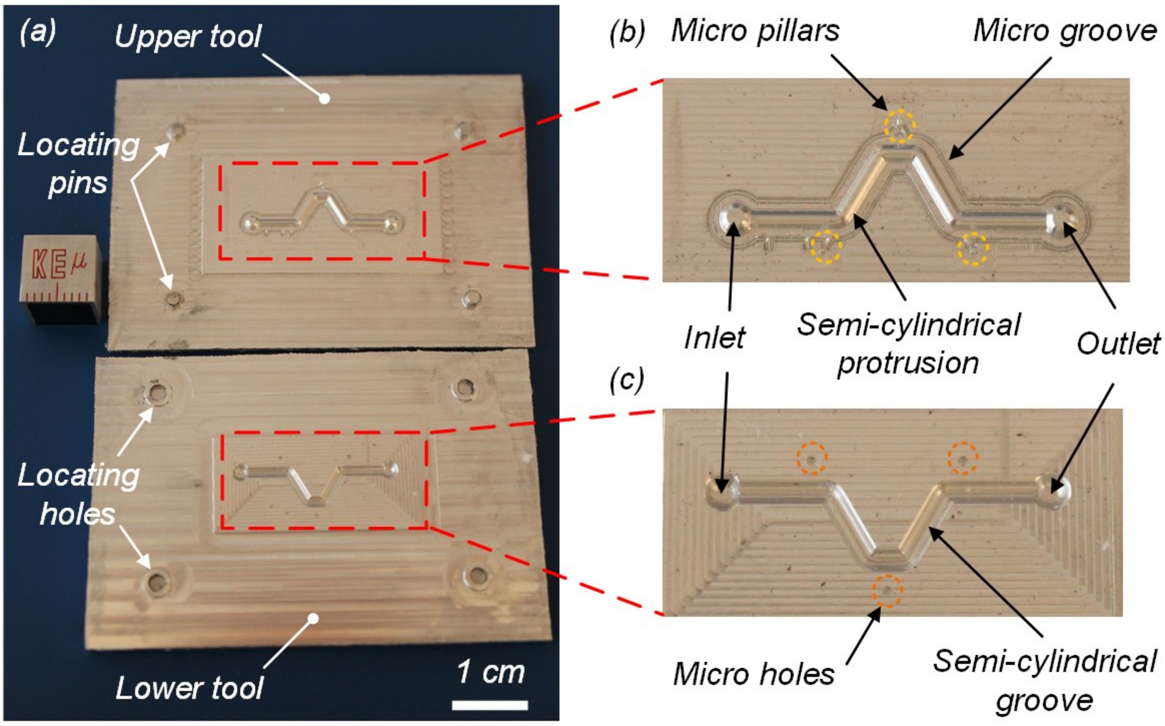

Figure 4.11: Tools (a) for ultrasonic thermoforming, and milled structures on upper tool (b) and lower tool (c).

The tools for ultrasonic thermoforming the base foil were milled from an aluminum plate as shown in Figure 4.11. A semi-cylindrical protrusion with a radius of 0.5 mm was milled into the upper tool (cf. Figure 4.11b) to thermoform the semi-circular channel. Its corresponding inverse structure was milled into the lower tool (cf. Figure 4.11c). The edge of this inverse structure was rounded with a radius of 250 µm, to prevent breakage of the thermoformed foil. To punch the three micro holes on the base foil (cf. Figure 4.10), three micro pillars with a diameter of 300 µm and a height of 490 µm and their inverse holes were milled into the upper tool and lower tool, respectively. The sensor wires were threaded into these punched holes before ultrasonic welding.

Micro grooves (cf. Figure 4.11b) surrounding the semi-cylindrical protrusion on the upper tool were designed to emboss the energy director for subsequent ultrasonic welding. It was engraved along the welding line (cf. Figure 4.10) using a ball end milling tool with a diameter of 250 µm and the engraving depth was 190 µm. As described in chapter 3.6, the tools got hotter during ultrasonic thermoforming when they had been fixed on the sonotrode. Therefore, it facilitates the ultrasonic hot embossing of the energy director when the upper tool is fixed on the sonotrode.

Four locating pins with a diameter of 2 mm and a height of 1.2 m were milled into the upper tool to align the two tools. Their corresponding locating holes with a diameter of 2.1 mm were also milled into the lower tool. The top of the hemispheric structures for the inlet and outlet on the upper tool were milled flat. Together with their inverse structure on the lower tool, hemispheres with flat tops were thermoformed facilitating the manual drilling of holes for tubes.

The top foil was the same as the base foil, but without energy directors and micro holes. So, another upper tool without micro grooves for energy directors and micro pillars for micro holes was milled also. Together with the lower tool in Figure 4.11a, the upper foil was ultrasonically thermoformed.

Table 4.1: Parameters for ultrasonic thermoforming the top and base foils and for ultrasonic welding.

Parameters	Top foil	Base foil	Ultrasonic welding
Pressing force	600 N	600 N	1000 N
Durations of vibration	1.4 s	0.7 s	0.18 s
Amplitude	20 µm	20 µm	20 µm
Trigger force	300 N	300 N	950 N
Cooling time	5 s	5 s	1 s
Holding force	800 N	800 N	800 N

PET-G foils with a thickness of 500 µm were used to thermoform the top and base foils for the flow rate sensor. The lower tool was fixed on the anvil. Then the upper tool was aligned with the lower tool and glued to the sonotrode. For each ultrasonic thermoforming, the lower tool was heated to 45°C to exclude the influence of a changing room temperature. Ultrasonic thermoforming parameters of the top and base foils are shown in Table 4.1. Pressing force, peak-to-peak amplitude, trigger force, cooling time, and holding force were kept constant at 600 N, 20 µm, 300 N, 5 s, and 800 N, respectively. The duration of ultrasonic vibration for thermoforming the top foil and base foil were 0.7 s and 1.4 s, respectively. Well thermoformed top and base foils are shown in Figure 4.12.

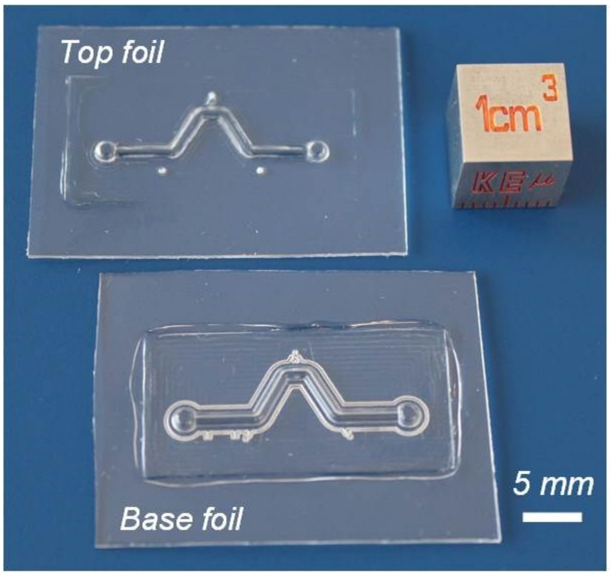

Figure 4.12: Thermoformed top foil and base foil.

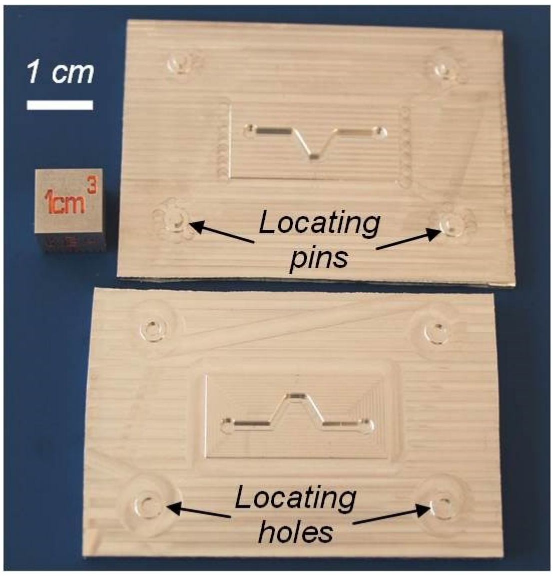

Figure 4.13: Tools for ultrasonic welding.

Due to the protruding semi-cylindrical channel on both top and base foils, the tools for ultrasonic welding were designed. The tools for ultrasonic welding are shown in Figure 4.13, a groove for placing the semi-cylindrical channel was milled on each tool. The upper and lower tools for ultrasonic welding were glued to the sonotrode and fixed on the anvil, respectively. Parameters for ultrasonic welding the top and base foils are shown in Table 4.1.

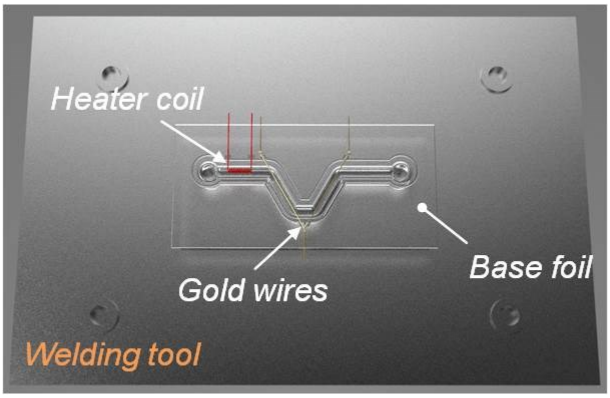

Figure 4.14: Placement of the components on the welding tool.

Before ultrasonic welding started, the heater coil and the sensor wire of the flow rate sensor are placed as shown in Figure 4.14. The gold wires were first threaded into the micro holes on the base foil (cf. Figure 4.9) and straightened with a small pull force avoiding breaking the 50 µm gold wires. They were fixed on the base foil using adhesive tape. Then, the base foil was placed on the lower tool. The heater coil was positioned with the help of the energy director and also fixed on the base foil using adhesive tape. All these adhesive tapes were carefully removed after ultrasonic welding.

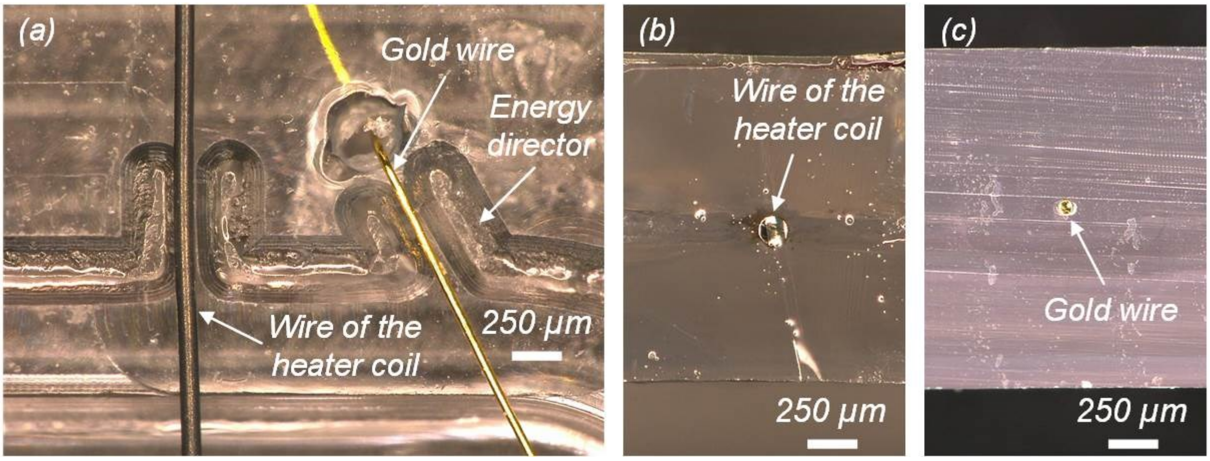

Figure 4.15: Top view (a) of specially shaped energy directors on the lower foil before ultrasonic welding, and cut through the wire of the heater coils (b) and a gold wire (c) after welding.

At the intersection of the energy director and the sensor wire, there was a gap and a 1 mm long energy director parallel to the wires located on both sides as shown in Figure 4.15a. The distance between these two energy directors was 200 µm. For thin filaments, e.g., 50 µm in diameter, the gold wire was placed between two energy directors. So that fissuring of the gold wire was avoided. Besides this, it also easily positions the heater coil and the sensor wire. The top foil was aligned and then mounted on the base foil. By ultrasonic vibration friction heat was generated and the energy director was molten. After solidification, the wires were tightly enclosed between the two foils and the gap was filled (cf. Figure 4.15 b, c).

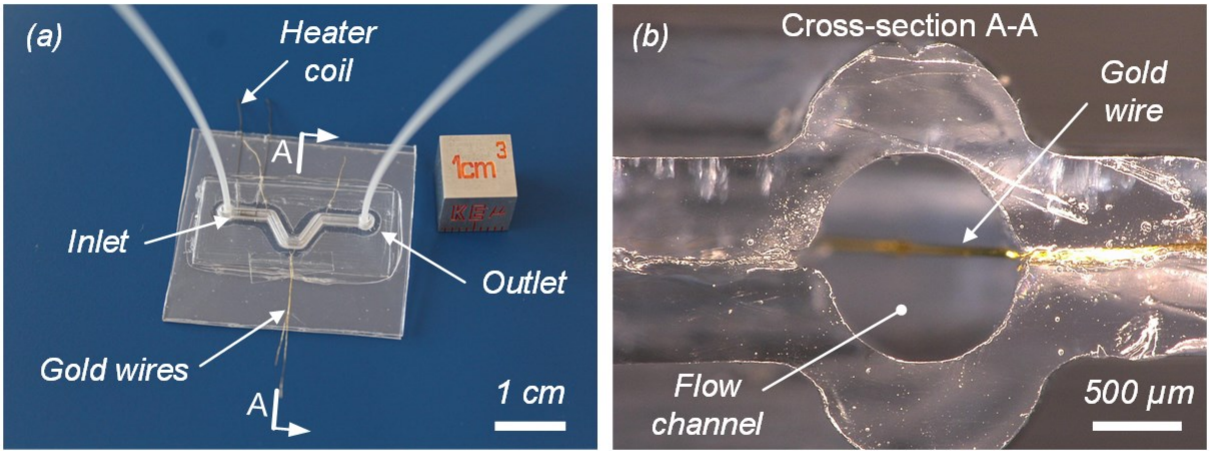

Figure 4.16: Fabricated flow rate sensor (a) and a cut through the flow channel (b).

Hemispheres with flat tops at the ends of the flow channel were designed for the inlet and outlet of the fluid. Holes with a diameter of 1 mm were drilled into them after ultrasonic welding. Two PTFE tubes with inner and outer diameters of 0.6 mm and

0.9 mm, respectively, were inserted into the holes. Glue was applied to fix the tubes in the orifices. Figure 4.16a shows a flow sensor after fabrication with connection tubes.

Figure 4.16b shows a cut through the flow channel on the flow rate sensor. The two foils were tightly welded, and no polymer melt was squeezed into the circular flow channel. For practical use, the flow rate sensor should be sealed and show no leakage. To check this, water was injected into the flow rate sensor through the inlet tube. No leakage was observed, indicating that the flow rate sensor was watertight. The actual cross-section area of the flow channel was measured to be 0.748 mm^2. It was determined by averaging the cross-section areas of three samples fabricated with identical parameters (cf. Table 4.1) measured by the digital microscope.

4.2.3 Measurements of the flow rate sensor

The fabricated flow rate sensor was tested with different liquids. An overview of the entire measurement setup is shown in Figure 4.17. The syringe pump generated a constant flow of liquid through the sensor and into a container.

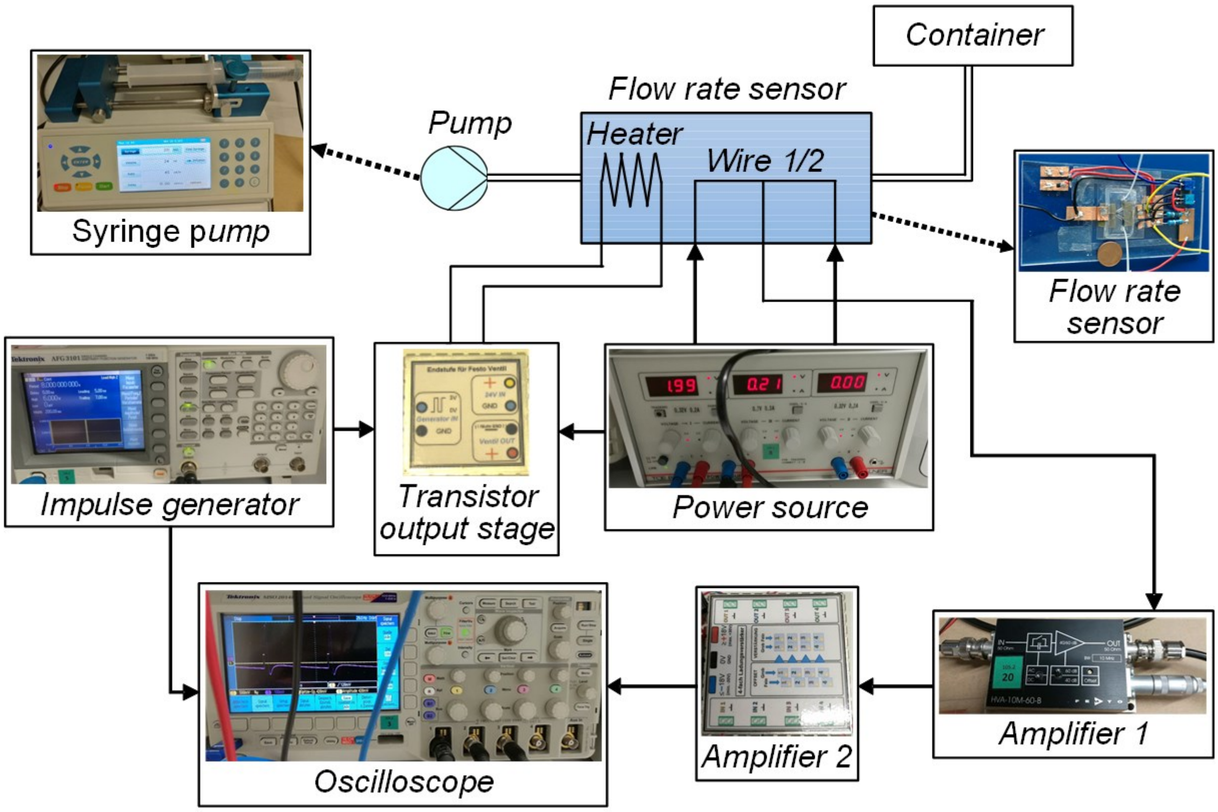

Figure 4.17: Measurement setup of the flow rate sensor.

The liquid in the flow channel was heated by the heater coil for a short time generating a heat pulse in the liquid. The heater coil was connected to a transistor output stage controlling the switch-on time of the power source. The input voltage from the impulse generator is the base-emitter voltage. When it was greater than 0.7 V, the base-collector junction is forward biased, hence the heater coil was powered. The duration (t_h), interval, and amplitude of the heat pulse were 200 ms, 8 s, and 6 V, respectively.

The applied voltage of the heater coil was generated by the power source, it is adjustable and readable. But the current cannot be directly read because the switch-on time was too short for the reaction of the power source, on which the display of the current has a time delay when the current changes. In order to determine the current, an electrical resistor with a resistance of 1 Ω was in series connection with the heater coil. Then, the applied voltage of the resistor was measured by an oscilloscope; the current flow through it was determined by the voltage divided by 1 Ω.

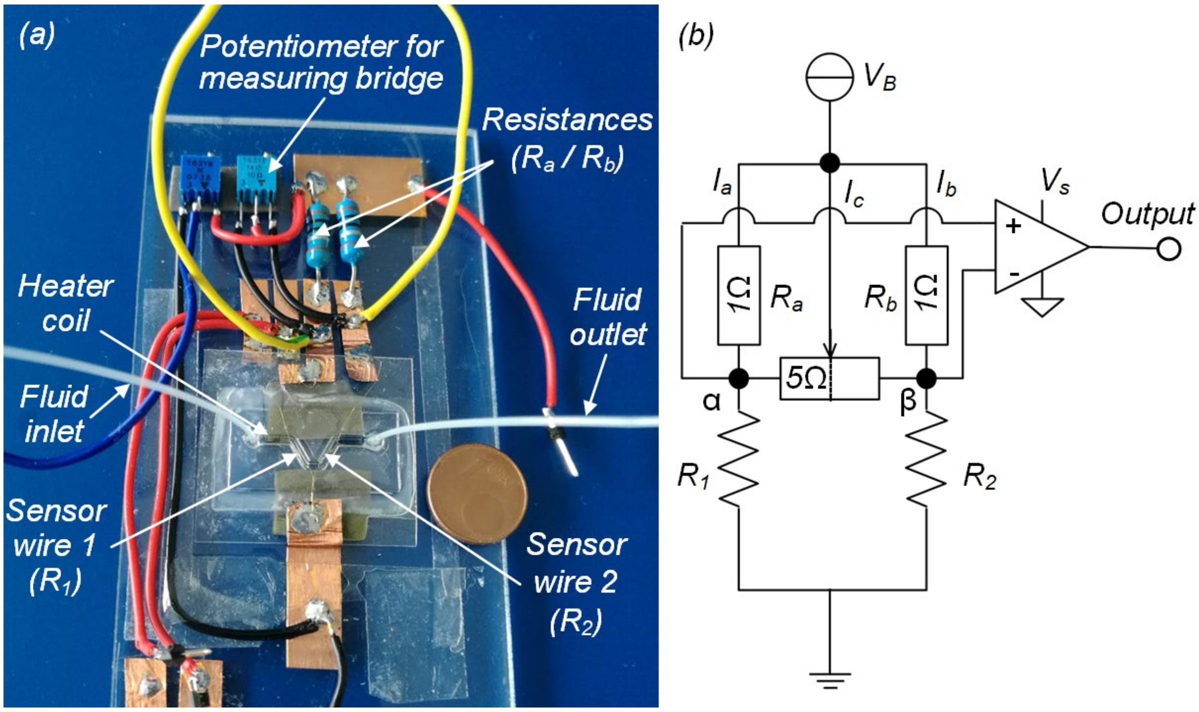

Figure 4.18: Electrically connected flow rate sensor (a) and schematic measuring circuit (b).

In the measurement, the flows of water, ethanol, and oil were injected in the flow rate range between 15 to 100 ml/h, the corresponding mean flow velocities are in the range from 5.81 mm/s to 37.1 mm/s. The sensor wires 1 and 2 were combined into a half bridge. The measuring bridge was connected to the points α and β as shown in Figure 4.18b. The measuring current was the total current of the bridge circuit. After leveling the electric potential of the sensor wire 1 and 2 by the potentiometer (cf. Figure 4.18a) when there was no flow through them, the current flowing through the sensor wires was about half of the measuring current and the output of the bridge circuit was 0 V. When the measuring current in sensor wires was greater than 400 mA, the output signal was unstable because the self-heating of the sensor wires disrupted the heating by the heated stream of liquid. But a measuring current less than 50 mA was too small to observe the output signal. Therefore, a measuring current of 250 mA was adopted. Investigations in the experiments showed that a current of 125 mA through each sensor wire causes no detectable change of the output signal.

When one of the sensor wires was heated up by the passing fluid, its electrical resistance increased and a voltage was measured at the output. The output signals of the flow rate sensor measured with water at different flow rates are shown in Figure 4.19. At the flow rates of 60 ml/h and 100 ml/h, the measured voltage of the bridge got a peak when the heated fluid pulse arrived at sensor wire 1 and then reached sensor wire 2. After that, the measured voltage of the bridge did not go back to zero but rised again, that is a second peak of the output signal. This indicates that the sensor wire 1 was heated again. It is not clear where this second heated fluid pulse came from. A possible explanation is that the fluid was split into two streams by the heater coil. Because its inner and outer diameters are 0.3 mm and 0.5 mm, respectively; and it was located at the center of the nearly circular flow channel of which the diameter was 1 mm. A much lower amplitude of the second peak means that the corresponding heated fluid was only a small portion of the flow. The flow rate before and after the heater coil were the same, hence the time of the heated fluid pulse flowed from the heater coil to the sensor wire 1 was not influenced. The second peak possibly can be eliminated if the heater coil is solid instead of a hollow one.

The time between the end of the heat pulse and maximum Δt_{Max} and zero crossing Δt_0 of the bridge output were recorded. It should be noted that Δt_{Max} is easier obtained and more reliable than Δt_0 because the base line of the signal, and therefore the crossing point of the signal with 0 V is not well defined (cf. Figure 4.8).

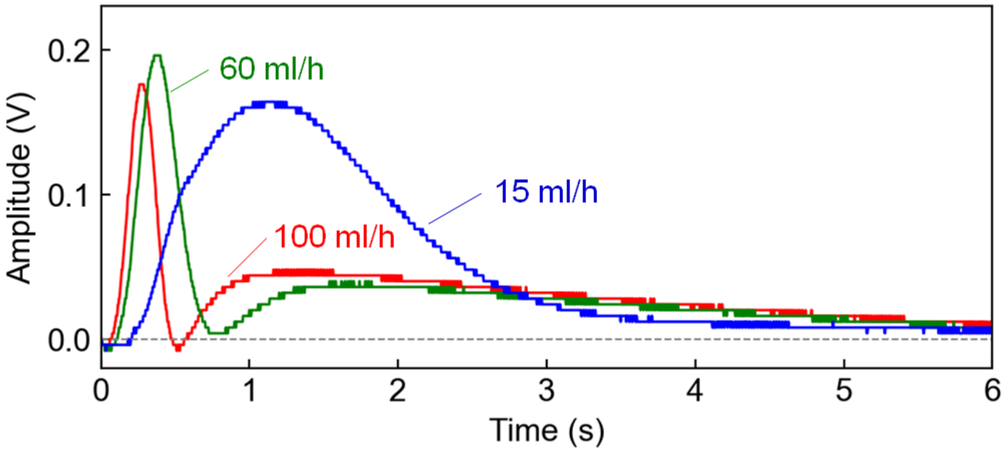

Figure 4.19: Output signal measured with water at different flow rates.

The signal is generated by the arrival of the heated fluid at the sensor wires. The heated fluid first heated up the sensor wire 1 resulting in a positive output voltage of the bridge, and then heated the sensor wire 2 generating a negative bridge output. At high flow velocities, less heat is transferred to the fluid and its temperature is less (cf. 100 ml/h in Fig. 4.19). If the flow velocity is high, heat is transfered to the the channel walls and distributed over the fluid in the direction of the length of the channel. Therefore, the generated peak is not so high and wider (15 ml/h in Fig. 4.19)

The measurement accuracy of the flow sensor is highly dependent on the accuracy of the function used to relate the time of flight and the average flow velocity. To help determine the appropriate correlation function for the fabricated flow sensor, the temperature distribution of the heated fluid along flow direction and its relationship with the detected signal was analyzed in the following.

As shown in Figure 4.20a, the red horizontal line represents the fluid (parallel to the flow direction) being heated in every moment within the heat pulse duration (t_h). So, the vertical height of those red lines is the cumulated heating time (t_{hf}) of the heated fluid. Assuming that the temperature of the heated fluid in a constant flow rate is a function of its cumulated heating time, then the temperature of the heated fluid (T_{hf}) along the flow direction is distributed as shown in the lower part of Figure 4.20a. The product of the flow velocity (v) and heat pulse duration, that is the flow distance within the heat pulse duration $v \cdot t_h$, is smaller than the length of the heater coil (L_c). The temperature maximum is located at the mid of the heated fluid, the length of it is s_0. Because of the symmetry of the temperature distribution of the heated fluid, $s_0 = L_c - v \cdot t_h$. The time of flow of the maximum Δt_{Max} and zero crossing Δt_0 (cf. Figure 4.19) of the bridge output are expected when the temperature maximum arrives at the mid of the sensor wire 1 and the mid-point of the measuring channel, respectively. The temperature maximum arrives at the mid of the sensor wire 1 when the fluid has traveled the distance $D_c + s_0/2$. In this case,

$$D_c + \frac{L_c - v \cdot t_h}{2} = v \cdot \Delta t_{Max} \qquad (4\text{-}1)$$

As illustrated in Figure 4.20b, when the flow distance within the heat pulse duration $v \cdot t_h$ is equal to the length of the heater coil L_c, the temperature maximum is located at the end of the heater coil when the heat pulse ends. The corresponding flow velocity and flow rates are 12 mm/s and 32.3 ml/h, respectively. The length of the temperature maximum s_0 is zero, resulting in:

$$D_c = v \cdot \Delta t_{Max} \qquad (4\text{-}2)$$

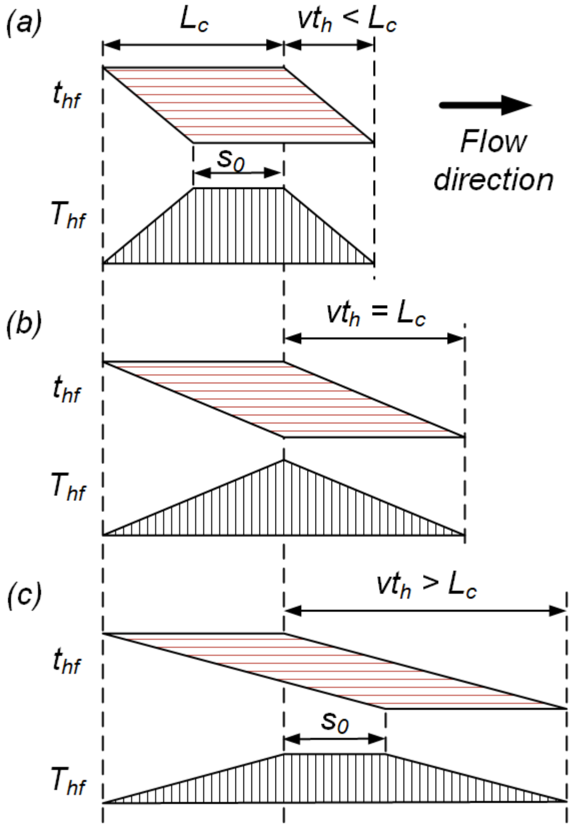

Figure 4.20: Temperature distribution of heated fluid along flow direction with different flow velocities.

When the flow velocity v is higher, the flow distance within the heat pulse duration $v \cdot t_h$ is greater than the length of the heater coil L_c, as shown in Figure 4.20c. The temperature maximum arrives at the mid of the sensor wire 1 when the fluid has traveled the distance $D_c - s_0/2$. The length of the temperature maximum s_0 is $v \cdot t_h - L_c$. This leads to:

$$D_c - \frac{v \cdot t_h - L_c}{2} = v \cdot \Delta t_{Max} \tag{4-3}$$

Thus, the flow velocity is derived from equations 4-1 and 4-3, giving:

$$v = \frac{2 \cdot D_c + L_c}{2\Delta t_{Max} + t_h} \tag{4-4}$$

When the flow distance within the heat pulse duration $v \cdot t_h$ is equal to the length of the heater coil L_c (cf. Figure 4.20b), equation 4-2 is also derived from equation 4-4. It means that equation 4-4 holds true for this case. Therefore, equation 4-4 was used to calculate the corresponding flow velocity of measured signals.

The Reynolds number [63] for liquids flow in the flow channel was calculated by:

$$\mathrm{Re} = \frac{\rho \cdot v \cdot D_{\mathrm{f}}}{\mu} \tag{4-5}$$

where ρ is the density of the liquid, v is the flow velocity of the fluid, D_f is the diameter of the flow channel, μ is the viscosity of the fluid.

In the measurement, the injected flow rate was in the range of 15 to 100 ml/h, the corresponding mean flow velocities were in the range of 5.81 mm/s to 37.1 mm/s. A check on the Reynolds number of three liquids were conducted by using equation 4-5 and the properties of liquids in Table 4.2. The calculated Reynolds number of water, ethanol, and oil are in the range of 5.81~37.1, 3.82~24.4, and 0.111~0.709, respectively. Since the Reynalds number of these three liquids are well below the critical value of 2,000, the flow is laminar [63].

The liquids were pumped into the flow sensor by a syringe and the length of the flow channel is short (less than 5 cm), it is assumed that the flow velocity of the fluid across the flow channel are all the same. The sensor wires of this flow rate sensor were fixed in the center of the flow channel; therefore they measure the flow velocity in the center. Therefore, the velocity near the sensor wire was used as the mean flow velocity in calculating volumetric flow rates of the flow rate sensor. It should be noted that the flow profile would be different if the liquid is driven in other ways, i.e., gravity force.

The mean flow velocity was calculated by equation 4-4, and its corresponding flow rate was then calculated by the following equation:

$$Q_f = v \cdot A_c \tag{4-6}$$

where A_c is the cross-sectional area of the flow channel.

Figure 4.21a-c shows the calculated flow rate plotted over the injected flow rate for water, ethanol, and oil, respectively. The blue dashed line represents the values where the calculated and the injected flow rate are equal. The error was defined as the difference between the calculated and injected value divided by the injected value. Each measurement was repeated three times, and their mean value and standard deviation are shown in the figures.

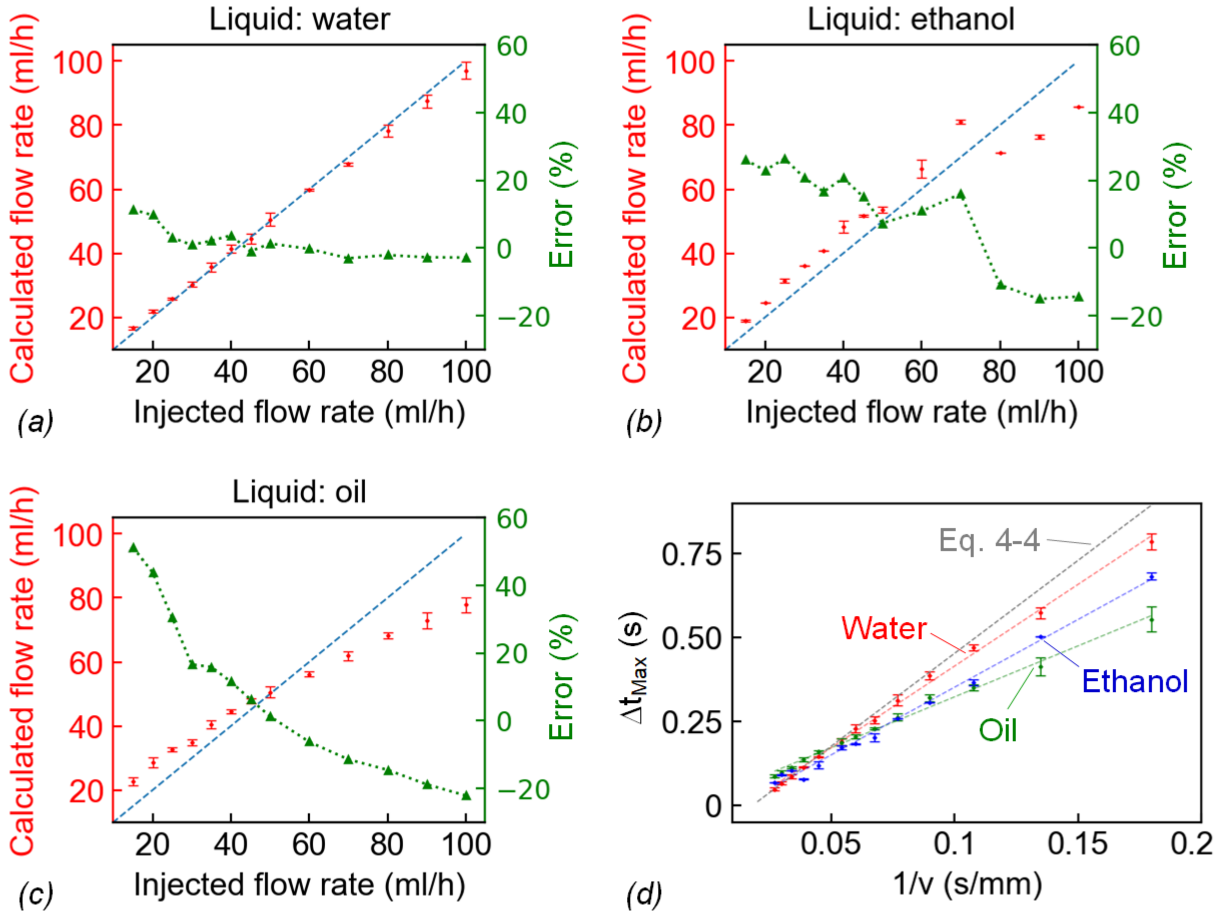

Figure 4.21: Comparison of injection flow rate and calculated flow rate of water (a), ethanol (b), and oil (c). Flow time Δt_{Max} as a function of the inverse of the injected mean flow velocity v (d).

The calculated flow rate is nearly the same as the injected flow rate for water (cf. Figure 4.21a). At the injected flow rate of 15 ml/h and 20 ml/h, the calculated value differs by about 10%. While at the injected flow rate between 25 ml/h and 100 ml/h, the average error is below 3%.

When ethanol was employed, the calculated flow rates show good linearity at flow rates of less than 80 ml/h and are larger than the injected flow rate. But at flow rates between 80 ml/h to 100 ml/h this is different. It is not clear why this happened. For oil, the calculated flow rate showed the largest differences to the measured ones but it has a good linearity.

A possible explanation of these observations is that due to different viscosities the flow profiles may be different. Besides, different heat conductivity and heat capacity of the three liquids may also influence the temperature profile in the flow and hence the temperature difference differs between the liquid and the sensor wires when measured at the same flow velocity. Consequently, the calculated flow rate is larger than the injected one.

The flow time Δt_{Max} of the three liquids as a function of the inverse of the injection flow velocity is shown in Figure 4.21d. A gray dashed line determined by equation 4.4 represents the ideal conditions where the mean velocity equals the velocity in the center of the flow channel. The measured flow time of the flow rate sensor remained a function of fluid properties.

During the measurement, the sensor wire is warmed by the heated fluid and the measuring current at the same time. The latter determines the amplitude of the signal. To find out the influence of heating by the measuring bridge current on the flow time Δt_{Max}, the flow time was measured as a function of the bridge current with ethanol. Each measurement was repeated three times, their mean value and standard deviation of measured values are shown in Figure 4.22. The Δt_{Max} of the four flow velocities 20 ml/h, 25 ml/h, 30 ml/h, and 35 ml/s are 0.516 ± 0.018 s, 0.405 ± 0.004 s, 0.332 ± 0.007s, and 0.271 ± 0.006 s, respectively. The results indicate that the variance of the measured flow time is larger at smaller flow rates, e.g. at 20 ml/h.

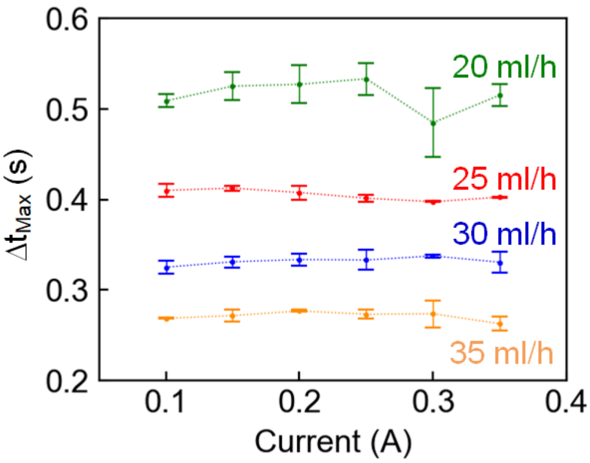

Figure 4.22: Influence of the measuring bridge current on the flow time Δt_{Max}.

Table 4.2: Fluid properties.

Properties	Water	Ethanol	Oil
Density [kg/m^3]	998	790	879
Viscosity [Pa·s]	1.0×10^{-3}	1.2×10^{-3}	46.0×10^{-3}
Heat conductivity [W/(m·K)]	0.598	0.165	0.126
Heat capacity [kJ/(kg·K)]	4.187	2.428	2.12

The sensitivity of a calorimetric thermal flow sensor varies with the thermal conductivity of the liquid [59]. Thus, the sensitivities of the flow rate sensor were tested with water, ethanol, and 'Tellus 46' hydraulic oil. Their properties are listed in Table 4.2. The amplitude of these three liquids measured at the flow rate of 100 ml/h is depicted in Figure 4.23. The signal peak maxima of water, ethanol, and oil are 0.128 V, 0.323 V, and 0.372 V, respectively. The amplitude of the detected signal of these liquids when varying the flow rate is summarized in Figure 4.24. There is a maximum of the amplitude as a function of the flow rate. The results show that the sensitivity of the proposed flow rate sensor varies according to the thermal properties of the liquid.

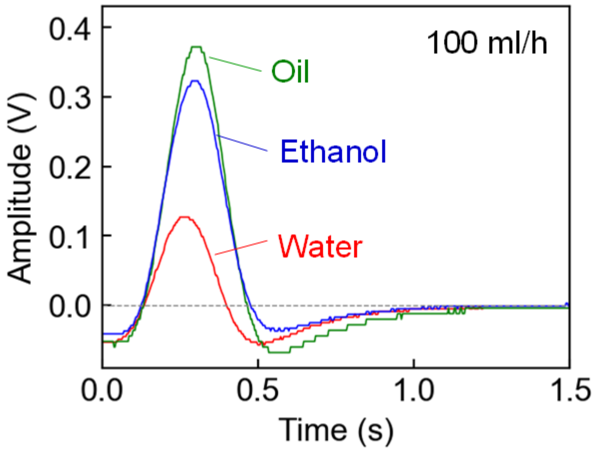

Figure 4.23: Amplitude of the detected signals of different liquids at a flow rate of 100 ml/h.

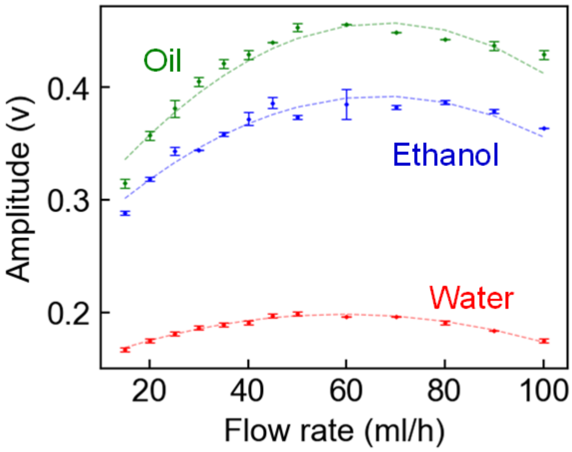

Figure 4.24: Detected voltage of three liquids at different flow rates.

Due to its higher heat capacity, the water was warmed up to a lower temperature than the other two liquids by the heater coil, and transferred its heat to the sensor wires slower. Besides this, the larger heat conductivity of water reduces its temperature by a radial flow to the circumference of the flow channel. The heat conduction from the heated fluid to its frontal in the axial direction leads to an earlier arrival of the heated fluid at the sensor wires.

4.2.4 Summary of the investigations on a flow sensor

By ultrasonic thermoforming, each foil with a semicircular channel was fabricated with a cycle time of less than 10 s. Together with subsequent ultrasonic welding; the top and base foils integrated with the heater coil and gold sensor wires were welded together in only 0.2 s. This way, a flow rate sensor with a nearly circular flow channel was obtained (Figure 4.16).

The measured flow time of water, ethanol, and oil indicated that the fabricated flow sensor remained a function of fluid properties. The correlation function Equation 4-4 is best suitable for water and ethanol and oil have their own characteristic curves. To get the characteristic curve of each liquid to be measured, it is necessary to calibrate the sensor before reliable measurements can be performed.

4.3 Variable focus lens

The conventional method to adjust the focal length of an optical system is to mechanically move the position of lenses along the optical axis. So the response times of the focus and zoom functions are limited by the mechanical motion of solid lenses with fixed focal length in the optical system. A variable focus lens, on the other hand, can dynamically adjust its focal length and therefore only fewer lenses are needed in the optical system [64-66]. Compared to a multitude of lenses with fixed focal length, which is bulky and complicated, a variable focus lens is a favorable alternative for optical systems. By changing the bending curvature of the refractive surface, the focal length of the liquid-filled variable focus lens is varied, allowing for a rapid response. Many types of variable focus liquid lenses have been reported [67], one of them is driven by electromagnetic actuators. This type of variable focus lenses are attractive because of their simple structure and zooming principle, and low cost.

Ultrasonic thermoforming, as a novel micro-fabrication technology, is especially suitable for fabricating the lens body. Combined with ultrasonic welding, an electromagnetic actuator was integrated into the lens body. With a low voltage (less than 5 V) and current (less than 2 A), the focal length was adjusted.

4.3.1 Design of the variable focus lens

The schematic of the liquid-filled variable focus lens with an aperture diameter of 3.5 mm and its exploded diagram is shown in Figure 4.25.

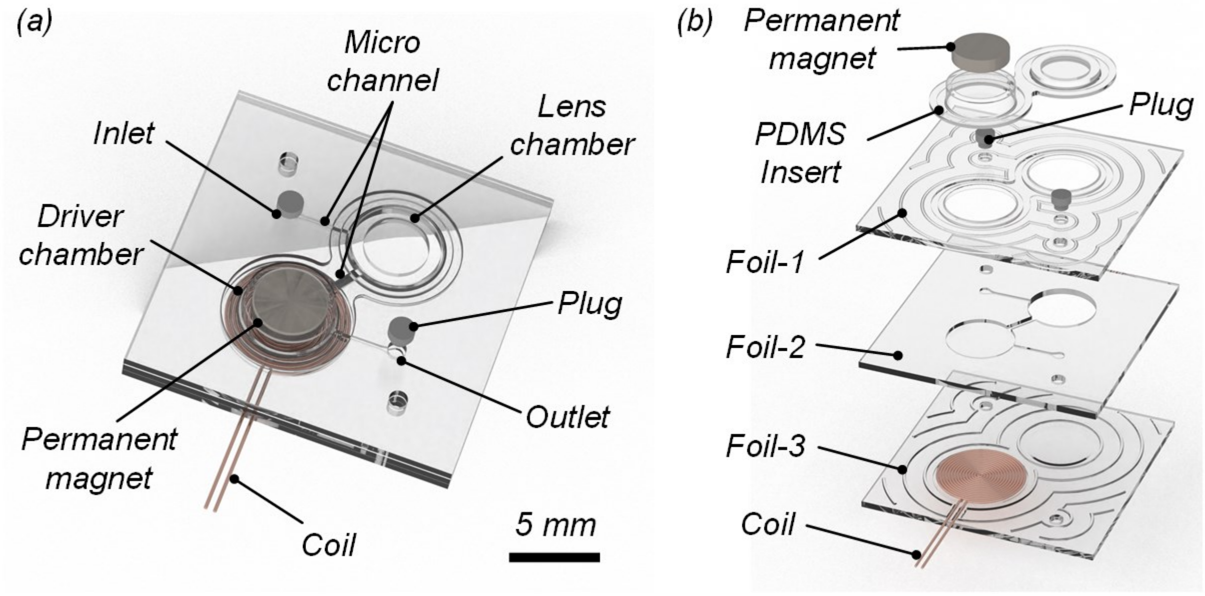

Figure 4.25: Variable focus lens (a) and its components (b). PDMS: polydimethylsiloxane.

The lens body contains two chambers: the lens chamber and the driver chamber, they are connected by a micro channel, 500 µm and 300 µm in width and depth, respectively. A planar coil with a permanent magnet was integrated into the driver chamber as a micro actuator to pump liquid in or out of the lens chamber. As shown in Figure 4.25b, this variable focus lens consists of foils 1-3, a coil, a permanent magnet, a PDMS insert, and two plugs. Each foil has two holes for aligning during ultrasonic welding. The foil-1 has two holes with a diameter of 5 mm for the PDMS insert and two holes for the inlet and outlet. The PDMS insert comprises two bottomless hollow cylinder structures: the shorter one is for the lens chamber and contains a 30 µm thick lens membrane, the taller one is for the driver chamber and a permanent magnet is fixed inside on its top. The foil-2 consists of a micro channel connecting two chambers and two micro channels connecting the inlet and outlet of the two chambers, respectively. The foil-3 has room for the coil and a convex spherical surface with a radius (R) of 10 mm for the optical path. Joining of the foils 1-3 is achieved by ultrasonic welding, and the PDMS insert is clamped between foil-1 and foil-2 to prevent leakage.

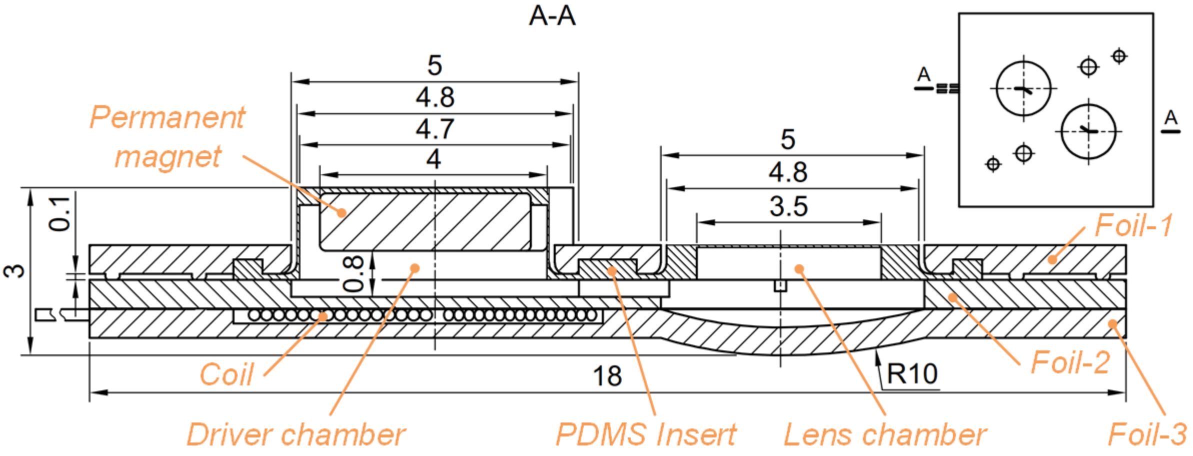

Figure 4.26: Cross-sectional view of the variable focus lens. Unit: mm.

The cross-sectional view (section A-A as shown in Figure 4.26) shows the detailed dimensions of the variable focus lens. Its length, width, and maximum thickness are 18 mm × 18 mm × 3 mm, respectively. The diameter of the driver chamber and aperture are 4.8 mm and 3.5 mm, respectively. The variable focus lens has a thickness of only 1.2 mm to minimize the gravity effect of the liquid.

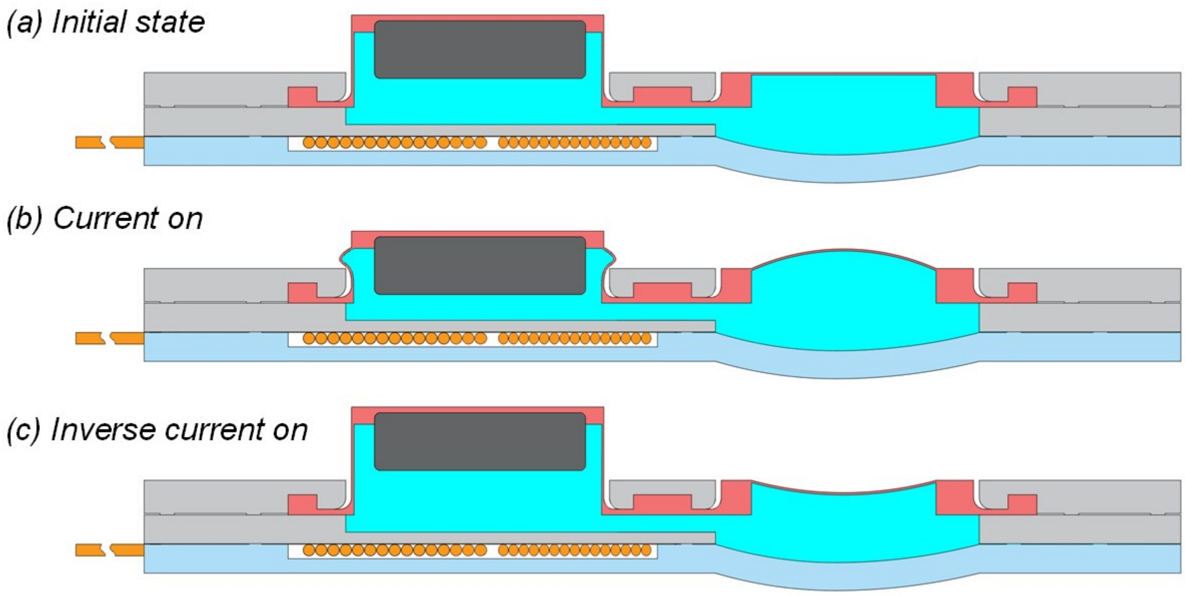

Figure 4.27: Operation mechanism of the proposed variable focus lens: (a) initial state; applied current to the coil (b); applied inverse current to the coil (c).

Figure 4.27 illustrates the working principle of the variable focus lens. In the initial state (cf. Figure 4.27a), the lens membrane on the PDMS insert is flat. When applying current to the coil (cf. Figure 4.27b), a magnetic force is generated between the coil and the permanent magnet, so they attract each other and the latter deforms the thin wall of the driver chamber on the PDMS insert. Hence, the micro actuator pumps the liquid into the lens chamber through the micro channel, changing the shape of the lens membrane and the focal length of the lens. With an increasing current, the magnetic force also gradually increases; the displacement of the permanent magnet increases shortening the focal length of the lens. With an inverse current applied (cf. Figure 4.27c), the water in the lens chamber is pumped out, so the lens membrane deforms towards the opposite direction resulting in a longer focal length.

4.3.2 Fabrication of the variable focus lens

The fabrication of the proposed variable focus lens includes ultrasonic fabrication of the foils for the lens body, electromagnetic actuator fabrication, and ultrasonic welding for assembly.

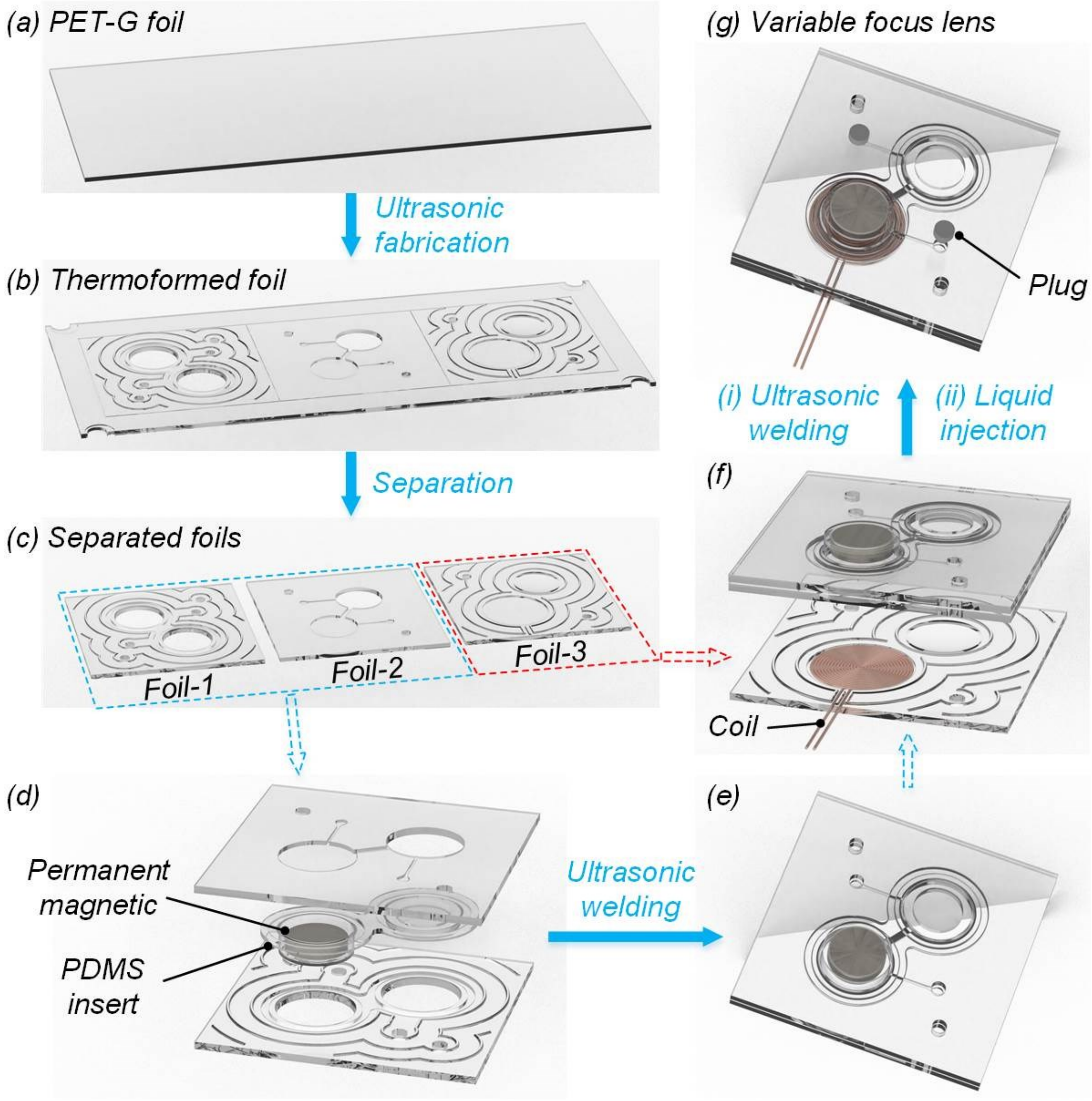

Figure 4.28: Fabrication procedures of the variable focus lens.

Figure 4.28 depicts the fabrication procedures of the lens. A PET-G foil was ultrasonically fabricated in a single step and then separated into foils 1-3 (cf. Figure 4.28 a-c). The PDMS insert together with a permanent magnet glued on the inner side of its driver chamber were placed on the predetermined holes on the foil-1(cf. Figure 4.28d). Foil-1 and foil-2 were first bonded by ultrasonic welding, so that the PDMS insert was clamped by the two foils preventing latent leakage. After that, the welded foils1-2 were ultrasonically welded with foil-3. The coil was placed on foil-3 before ultrasonic welding to obtain an electrical connection. The energy directors on foil-3 were melted and after solidification, the coil was tightly enclosed. Finally, pure water (refractive index, $n_w = 1.33$) was injected from the inlet to fill the two chambers and all micro channels. After that, the inlet and outlet were sealed by plugs from PET-G using glue.

4.3.2.1 Ultrasonic fabrication of the foils

The tools used for ultrasonic fabrication of the three foils were milled into aluminum plates as shown in Figure 4.29. Four locating pins and corresponding locating holes on two tools were designed to align all the structures of the tools. There are also convex/concave structures for thermoforming, columns and micro grooves for hot embossing, and holes and columns for punching. This way, the foils1-3 (cf. Figure 4.30) were ultrasonically fabricated in a single step by combining ultrasonic thermoforming, ultrasonic hot embossing, and ultrasonic punching. The upper tool was glued on the sonotrode and the lower tool was fixed on the anvil. With a heater on the anvil, the lower tool was preheated to 45 ºC. Pressing force, trigger force, peak-to-peak amplitude, welding time, cooling time, and holding force of ultrasonic fabrication were 600 N, 300 N, 20 µm, 2.4 s, 5 s, and 600 N, respectively.

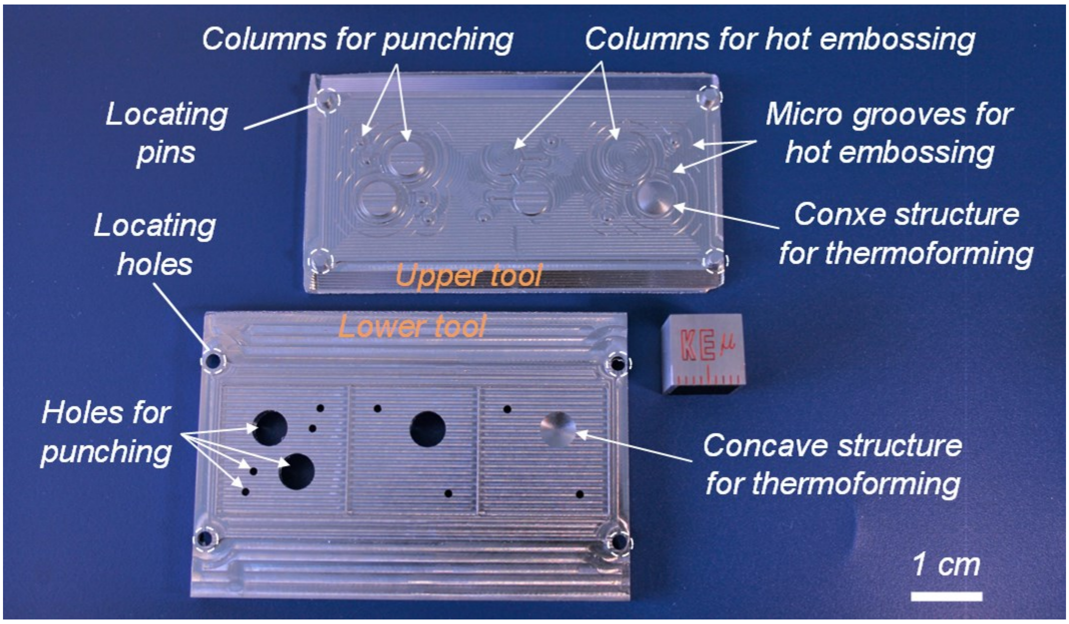

Figure 4.29: Aluminum tools used for ultrasonic fabrication.

Figure 4.30 shows the photo of the ultrasonically fabricated foil 1-3. Unnecessary materials were removed. As shown in the figure, the thermoformed lens surface, punched holes, hot embossed energy directors, cavity, and micro channel were all fabricated in a single step as designed. There are two locating holes on each foil for subsequent ultrasonic welding. This allows for aligning corresponding micro structure on three foils during welding. The energy directors served to bond and seal neighboring foils at the same time.

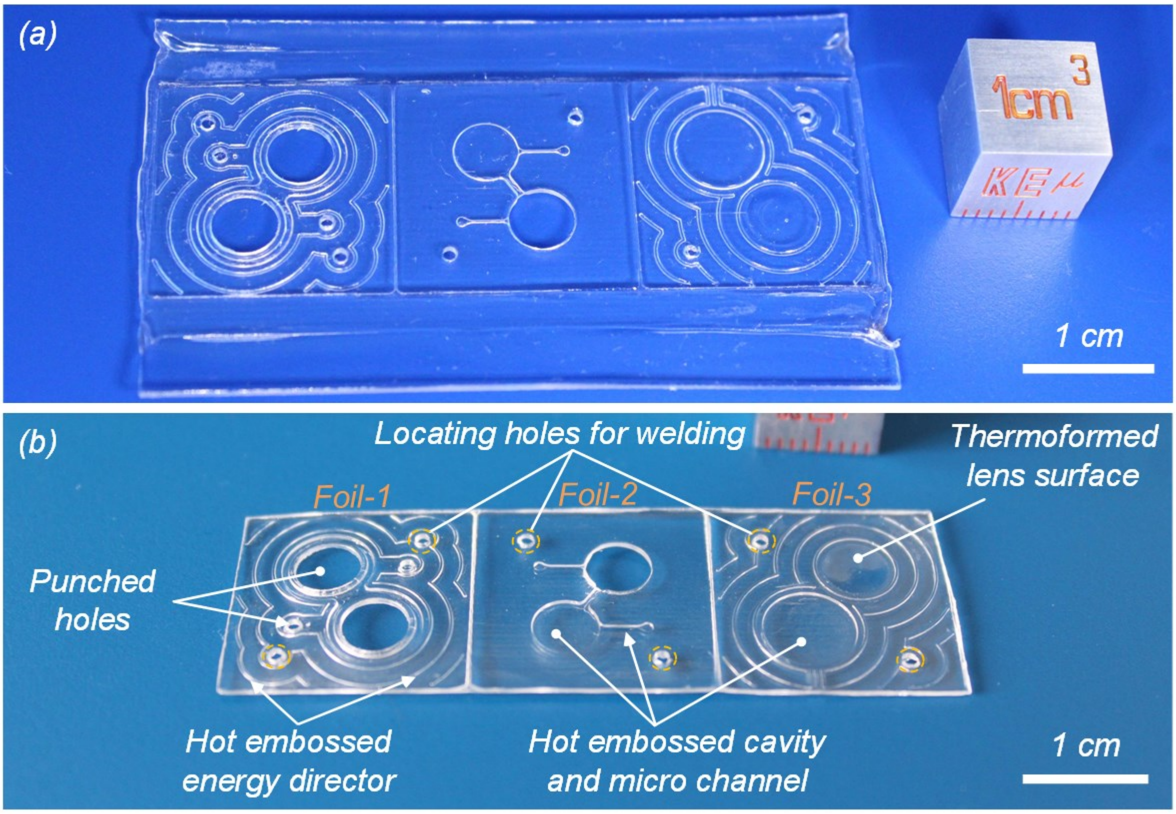

Figure 4.30: Ultrasonically fabricated foil1-3 before (a) and after (b) removing unnecessary material.

4.3.2.2 Fabrication of the micro actuator

The micro actuator consists of a commercially available NdFeB permanent magnet, a coil, and a PDMS insert, as shown in Figure 4.31. The diameter and height of the permanent magnet were 4 mm and 1 mm, respectively. The winding turns of the coil was 13, and a varnished copper wire with a diameter of 200 µm was used. The coil had an outer diameter of 7 mm and a thickness of 200 µm. The electromagnetic actuator consists of this planar coil and a permanent magnet was employed because, this way, large displacement and driving force are obtained by applying a voltage of less than 5 V.

The PDMS insert used in the variable focus lens was fabricated using poly-

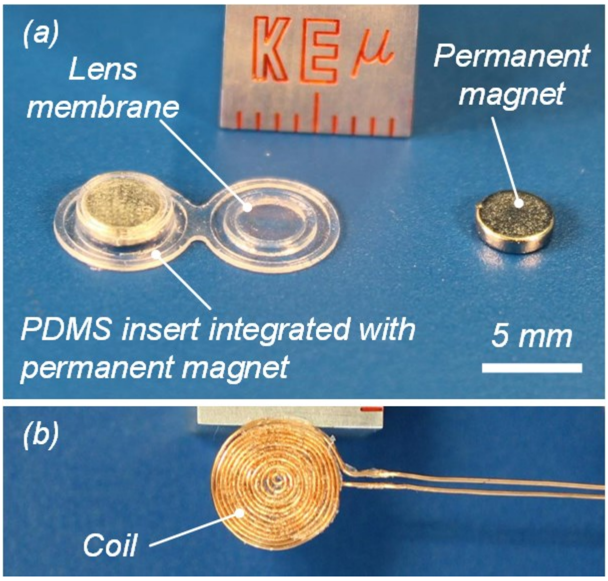

Figure 4.31: Photos of PDMS insert and permanent magnet (a), and coil (b).

dimethylsiloxane (PDMS, Sylgard 184, Dow Corning, Midland, MI, USA) with a mixing ratio of 10 (silicone resin): 1 (silicone elastomer). The detailed dimension of it is shown in Figure 4.32a. A pair of aluminum molds (cf. Figure 4.32b) was milled to mold the PDMS insert with a PDMS lens membrane, 30 µm in thickness. After milling, the surfaces for molding the lens membrane on the molds were carefully polished by polishing agent (Kratzer-EX, Enna Werk-Dr. Appelt GmbH & Co. KG, Germany). A non-woven fabric was used to polish the molds.

To take photos of the cross-section, the molds were cut through the middle of structure by milling. Six photos were taken at different positions and then stitched together. Hence, a single photo of the cross-section of the molds was obtained, as shown in Figure 4.32b.

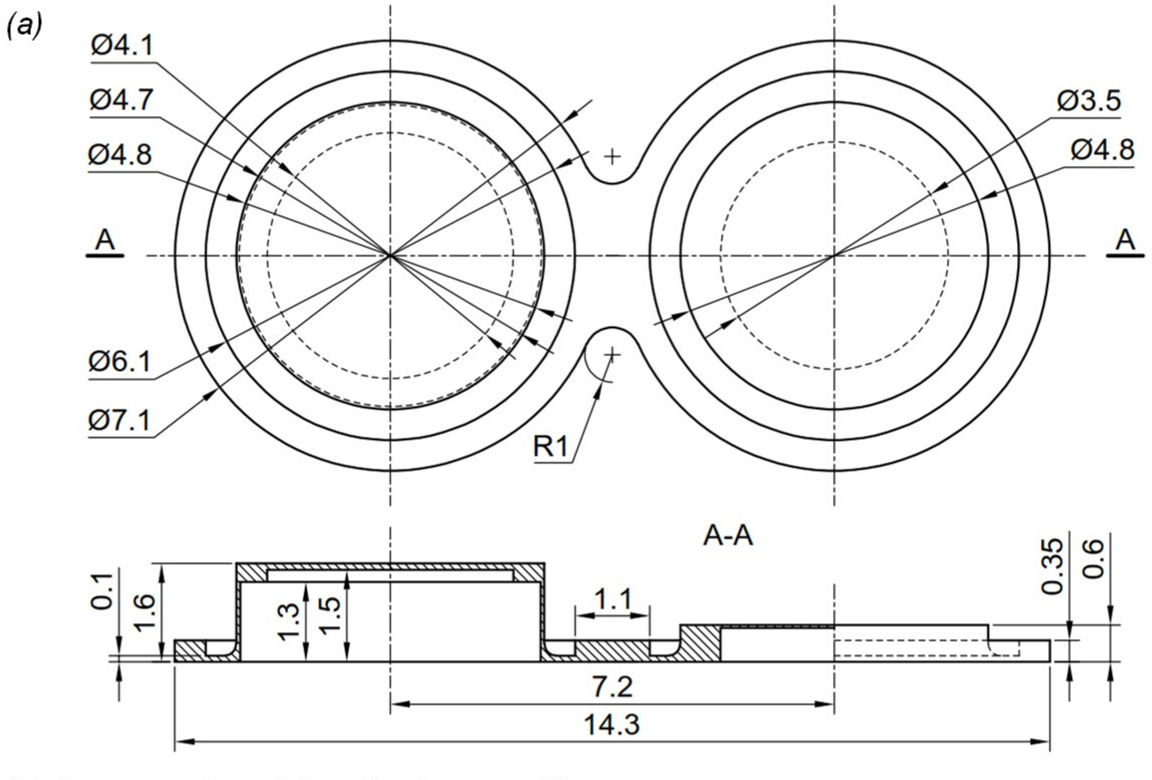

(b) Cross-section of the aluminum molds

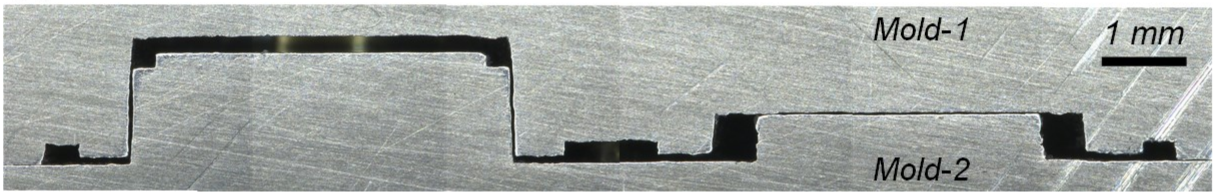

Figure 4.32: Detailed dimension of the molds for the PDMS insert (a) and photos of their cross-section (b).

The fabrication of the PDMS insert begins with cleaning the molds using acetone and pure water. After drying, the PDMS prepolymer was poured into the cavities on mold-1 and placed under vacuum to remove bubbles. Then, the mold-2 was mounted on the mold-1 and clamped with a proper force to squeeze out excess PDMS prepolymer.

Subsequently, it was cured at a temperature of 70 °C for 20 minutes. Finally, the molds were separated and the PDMS insert with a 30 µm-thick lens membrane was obtained (cf. Figure 4.31a).

The PDMS insert were cut through the middle along the A-A line (cf. Figure 4.32a) using a knife to observe its cross-section. Figure 4.33 shows the cross-section of the PDMS insert. The thickness of the driver chamber wall and the lens membrane were about 50 µm and 30 µm, respectively. This allows for a displacement of the driver chamber when applying a force of about 10 mN, thereby changing the shape of the lens membrane.

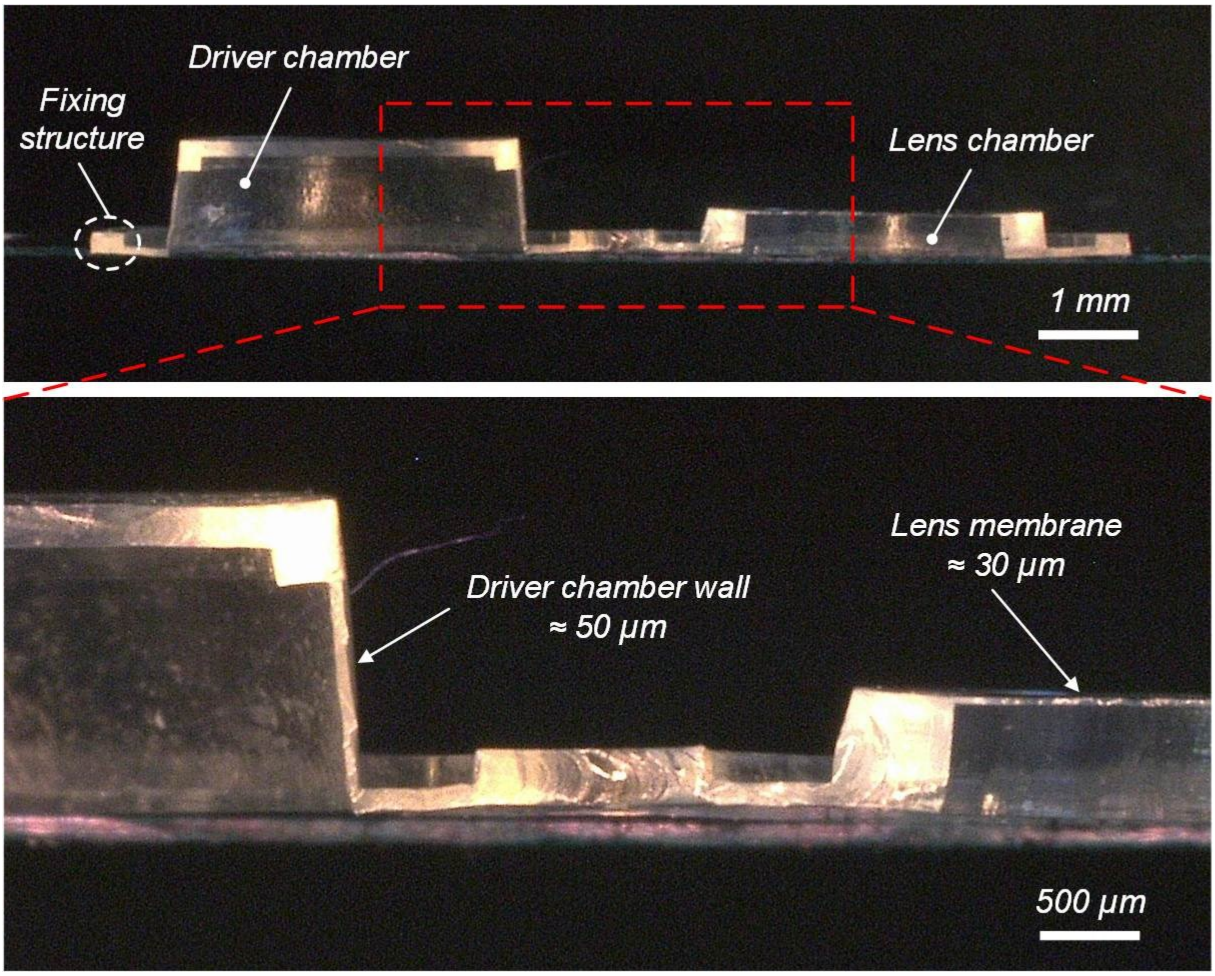

Figure 4.33: Cut through the PDMS insert.

4.3.2.3 Ultrasonic welding

The body of the proposed variable focus lens is composed of three ultrasonically thermoformed foils. They were bonded by ultrasonic welding integrating the micro actuator. Both the foils and the micro actuator have protruding structures on different sides and therefore they cannot be welded by the sonotrode directly. Otherwise, the thermoformed lens surface and the driver chamber of the PDMS insert would be destroyed. A welding tool was needed to bond all components without damaging them.

A pair of welding tools was designed and milled, as shown in Figure 4.34. The upper tool was glued on the sonotrode and the lower tool was fixed on the anvil. There are four locating holes and pins for the welding tools, ensuring the alignment of the upper and lower tool. Additionally, two locating holes and pins were especially designed for aligning the foils. Before the ultrasonic welding process, the foils were placed on the lower welding tool and fixed by the corresponding locating pins. The foils can only move along the locating pins, that is, the direction of the ultrasonic vibrations. This makes it possible to align the micro structures on the foils and bond them together. Both ultrasonic weldings shared the same parameters. Pressing force, trigger force, peak-to-peak amplitude, welding time, cooling time, and holding force of ultrasonic welding were 1000 N, 950 N, 20 µm, 0.15 s, 0.2 s, and 600 N, respectively.

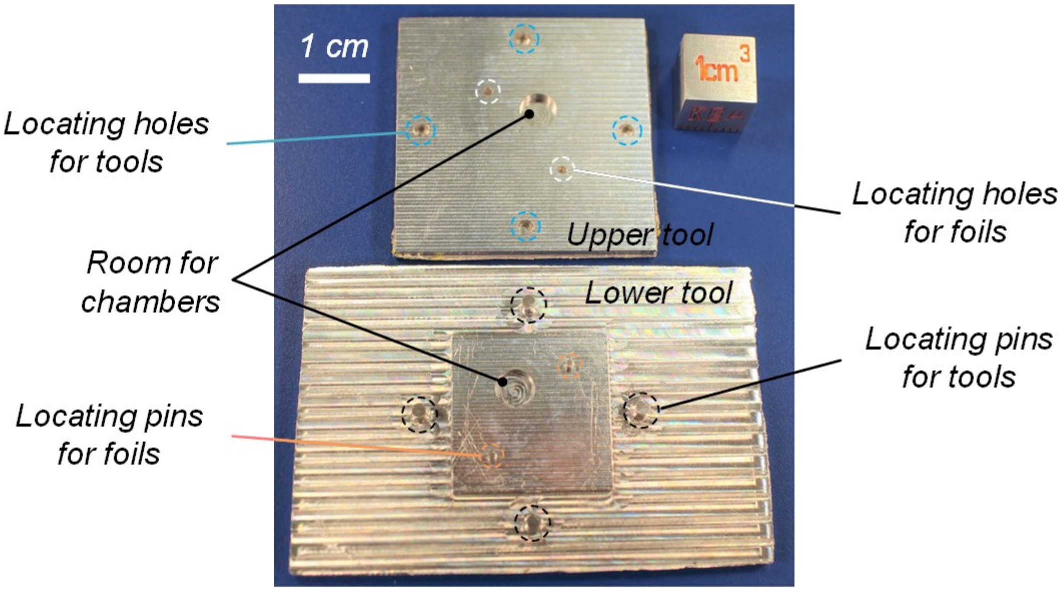

Figure 4.34: Tools for welding the variable focus lens.

Figure 4.35 b-d shows the photos of the cross-sectional views of the welded foils without integrating the micro actuator, of which the locations are depicted in Figure 4.35a. Figure 4.35b shows a cut through the center of the driver chamber, below is its magnificated photo. The three foils were tightly bonded after ultrasonic welding. There is a gap of about 0.1 mm when the PDMS insert is simply sandwiched between the foil-1 and the foil-2 as shown in Figure 4.26. Hence, the foil-1 and foil-2 would clamp the fixing structure (cf. Figure 4.33 and Figure 4.35b) if the PDMS insert had been integrated. With this design, the PDMS insert was firmly fixed and sealed. Besides, there is room for the coil separated from the liquid by the foil-2. Figure 4.35c shows the micro channel connecting the two chambers. Its cross-section was rectangular with a width and height of about 500 µm and 300 µm, respectively. As shown in Figure 4.35d, the micro channel connecting the inlet and the lens chamber had a square cross-section with a width of 200 µm.

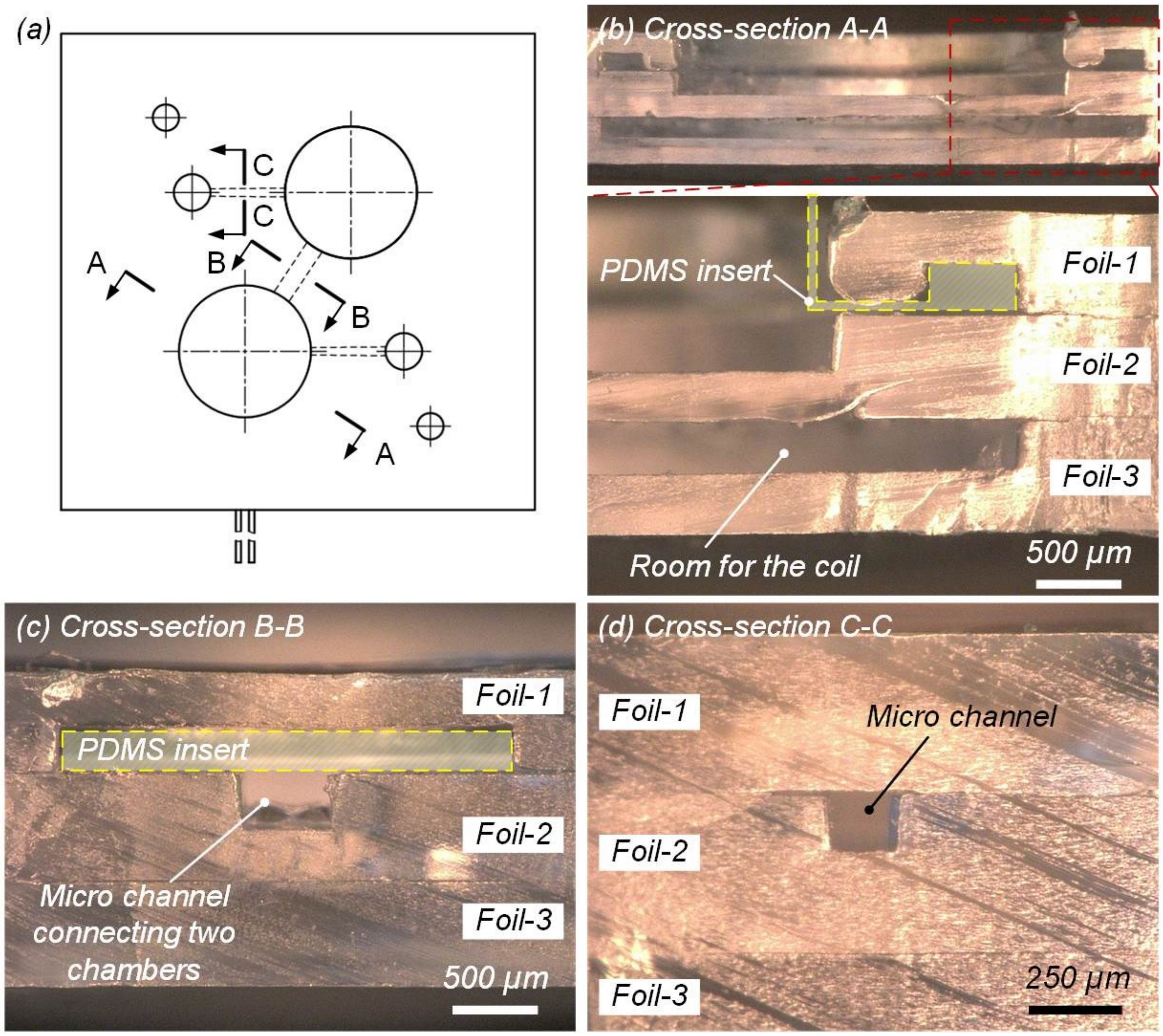

Figure 4.35: Top view of the variable focus lens (a) and cuts through the driver chamber (b), micro channel connecting two chambers (c), and connecting inlet and lens chamber (d) on the welded foils without micro actuator.

4.3.3 Fabricated variable focus lens

The fabricated variable focus lens is shown in Figure 4.36. No leakage was observed after applying a voltage on the coil. To determine the change of focal length of the variable focus lens, the angle between the deflected lens membrane and lens body were measured. The series of images captured from the lens chamber when the current applied varies between 0 and 1.4 A. Figure 4.37a shows the initial state of the lens membrane when there is no

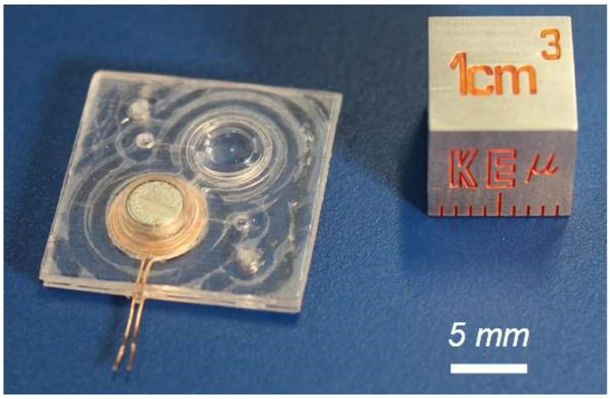

Figure 4.36: Photo of the fabricated variable focus lens.

current in the coil. The shape of the lens membrane is not plane but with an angle (θ) of about 4 ° because of the gravity force of the permanent magnet. When the current is applied on the coil, the electromagnetic force acted on the magnet drags the circular membrane of the driver chamber and pumps the liquid into the lens chamber. Hence, the lens membrane of the lens chamber was deflected as shown in Figure 4.37b-h.

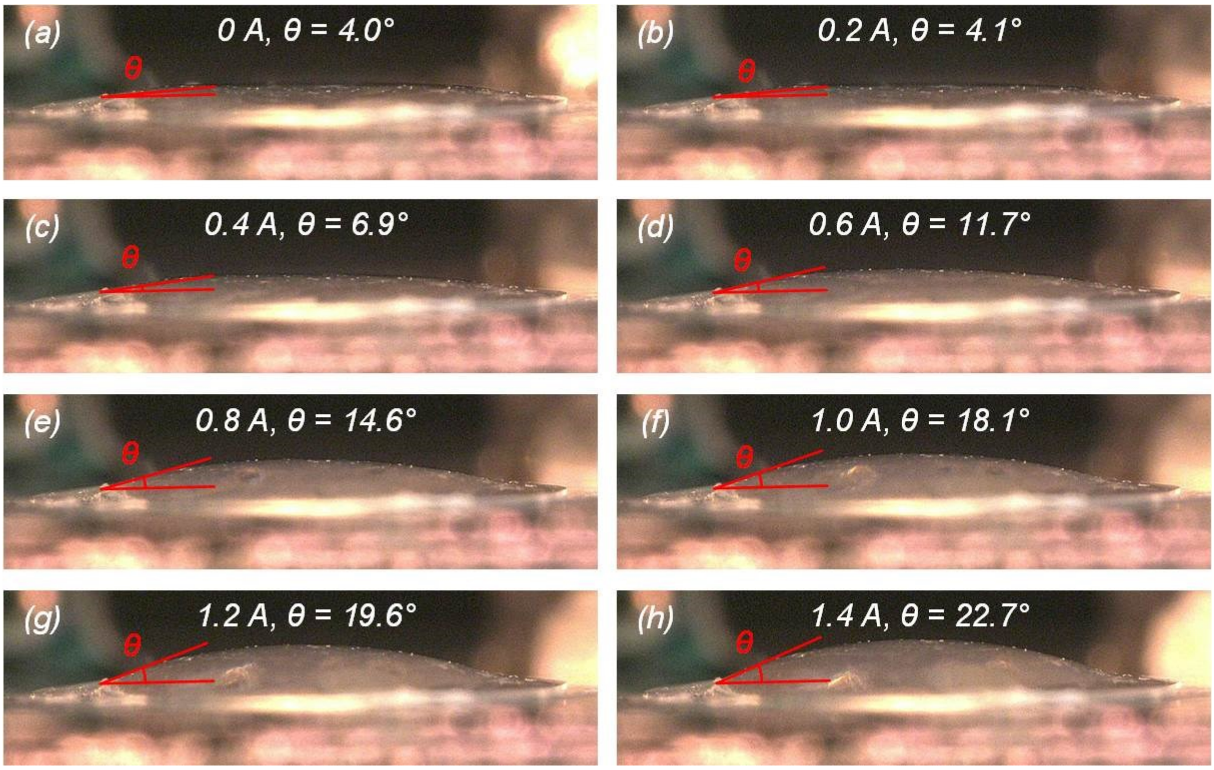

Figure 4.37: Photos of the shape change of the lens membrane with different applied current.

Figure 4.38 depicts the measured profile using the circular fit of the lens membrane at different current. From the measured angles using circular fit, the radii of curvature of the lens membrane were calculated using the following equation:

$$r = \frac{d_L}{2 \cdot sin(\theta)} \tag{4-7}$$

where r is the radius of curvature, d_L is the aperture of the lens, θ is the angle between the tangent of the lens membrane and the diameter of the lens at the point of their intersection as shown in Figure 4.37.

The deflection h at the center of the lens membrane can be calculated by the following equation:

$$h = (1 - cos(\theta)) \cdot r \tag{4-8}$$

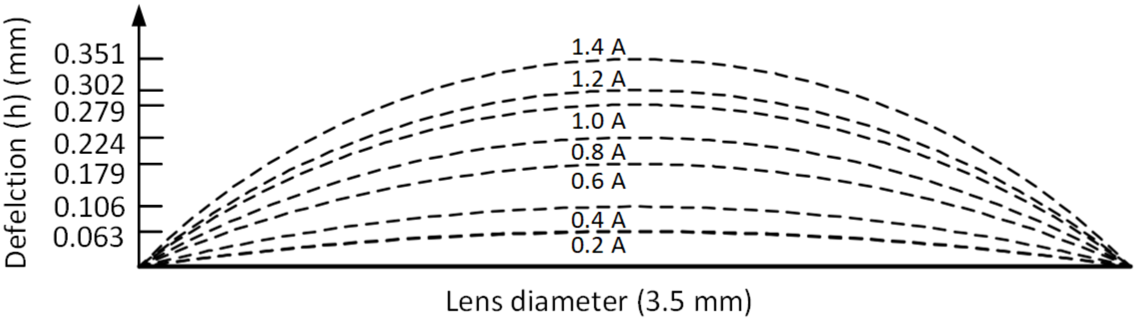

Figure 4.38: Measured profile of the lens membrane at different currents.

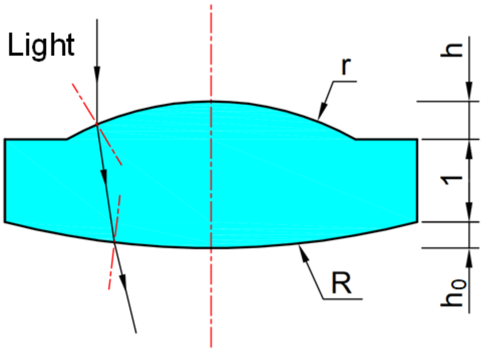

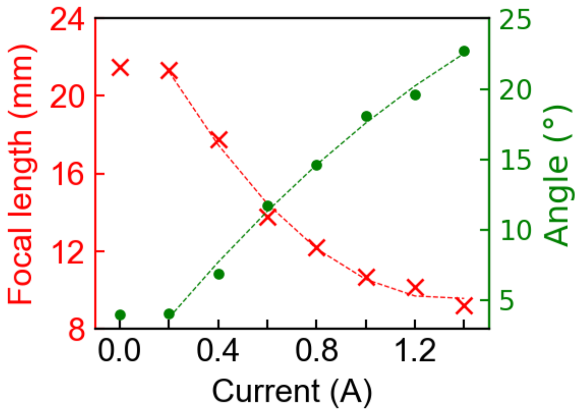

Figure 4.39: Path of the light refracted by the lens.

Figure 4.40: Calculated focal length and angle at different current.

One example of the path of the light refracted by the lens is shown Figure 4.39. The focal length (f) of the lens formed with radius of curvature r was calculated using the following equation [68]:

$$\frac{1}{f} = (n_w - n_a) \cdot (\frac{1}{r} + \frac{1}{R}) + \frac{(h + h_0 + d_c) \cdot (n_w - n_a)^2}{n_w \cdot r \cdot R} \tag{4-9}$$

where n_a is the refractive index of air, n_w is the refractive index of water inside the lens, d_c is the thickness (1 mm) of the lens chamber without deflection of the lens membrane, and h is the deflection of the lens membrane at the center as shown in Figure 4.38. The calculated focal length values from equation 4-9 are shown in Figure 4.40. The tuning range of focal length achieved using this variable focus lens is 9 mm to 22 mm. It is expected that its focal length would be longer with an inverse current. Figure 4.41 shows the photo of the light concentrated by the lens compare to the light dot without the lens.

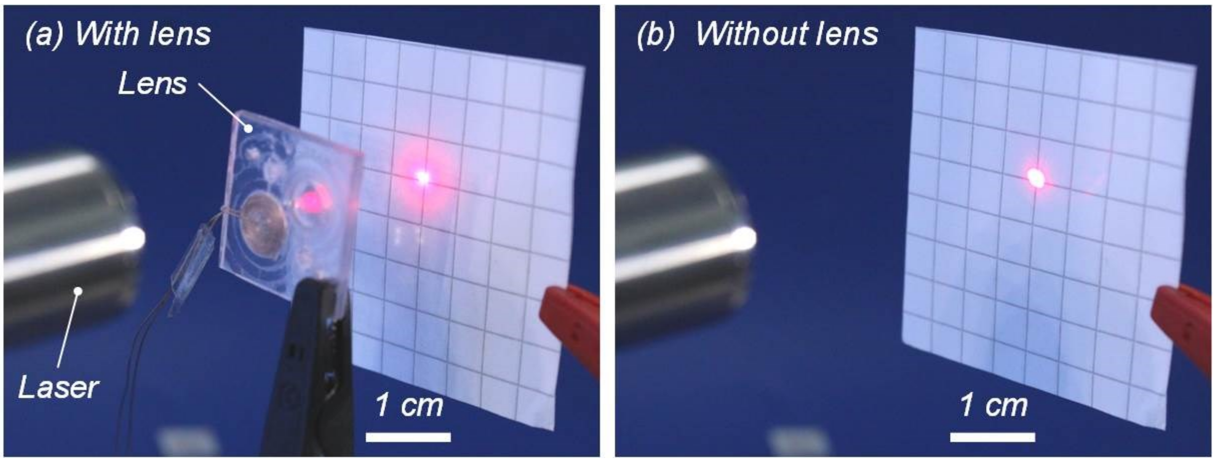

Figure 4.41: Photos of the light concentrated by the lens (a) and without lens (b). One grid represents five millimeters.

5 Chip with micro channel and cavity

In different microsystems, especially microfluidics, there are micro channels and cavities with different dimensions. It is important to obtain both at the same time. Ultrasonic thermoforming enables the thermoforming of complex three-dimensional structures directly from user-defined designs. Microfluidics is fabricated by enclosing thermoformed micro channels and cavities. Ultrasonic welding is a good option to achieve this. However, with high frequency ultrasonic vibrations, the flow behavior of the melted polymer from the energy director is hard to control [69] and the temperature distribution is inhomogeneous [40]. Hence, these may lead to the blockage of micro channels or failure to seal the micro structures. It’s an affordable and practical approach in the fabrication of microfluidics with enclosed micro channels and cavities if they were properly sealed.

A chip with sealed micro channels and cavities was fabricated by ultrasonic fabrication. The desired micro structures were ultrasonically thermoformed and bonded with another foil by ultrasonic welding.

5.1 Design of the micro channel and tools

During the ultrasonic welding process, micro channels are easily damaged due to the inhomogeneous temperature distribution and the difficulty to control the melted energy directors. To address this limitation, a micro channel with a special cross-section was designed as shown in Figure 5.1. As shown in Figure 5.1a, the width and height of the micro channel in the center are w_c and h_c, respectively. There are two parallel semicircular energy directors along the micro channel, their radii and distance to the micro channel are 125 µm and 500 µm, respectively. The ultrasonic vibrations generate friction heat to melt the energy director during ultrasonic welding. The melted energy director acted as a kind of glue joining the two parts to be welded and sealing both sides of the micro channel. On both sides of the micro channel, there are two rectangular protruding walls, of which the width and height are 250 µm and 60 µm, respectively. After ultrasonic welding (cf. Figure 5.1b), both rectangular protruding structures are clamped to the flat foil. This structure helps generating an enclosed rectangular micro channel and prevents excess polymer melt from entering the micro channel. Thus, preventing leakage or blockage of the micro channel.

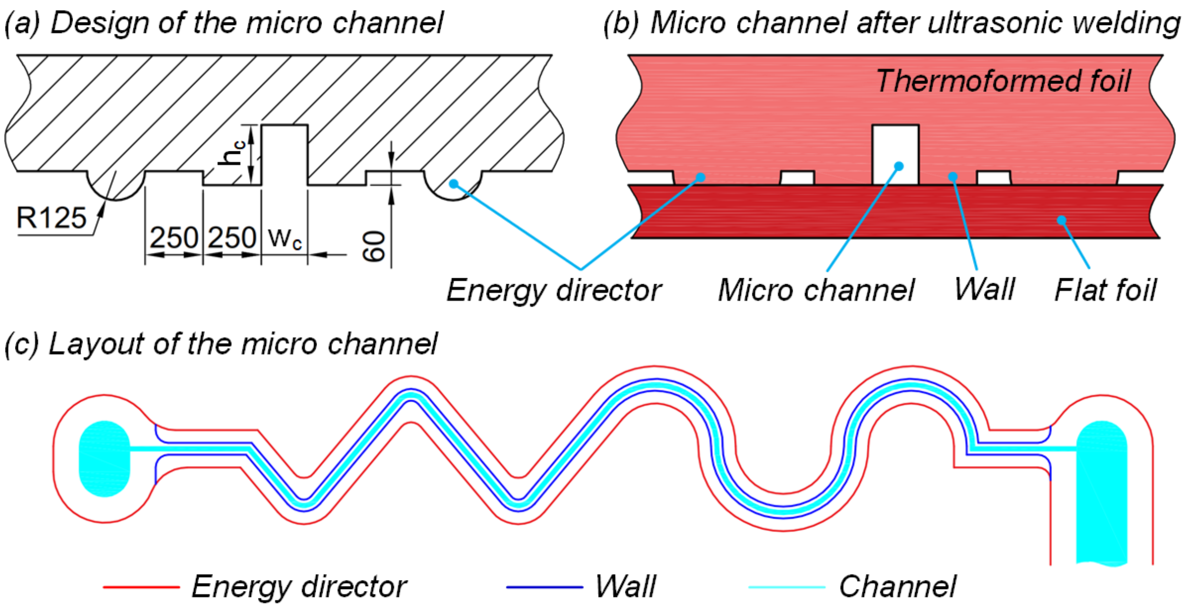

Figure 5.1: Design of the micro channel (a) and its cross-section after ultrasonic welding (b), layout of the micro channel (c). Unit: µm.

Figure 5.1c shows the layout of the micro channel and cavity. Each micro channel consists of two different shapes: zig-zag and serpentine. Both ends of the micro channel are connected to cavities. At these ends, the walls are intersected with their neighboring energy director preventing the liquid from entering the area between them.

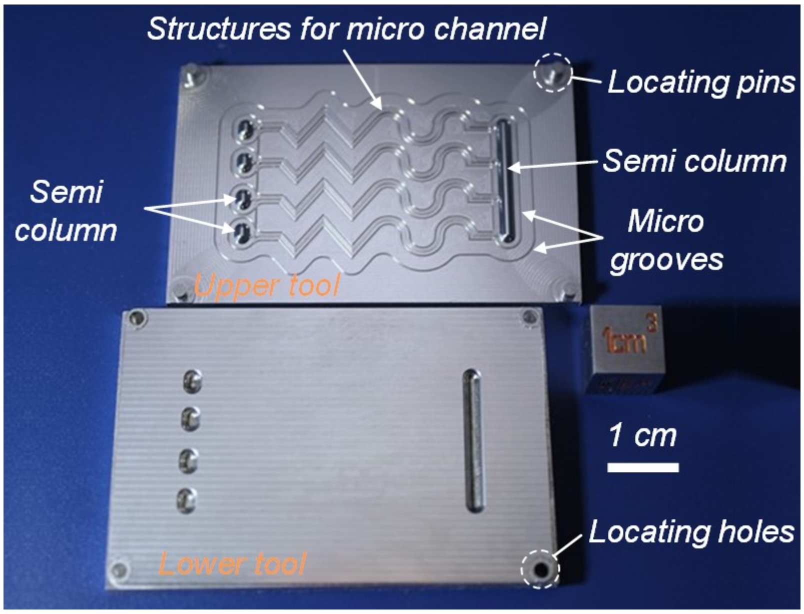

Figure 5.2: Tools for ultrasonic thermoforming.

The tools used for ultrasonic thermoforming the foil with micro channels and cavities were milled into aluminum plates as shown in Figure 5.2. Four locating pins and corresponding locating holes on two tools were designed to align all the structures of the tools. The cross-section of the structures for thermoforming the micro channels on the upper tool is the inverse of the cross-section of the micro channel, as shown in Figure 5.1a. Four micro channels with different dimensions (cf. Table 5.1) were designed. Their widths were 200 µm, 100 µm, 60 µm, and 30 µm, respectively. They are referred to as MC-200, MC-100, MC-60, and MC-30, respectively. Four short semi-cylindrical protruding structures were designed to thermoform cavities acted as inlets of micro channels. A longer one was designed to thermoform a semicircular channel that connects four micro channels. The diameter of these five semi-cylindrical protruding structures is 2 mm, and the edges of their corresponding concave structures on the lower tool were rounded with a radius of 0.5 mm to prevent breakage during ultrasonic thermoforming.

Table 5.1: Dimensions of designed micro channels.

Micro channel	MC-200	MC-100	MC-60	MC-30
Width (µm)	200	100	60	30
Height (µm)	240	240	140	90

5.2 Ultrasonic thermoforming of foil

The upper tool was glued on the sonotrode and the lower tool was fixed on the anvil. A PET-G foil, 500 µm in thickness, was used to thermoform a foil with micro channels and cavities. With a heater on the anvil, the lower tool was preheated to 45 ºC. Pressing force, trigger force, peak-to-peak amplitude, welding time, cooling time, and holding force of ultrasonic thermoforming were 600 N, 300 N, 25 µm, 5.4 s, 10 s, and 2100 N, respectively. It was found that a larger holding force facilitates the formation of embossed structures, such as the energy director.

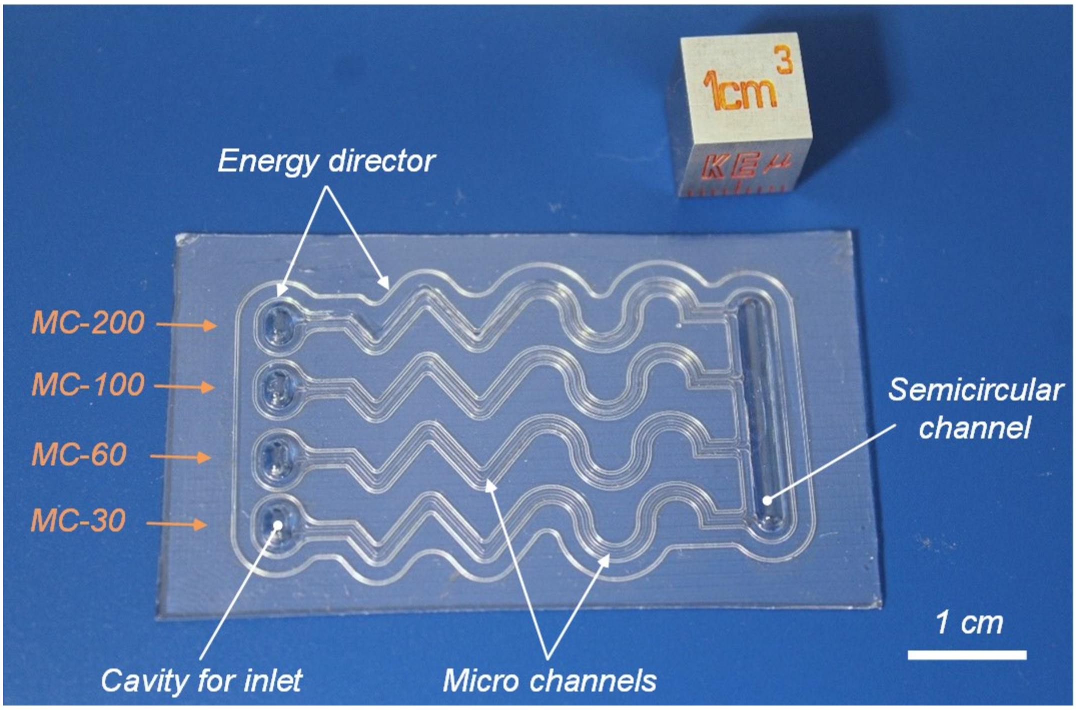

Figure 5.3: Ultrasonically thermoformed foil with micro channels and cavities.

Figure 5.3 shows the photo of the ultrasonically thermoformed foil with a dimension of 3.5 × 6 cm. As shown in the figure, the foil was well thermoformed without breakage or damage. Energy directors surrounding the four cavities, micro channels, and semicircular channels are intact. The outer energy director served to strengthen the bonding of the two foils to be welded.

Figure 5.4 shows the cross-sections of micro channels MC-200, MC-100, MC-60, and MC-30 on the ultrasonically thermoformed foil. As shown in the figures, the micro channels with different dimensions, walls, and energy directors were all well replicated from the tools. The structures on the tools maintained integrity with no signs of defects of deformation or breakage after at least 50 cycles.

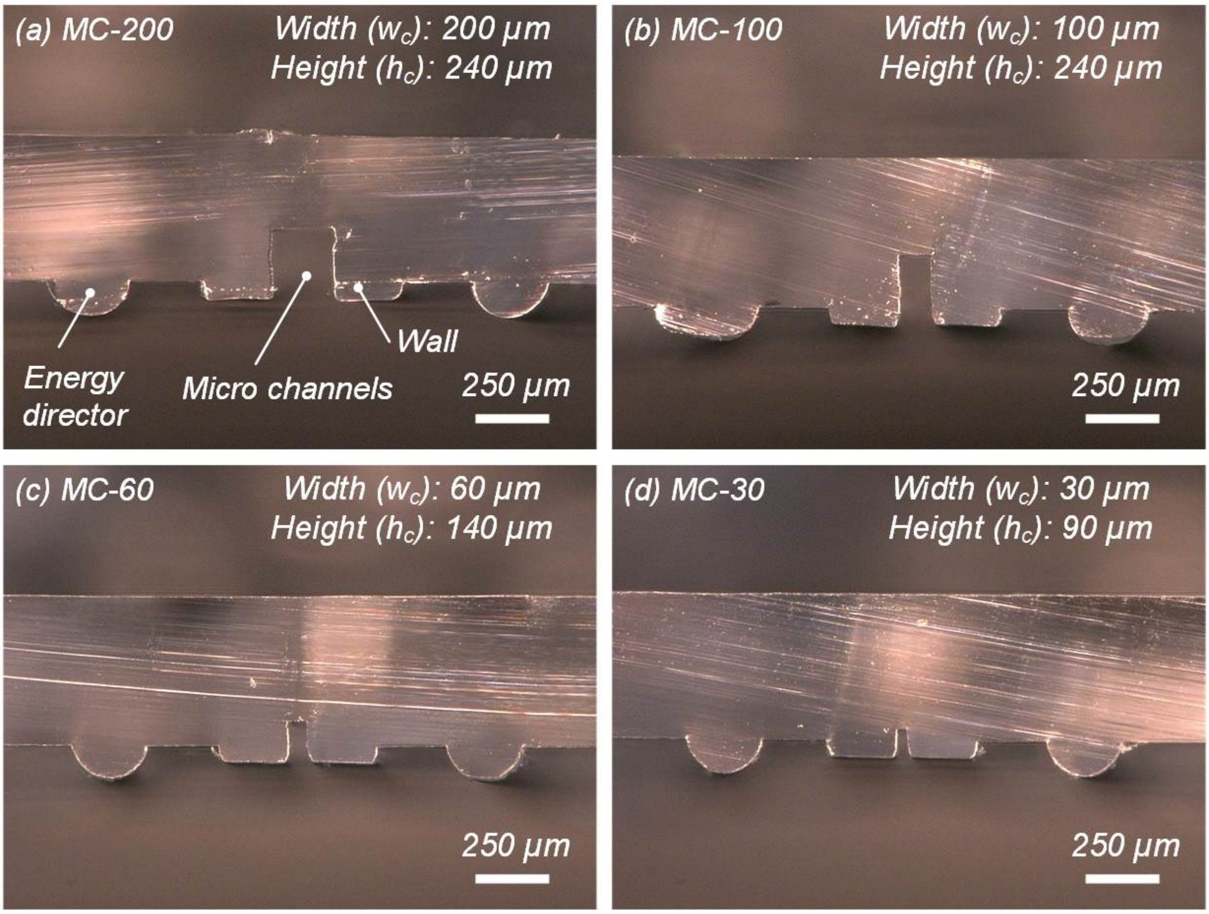

Figure 5.4: Cuts through ultrasonically thermoformed micro channels MC-200 (a), MC-100 (b), MC-60 (c), and MC-30 (d) with a width of 200 µm, 100 µm, 60 µm, and 30 µm, respectively.

5.3 Ultrasonic welding of the thermoformed foil

To generate enclosed micro channels and cavities, thermoformed foils were ultrasonically welded with a flat PET-G foil. In ultrasonic welding, only the lower tool was used. It was fixed on the anvil and the thermoformed foil (cf. Figure 5.3) was placed onto it. Pressing force, trigger force, peak-to-peak amplitude, welding time, cooling time, and holding force of ultrasonic welding were 1000 N, 950 N, 18 µm, 0.21 s, 0.2 s, and 600 N, respectively. A chip with enclosed micro channels and cavies was obtained.

Holes with a diameter of 1 mm were drilled on four cavities and semicircular channel before the ultrasonic welding. Five tubes with inner and outer diameters of 0.6 mm and 0.9 mm, respectively, were inserted into the holes. These tubes were glued to the chip.

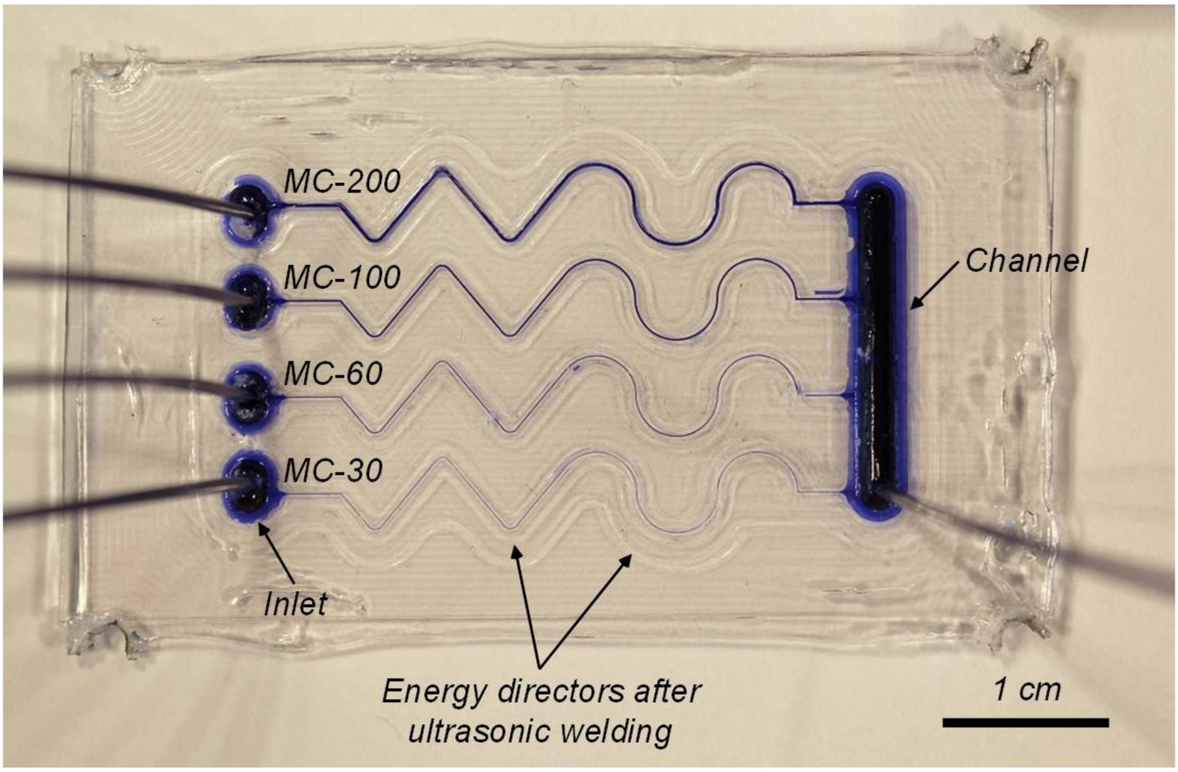

Figure 5.5: Photo of the chip with micro channels and cavities.

Figure 5.5 shows the chip with injected colored dyes. The four micro channels were filled with liquids without obvious leaking. The energy directors melted and bonded the thermoformed foil with the flat foil. In the meantime, clamping the two foils and enclosing the liquid in the micro channels and cavities. Ultrasonic welding enables bonding at lower temperatures minimizing the likelihood of collapsing or deforming a channel.

To examine the integrity of the thermoformed micro channels after ultrasonic welding, the cross-sections of the four micro channels were observed with the digital microscope, as shown in Figure 5.6. There is an interfacial gap between the two foils after ultrasonic welding because of the energy director. But with the help of the walls fully enclosed micro channels were generated. Besides, the micro channels were not deformed. As expected in Figure 5.1b, energy directors were melted but the walls were not melted during ultrasonic welding. The polymer melt from the melted energy director flowed to its two sides acting as a kind of glue bonding the two foils. The cross-sectional area of the energy directors was determined by its distance to the wall and the gap between the two welded foils. Too much melt would result in entering of the melt into the micro channel. The heights of the micro channels after ultrasonic welding were about 10 µm shorter than before. This indicates that the walls were contacted with the flat foil near the end of the ultrasonic vibrations, but the generated friction heat between them was insufficient to melt the wall. Hence, the walls were clamped to the flat foil after hardening of the melted energy directors.

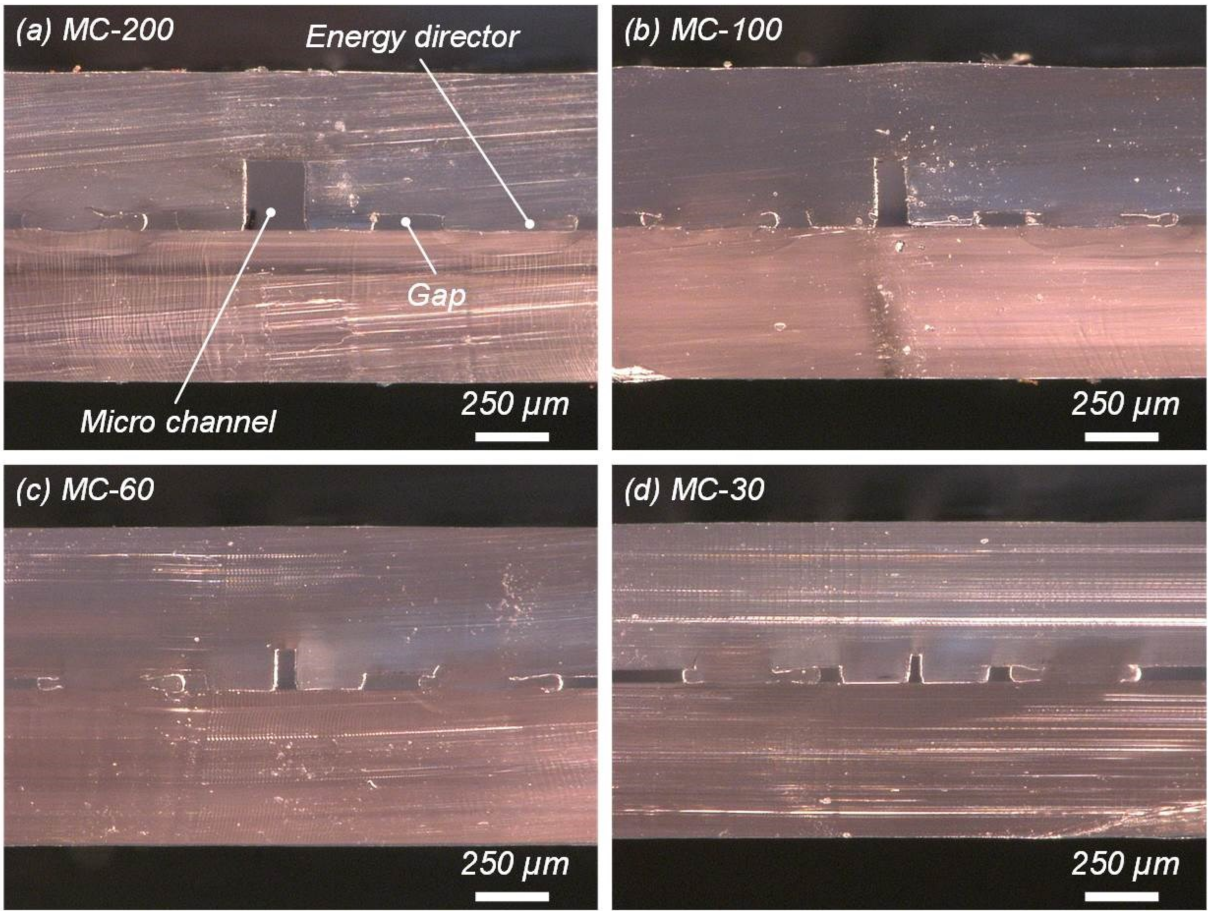

Figure 5.6: Cuts through the micro channels MC-200 (a), MC-100 (b), MC-60 (c), and MC-30 (d) after ultrasonic welding.

5.4 Micro channel testing

To evaluate the functionality of the micro channels on the chip, the micro channels were tested using colored dyes. Each micro channel consists of three different shapes: straight, zig-zag, and serpentine. Three positions were selected to observe, they were located at the intersection of the straight and zig-zag micro channel, zig-zag micro channel, and serpentine micro channel. Figure 5.7 shows the microscopic photos of these three different positions for each micro channel. Due to the narrow sizes of the micro channels, liquids were driven inside the micro channels via capillary force.

As shown in these photos, colored dyes filled micro channels without observable leaking. The energy directors on both sides of the micro channels were much wider than the walls after ultrasonic welding. Their boundaries were irregular and their distances to the wall were quite different. This is because the energy directors were melted and squeezed to their neighboring areas during the ultrasonic vibrations. After the hardening of the polymer melt, the thermoformed foil was bonded with the flat foil. The wall areas and energy directors looked alike, but the boundaries of the walls on both sides of the micro channels are straight and clear. This means that the walls were in close contact with the flat foil. The liquids inside the micro channels were thus confined in the micro channels and no observable colored dyes in other areas. As shown in Figure 5.7f, the wall also prevented the polymer melt from entering the micro channel.

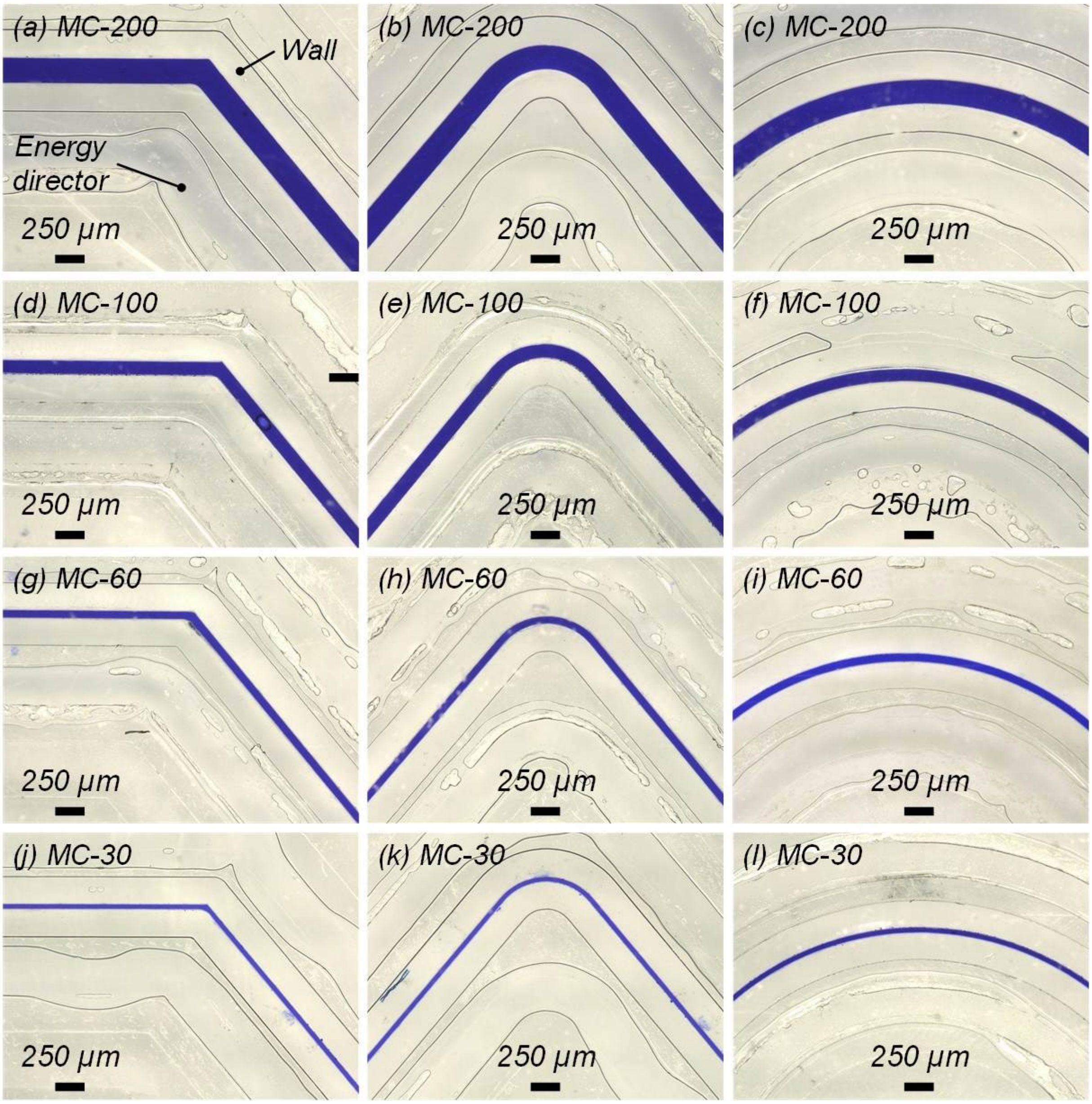

Figure 5.7: Photos of the micro channels on the chip injected with colored dyes. (a-c), (d-f), (g-i), and (j-l) are micro channels MC-200, MC-100, MC-60, and MC-30, respectively.

6 Ultrasonic fabrication of microdiaphragms

Microdiaphragms may be employed in mircophones. Their resonance frequency needs to be much larger than the highest frequency to be measured with the microphone. Therefore, it has been investigated whether microdiaphragms can be fabrictated by ultrasonic thermoforming.

Two types of microdiaphragms were ultrasonically fabricated. One is a single-layer PEEK hexagonal microdiaphragms fabricated by ultrasonic thermoforming with the aid of buffer foils. And the other one is thermoformed foils welded with a thin micromembrane. Then, the resonance frequency measurement setup and choice of measuring parameters were presented. Detected resonance frequencies and signal intensities were analyzed.

6.1 Tools for microdiaphragms

Tools with hexagonal, rectangular, and circular micro structures were milled into aluminum tools as shown in Figure 6.1, Figure 6.2, and Figure 6.3.

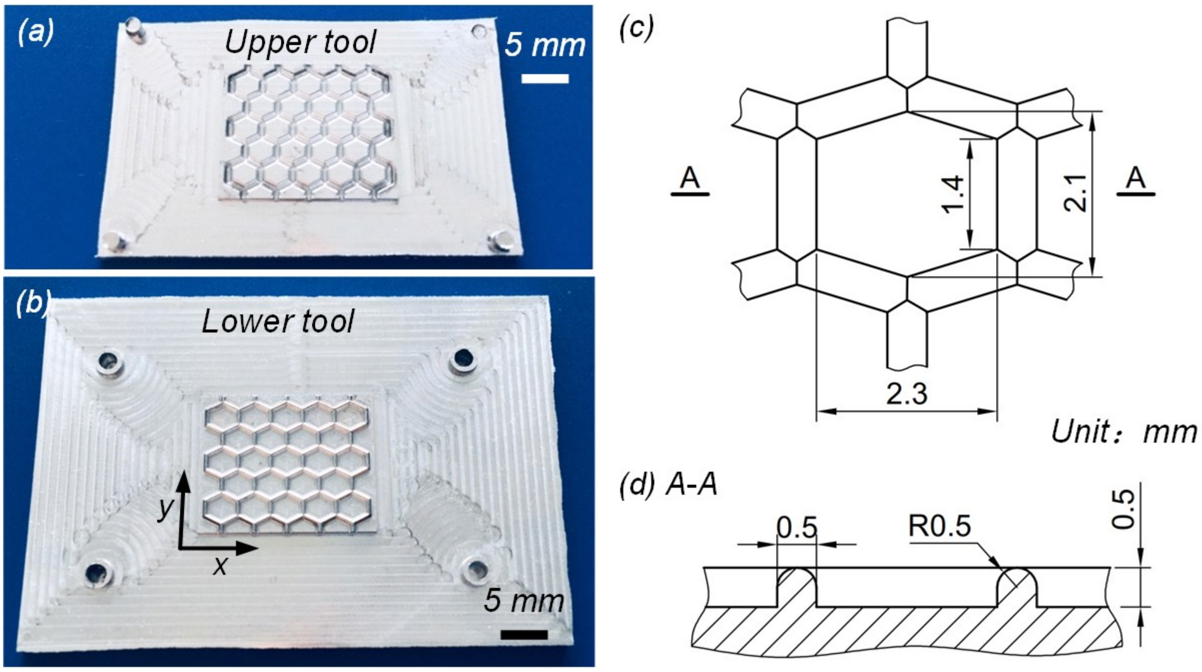

Figure 6.1: Upper tool (a) and lower tool (b) with hexagonal micro structures. The top view (c) and cross-sectional view (d) of hexagonal micro structures on the lower tool.

As shown in Figure 6.1a-b, 23 compactly arranged axisymmetric hexagons were evenly placed on a rectangle in the middle of the lower tool. Their dimensions are shown in Figure 6.1c-d, the corresponding length in x-direction and y-direction were 2.3 mm, and 2.1 mm, respectively. Each side of the hexagon on the lower tool was a protruding structure and its cross-section was a semi-circle attached to a rectangle. The width and height of the cross-section were both 0.5 mm.

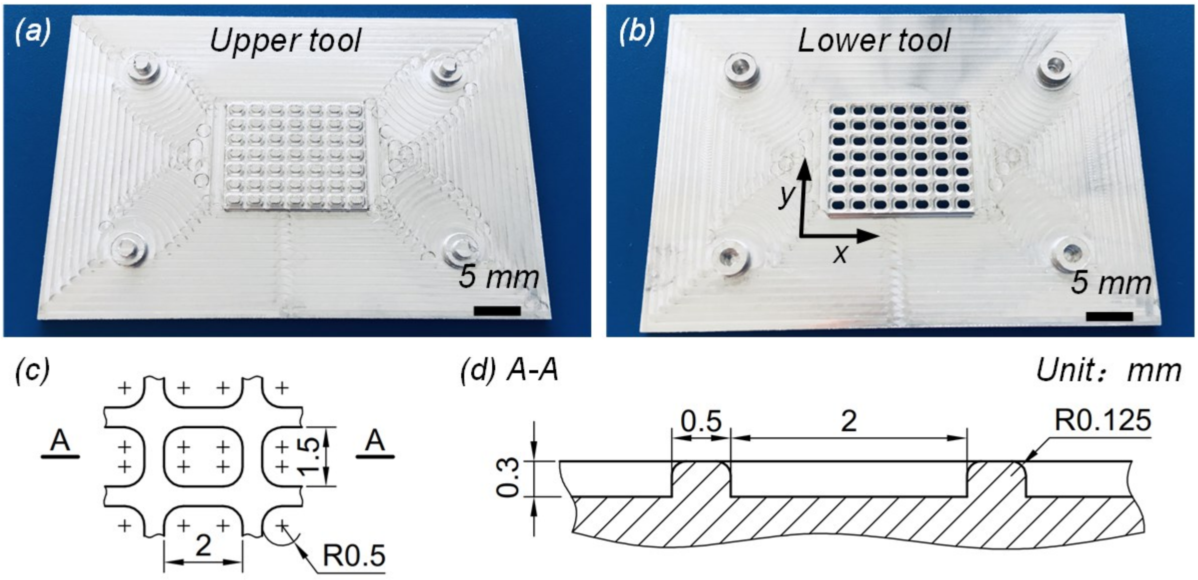

Figure 6.2: Upper tool (a) and lower tool (b) with rectangular micro structures. The top view (c) and cross-sectional view (d) of rectangular micro structures on the lower tool.

Figure 6.2 shows the tool pair with rectangular micro structures. Seven rows and seven columns of rounded rectangular micro structures were evenly placed on a rectangle in the middle of the lower tool. The width, height, and depth of each rounded rectangle were 2 mm, 1.5 mm, and 0.3 mm respectively. All four corners of the rectangles were rounded with radii of 0.5 mm. The distance between the sides of neighboring rectangles was 0.5 mm. All edges were rounded with a radius of 0.125 mm

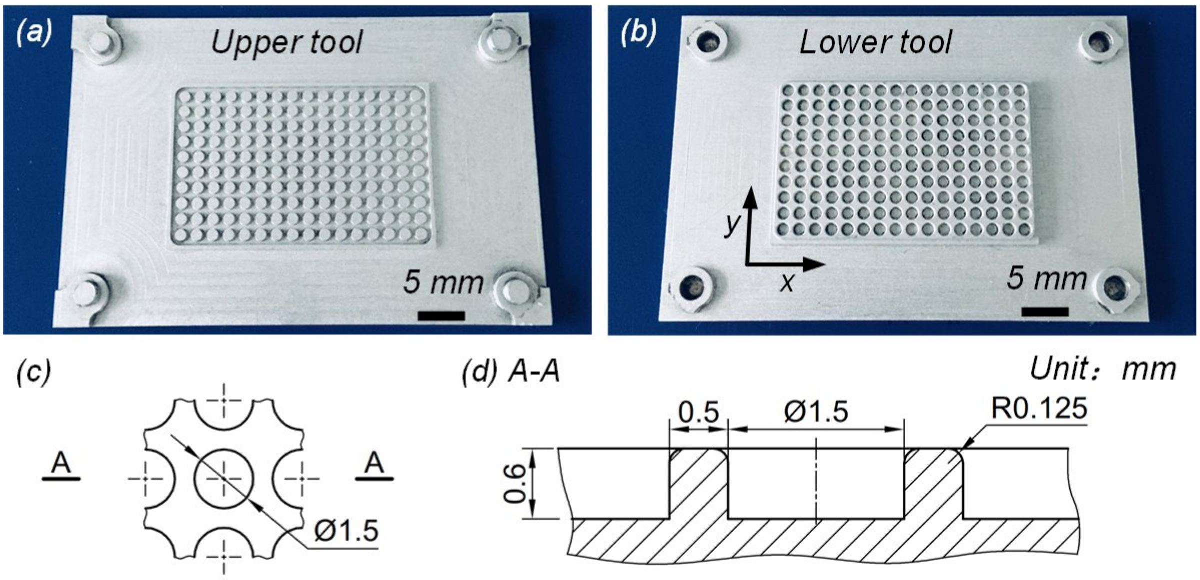

Figure 6.3: Upper tool (a) and lower tool (b) with circular micro structures. The top view (c) and cross-sectional view (d) of circular micro structures on the lower tool.

Figure 6.3a-b shows the tool pair with circular micro structures. Ten rows and sixteen columns of circular micro structures were evenly placed on a rectangle in the middle of the lower tool. As shown in Figure 6.3c-d, the diameter of the circle was 1.5 mm and the distance between the centers of neighboring circles was 2 mm. The edges were rounded with a radius of 0.125 mm.

The inverse micro structures were milled into the upper tool and all the edges were rounded with a radius of 0.25 mm. Four locating pins and holes located at the corners on the upper and lower tool were designed to align the tool pair during ultrasonic thermoforming.

6.2 Fabrication of microdiaphragms

6.2.1 Ultrasonic fabrication of microdiaphragms

A PEEK micromembrane with a thickness of 12 µm was used to ultrasonically thermoform the single layer microdiaphragms using tool pairs with hexagonal structures. It was sandwiched between two layers of 100-µm-thick PA 6 buffer foils during ultrasonic thermoforming. Pressing force, trigger force, peak-to-peak amplitude, welding time, cooling time, and holding force of ultrasonic thermoforming were 600 N, 300 N, 20 µm, 0.2 s, 2 s, and 600 N, respectively.

The composite microdiaphragms were composed of a base foil and a vibrating membrane. The base foil was ultrasonically thermoformed from two layers of 100-µm-thick PP foils using the tool pairs described in chapter 6.1. Then, it was ultrasonically welded with a 20-micron-thick PP vibrating membrane, as shown in Figure 6.4. Pressing force, trigger force, peak-to-peak amplitude, cooling time, and holding force of ultrasonic thermoforming were 600 N, 300 N, 20 µm, 2 s, and 600 N, respectively. The welding time for using tool pairs with rectangular structure and circular structure were 1.3 s and 0.9 s, respectively.

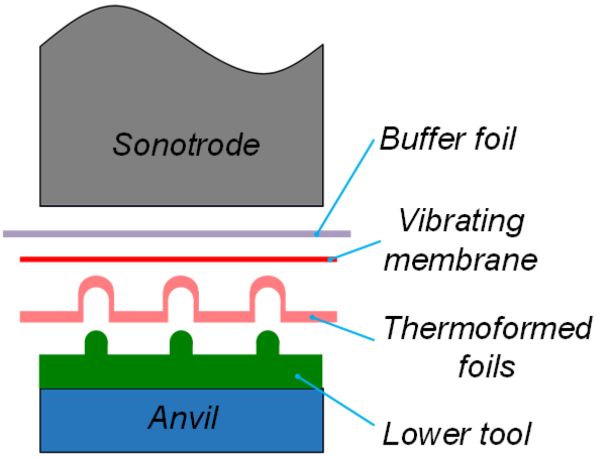

Figure 6.4: Placement of foils during ultrasonic welding of composite microdiaphragms.

For ultrasonic welding, peak-to-peak amplitude was 25 µm. The welding time and pressing force for using tool pairs with rectangular structure and circular structure were 0.29 s, 300 N, and 0.59 s, 500 N, respectively.

6.2.2 Sputtering of titanium layer

The sputtering system (Z 400 by Leybold Heraeus) was used for coating a layer of titanium on the thin vibrating membrane. The density, Young's modulus, and Poisson's ratio of titanium are 4.5 g/cm^3, 100 GPa, and 0.33, respectively. The power and argon flow during sputtering were 500 W and 90 sccm, respectively. The sputtering was several times resumed for 30 s after a pause of five minutes allowing the membrane to cool down.

6.3 Measurements

6.3.1 Measurement of the thickness of sputtered titanium layer

To calculate the resonance frequency of the titanium sputtered microdiaphragms, the thickness of the titanium layer was determined. The analytical balance (ALT 220-5DAM, KERN & Sohn GmbH, Germany) was used to measure the mass of the membranes before and after sputtering. The readability of this balance is 0.01 mg. The difference between the masses is the mass of the titanium layer. Thus, this mass difference divided by the density of titanium and the area of the sputtered membrane is the thickness of sputtered titanium layer.

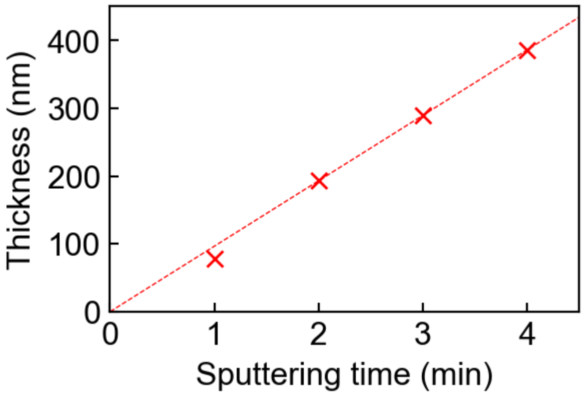

Figure 6.5: Thickness of titanium layer as a function of sputtering time.

Table 6.1: Sputtering time, the mass before and after sputtering, and the calculated thickness of the titanium layer.

Sputtering time [minute]	Mass before sputtering [g]	Mass after sputtering [g]	Area [mm^2]	Thickness [nm]
1	0.00863	0.00883	565.11	79
2	0.00863	0.00912	565.11	193
3	0.00863	0.00936	565.11	287
4	0.00863	0.00961	565.11	386

The masses of a 16.9 µm-thick PP membrane after sputtering for 1, 2, 3, and, 4 minutes were measured. Table 6.1 summarizes the masses before and after sputtering, the area of the membrane, and the calculated thickness of the titanium layer. Linear regression was carried out to correlate the thickness of the titanium layer and the sputtering time, as shown in Figure 6.5. From the calculated regression, 96.5 nm titanium was deposited per minute.

6.3.2 Resonance frequency measurement setup

The fabricated microdiaphragms were tested at different frequencies. An overview of the measurement setup is shown in Figure 6.6a. It consists of a measuring device, power supply, mixed signal oscilloscope, and function generator. As shown in Figure 6.6b, the measuring device is a hollow cylinder and there was a layer of soundproof foam on its inner walls to prevent noise from the outside. Inside of the cylinder, the microdiaphragms were fixed on one end between a piezo actuator and a microphone located at the other end.

The function generator (AFG 3022C, Tektronix, Inc., USA) generated an electrical signal with a preset frequency. This signal was a sine function. The piezo actuator converted this signal into mechanical vibrations. The tested microdiaphragms were thereby stimulated to resonate. Then, the signals emitted by microdiaphragms were detected by a microphone. A mixed signal oscilloscope (MSO 2014B, Tektronix, Inc., USA) was used to record the detected signals. After Fourier transform, the frequencies of the detected signal were obtained. In this device, the piezo actuator was a circular piezo disk (EPZ-27MS44W, EKULIT Elektrotechnik Karl-Heinz Mauz GmbH, Germany) made of brass and ceramic. Its resonance frequency and capacitance are 4.4 kHz and 21 pF, respectively.

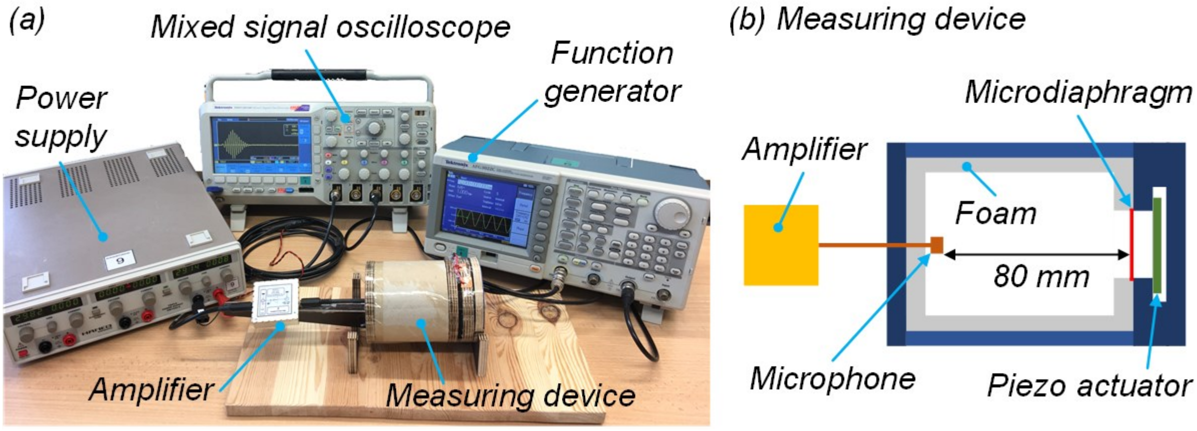

Figure 6.6: Resonance frequency measurement setup (a), and schematic of the measuring device (b).

The signal without microdiaphragms was measured with pulse frequency, amplitude, pulse cycles, and trigger interval of 12 kHz, 1 Vpp, 5, and 100 ms, respectively. The detected signal consists of three parts as shown in Figure 6.7. The first part of the detected signal was composed of the pulse signal from the piezo actuator. The piezo actuator did not stay still instantly after the pulse signal ended. So, the second part of the detected signal was selected after the pulse signal ended with an interval. After Fourier transform, the frequencies were obtained from the second part.

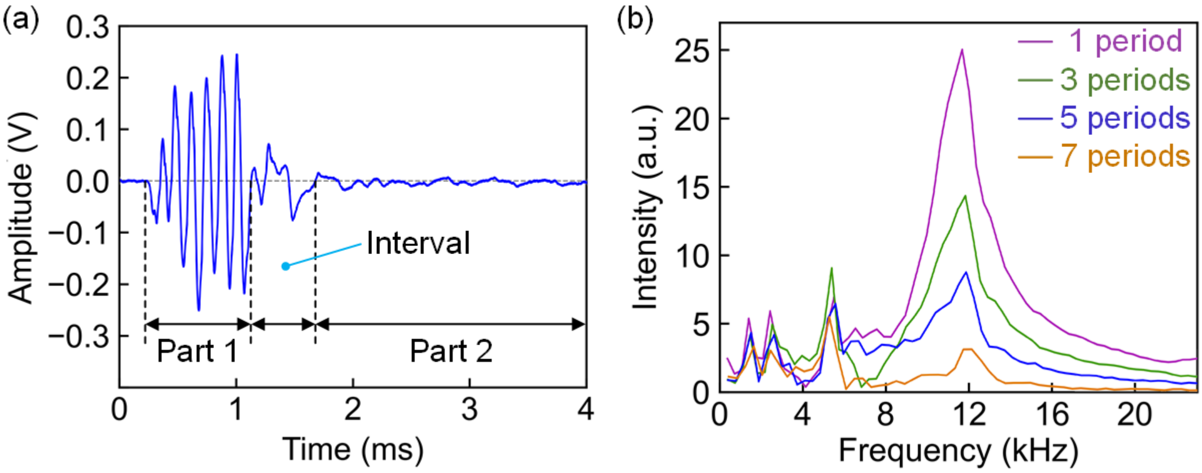

Figure 6.7: Detected signal without microdiaphragms (a) and its results of the second part after Fourier transform with an interval of 1, 3, 5 and, 7 periods after the end of the pulse signal (b).

To determine a suitable interval of the signal, the frequencies of the detected signal were analyzed after Fourier transform with different intervals. Figure 6.7b shows the frequencies of the second part after Fourier transform with an interval of 1, 3, 5 and, 7 periods after the end of the pulse signal. From left to right, there are four peaks near the frequencies of 1.5 kHz, 2.5 kHz, 5 kHz, and 12 kHz, respectively. The sources of the first two frequencies are unknown. The third peak near the frequency of 5 kHz is the resonance frequency of the piezo disk. The intensity of the fourth peak near the frequency of 12 kHz varied largely according to different intervals. With a longer interval, the intensity of the fourth peak attenuates to half of the third one. The piezo disk continued vibrating after the end of the pulse signal and its vibration decays over time. The resonance signal of the microdiaphragms are dwarfed by the vibration of the piezo disk after the pulse signal ends if the interval is too short. And are too weak to recognize its frequency if the interval is too long. Hence, an interval of five periods after the end of the pulse signal was adopted.

6.4 Resonance frequency of microdiaphragms

6.4.1 Single layer microdiaphragms

Single layer microdiaphragms were ultrasonically thermoformed with the help of buffer foils using the tool pair with hexagonal structures. Figure 6.8 shows the thermoformed microdiaphragms on a single PEEK layer and its cross-section. After thermoforming, the micromembranes were subdivided into smaller hexagonal microdiaphragms by micro-frames.

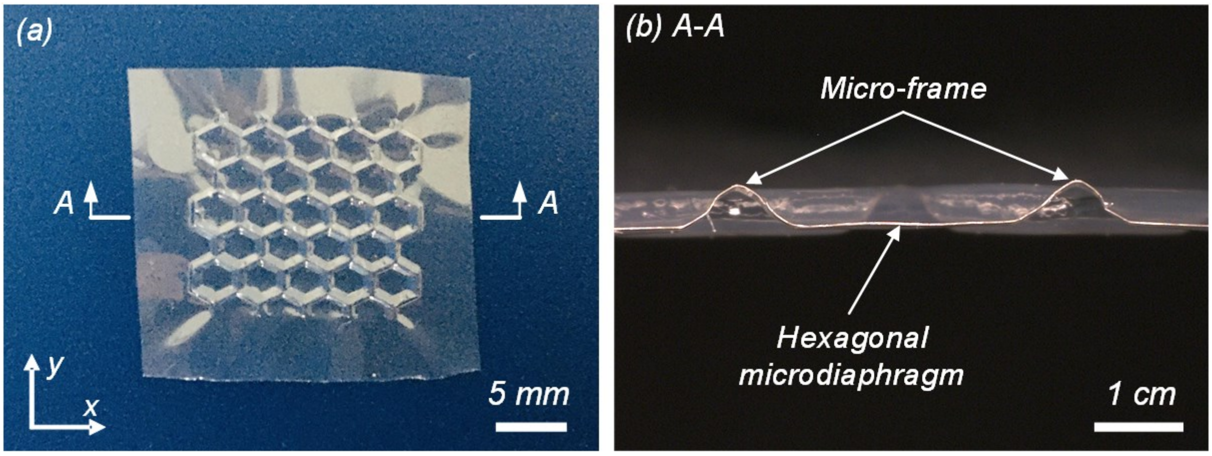

Figure 6.8: Single layer microdiaphragms (a) and a cross-section (b).

Since no equation was available for the resonance frequency of hexagonal membranes, as an approximation, Equation 6-1 [70] was used to predict the possible fundamental resonance frequency (f_{res}) of rectangular microdiaphragms and determine a range of pulse frequency for measurements. For the legth a_M and width b_M of the rectangle 2.3 mm and 2.1 mm were used.

$$f_{res} = \frac{\sqrt{3}}{\pi\sqrt{\rho_M}}\sqrt{\frac{1}{2}\frac{E_M}{1-v_M^2}d_M^2\left(\frac{7}{a_M^4}+\frac{4}{a_M^2 b_M^2}+\frac{7}{b_M^4}\right)+\left(\frac{\sigma_a}{a_M^2}+\frac{\sigma_b}{b_M^2}\right)} \tag{6-1}$$

where ρ_M, d_M, E_M, and v_M are the density, thickness, Young's modulus, and Poisson's ratio of the membrane. a_M and b_M denote the length of the microdiaphragm in two directions. σ_a and σ_b denote the stresses in these directions, respectively.

The density, thickness, Young's modulus, and Poisson's ratio of the PEEK membrane are 1.32 g/cm^3, 12 µm, 3.6 GPa, and 0.39, respectively. The stresses in the microdiaphragms are negligible. So, the fundamental resonance of the single-layer microdiaphragms was calculated to be 7417 Hz.

In measurements, pulse frequency, amplitude, pulse cycles, and trigger interval were 7400 Hz, 1 Vpp, 5, and 100 ms, respectively. Figure 6.9a shows the detected signals measured with single layer microdiaphragms, with the flat membrane, and without membrane. Their results after Fourier transform are shown in Figure 6.9b. The frequency of the peak of the signal measured with the single-layer microdiaphragms was 2250 Hz, the same as that without a membrane. It is quite different from the calculated one. Therefore, the single-layer microdiaphragms did not vibrate as expected. The possible reason is that the micro-frames were essentially flexible, and they are not stiff enough to support the vibration of the hexagonal microdiaphragms.

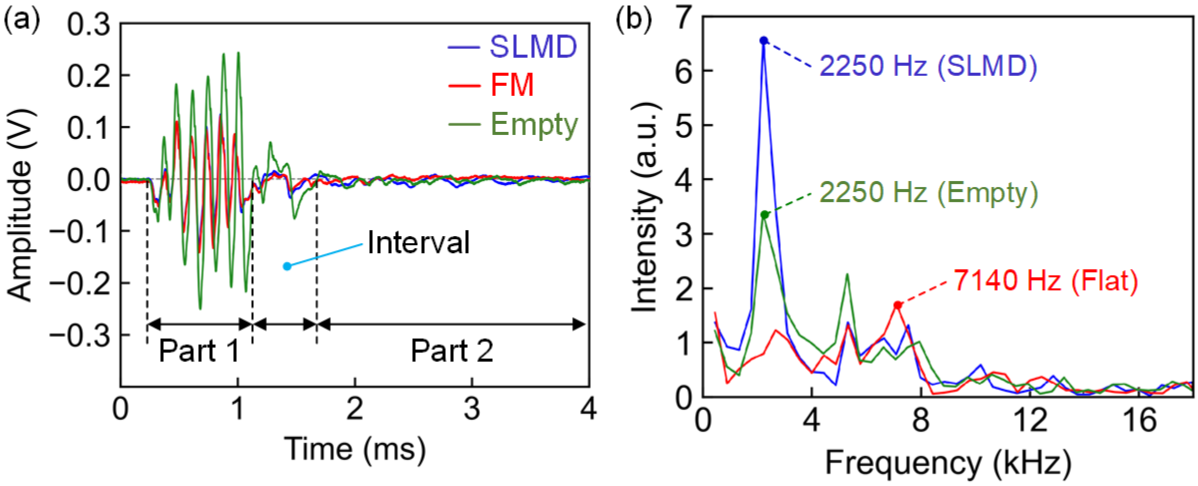

Figure 6.9: Detected signals (a) and their results after Fourier transform (b) of measurements with single layer microdiaphragms (SLMD), with the flat membrane, and without membrane.

6.4.2 Composite microdiaphragms

Since there was no desired resonance signal from the signal detected from the single-layer microdiaphragms, composite microdiaphragms were designed. Two layers of 100-µm-thick PP foils were ultrasonically thermoformed into a single foil with concave rectangular or circular structures to support the vibrating membrane. This thermoformed foil was ultrasonically welded with a 20-µm-thick PP vibrating membrane.

After ultrasonic welding, the base foil and the vibrating membrane were bonded together, and the latter was subdivided into rectangular or circular microdiaphragms. Then, onto the vibrating membrane there was sputtered a layer of titanium for two minutes. Figure 6.10a and Figure 6.10c show the photos of the composite microdiaphragms with rectangular and circular structures, respectively. The composite microdiaphragms were cut through their middle using a knife. Their cross-sections were observed with a digital microscope, as shown in Figure 6.10b and Figure 6.10d.

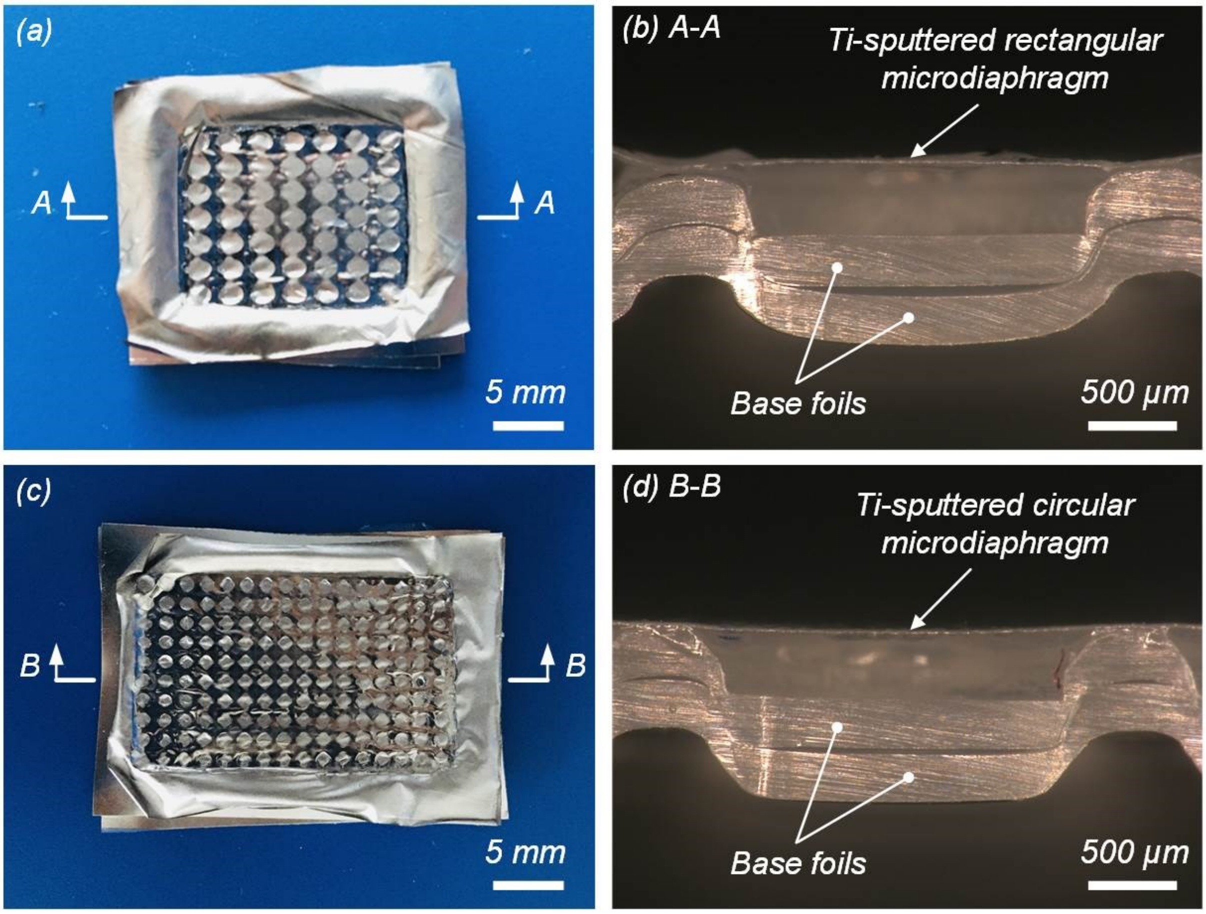

Figure 6.10: Photos and cuts through composite microdiaphragms with rectangular (a, b) and circular (c, d) structures.

Since Young's modulus and density of the vibrating membrane after sputtering are unknown, the exact fundamental resonance frequency cannot be calculated by equation 6-1. Therefore, a frequency range between 7 kHz and 23 kHz was assumed by the properties of PP and titanium, respectively. The vibration signals of the composite microdiaphragms were measured in this range in increments of 200 Hz. A Fourier transform was performed to analyze the resonance frequency of the detected signals. Two experiments were conducted at each pulse frequency. One is the 20-µm-thick PP membrane and a 100-µm-thick PP foil. The other is without a membrane.

Figure 6.11a shows the results of the detected signal of the composite rectangular microdiaphragms after the Fourier transform. Pulse frequency, amplitude, pulse cycles, and trigger interval of the measurements were 11600 Hz, 1 Vpp, 5, and 100 ms, respectively. There are peaks of about 2000 Hz and about 5000 Hz frequency in all these three measurements. The reason why these peaks appear is stated in chapter 6.3.2. The peak with a frequency of 11570 Hz appears only in the signal measured with the composite rectangular microdiaphragms.

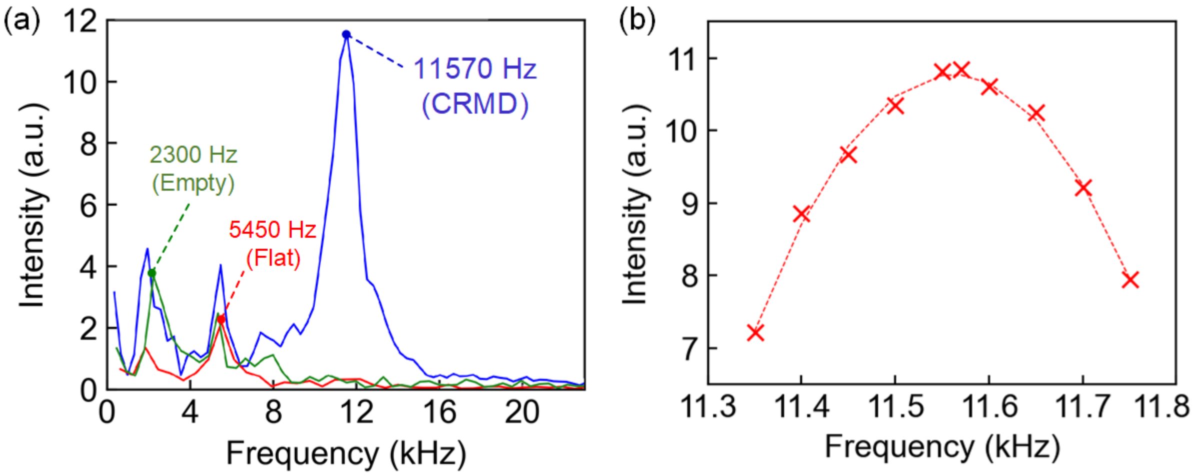

Figure 6.11: Measured with composite rectangular microdiaphragms (CRMD), results of detected signals after Fourier transform (a) and intensity of peak frequency concerning pulse frequency (b).

The results were roughly the same if the pulse frequency was varied between 11000 Hz and 12800 Hz. The frequency of the highest peak of the signal measured with the composite rectangular microdiaphragms changes with a change in pulse frequency. Their mean value and the standard deviation are 11570 Hz and 83 Hz, respectively. This resonance was only observed when the exciting frequency was in the range between 11 and 12.8 kHz.

The pulse frequency was varied from 11350 Hz to 11750 Hz in increments of 50 Hz to find out the exact resonance frequency of the composite rectangular microdiaphragms. Figure 6.11b shows the intensity of the highest frequency peak as a function of the pulse frequency. The maximum intensity is located at 11570 Hz. Therefore, this is the resonance frequency of the composite rectangular microdiaphragms.

For the composite circular microdiaphragms, signals were measured with pulse frequency, amplitude, pulse cycles, and trigger interval of 11800 Hz, 1 Vpp, 5, and 100 ms, respectively. Results of detected signals after Fourier transform and the intensity of the highest frequency peak as a function of pulse frequency are shown in Figure 6.12.

The peak with a frequency of 11650 Hz appears only in the signal measured with the composite rectangular microdiaphragms as shown in Figure 6.12a. The intensity of this peak frequency is much higher than that of the composite rectangular microdiaphragms (cf. Figure 6.11a) due to a larger quantity of the microdiaphragms. Similar to the composite rectangular microdiaphragms, the results with the pulse frequency range between 11200 Hz and 12800 Hz were roughly the same. The peak frequency also changes according to the pulse frequency. Their mean value and the standard deviation are 11650 Hz and 44 Hz, respectively. Outside the frequency range between 11200 Hz and 12800 Hz, there was no significant difference in the results of the measurements with or without microdiaphragms.

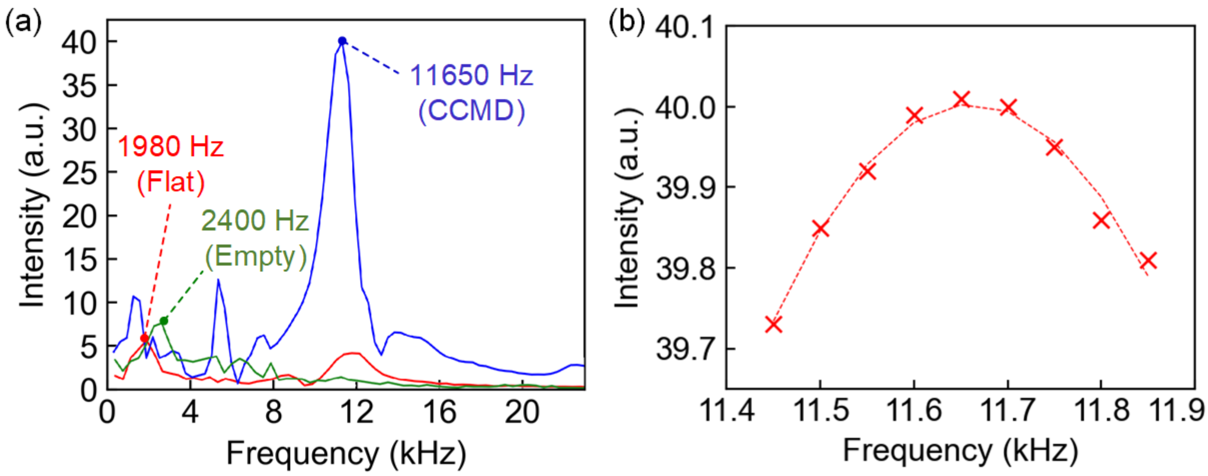

Figure 6.12: Measured with composite circular microdiaphragms (CCMD), results of detected signals after Fourier transform (a) and intensity of peak frequency concerning pulse frequency (b).

Signals with pulse frequency between 11450 Hz and 11850 Hz in increments of 50 Hz were measured further. Figure 6.12b shows the intensity of the highest peak frequency concerning pulse frequency, the maximum intensity was obtained at the frequency of 11650 Hz. The closer the pulse frequency is to this frequency, the larger is the intensive of the signal.

6.5 Influence of sputtering time on the resonance frequency

The influence of the thickness of the titanium layer on the resonance frequency of the composite microdiaphragms was also investigated. Composite circular microdiaphragms with Ti layer fabricated with four different sputtering times were measured. The thickness as a function of the sputtering time is shown in Table 6.1.

The vibration signals of the composite circular microdiaphragms were measured with the pulse frequency between 7 kHz and 23 kHz in increments of 200 Hz. The measurement was repeated five times at each pulse frequency. Within the pulse frequency range from 10.8 kHz to 12.4 kHz, the highest peak of resonance frequency near the pulse frequency appeared in the measurements of all four composite circular microdiaphragms. No obvious peak was found beyond this pulse frequency range.

Figure 6.13a shows the results of the detected signal of composite circular microdiaphragms after Fourier transform at the pulse frequency of 12 kHz. The resonance frequency of the composite circular microdiaphragms with a sputtering time of 1, 2, 3, and 4 minutes are 11560 ± 38 Hz, 11650 ± 44 Hz, 11760 ± 28 Hz, and 11820 ± 37 Hz, respectively. The intensity of the resonance signal increased with a longer sputtering time in the range of 1 to 3 minutes. But the intensity was much lower when the sputtering time was four minutes. This means that the intensity of the resonance signal was increased by increasing the thickness of the sputtered titanium layer in a certain range.

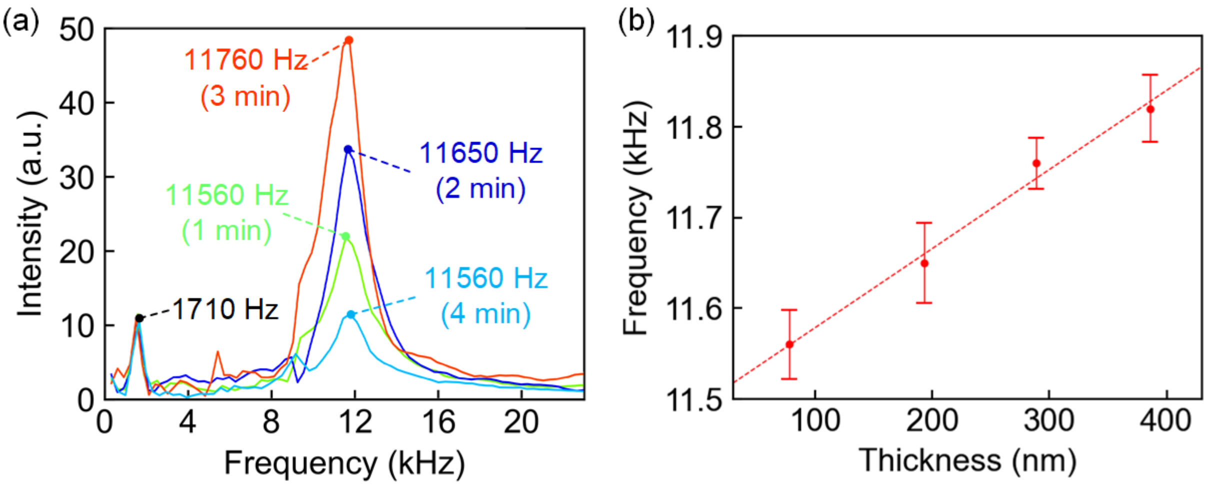

Figure 6.13: Resonance frequency measurements of composite circular microdiaphragms with four different sputtering times. Detected signal after Fourier transform (a) and intensity of peak frequency concerning pulse frequency (b).

As shown in Figure 6.13b, the resonance frequency of the microdiaphragms is proportional to the thickness of the titanium layer. A thicker titanium layer results a higher resonance frequency.

7 Conclusion and outlook

Ultrasonic thermoforming has been investigated by employing aluminum tool pairs with inverse microstructures. Layers from thermoplastic polymers were enclosed between these tools, heated by ultrasonic vibrations, and adapted to the shape of the microstructures. The process window was mainly determined by the tool temperature. Heating the tool is not necessary. But the process may become more independent of the ambient temperature and more reproducible if the tool temperature is kept constant.

The walls of structures on tools with a proper inclination angle prevented undesired punching of foils. Rounded corners of the concave tool can increase the minimum thickness of thermoformed structures, prevent potential fracture, and obtain a more uniform wall thickness distribution. A tool with an inclined wall and rounded corners let it accommodate to a varied thickness of foils to be thermoformed. Extra thin foils can also be thermoformed with the aid of buffer foils.

Rigid concave tools are preferable compared to flexible ones with respect to their ability to thermoform foils, whether from amorphous or semi-crystalline thermoplastics. Foils thermoformed by rigid tools have replicated the exact geometry of the tools. Parameters in ultrasonic thermoforming have less influence on wall thickness distribution compared to the shape of the tools. There was no obvious shrinkage of the polymer after the process. Flexible tools deformed according to the structures on the tool and resulted in concentrated thermal energy. This inhomogeneous distribution of force and heat hinders the practical application of flexible tools because foils were not well adapted to the shape of the tools.

Further investigations have shown that the tools and foils were heated differently with different installation locations of the tools. The tool fixed on the sonotrode got tens of degrees hotter than the one fixed on the anvil. Both tools got several degrees hotter if the convex tool has been fixed on the sonotrode compared to fixed on the anvil. On each tool, the temperature in the center was generally higher than in the surrounding area and the difference was about several degrees. The temperature of the thermoformed foils was not homogeneously distributed; it correlated to the shape of the structures.

With the integration of electrical elements, ultrasonically thermoformed foils could be welded to fabricate microsystems. This can be the integration of LEDs into a thermoformed foil with micro channels and cavities. The different dimensions, geometry, and connection of the thermoformed foil have shown that ultrasonic thermoforming is capable of generating complex three-dimensional micro structures. It was also shown that a flow sensor can be fabricated by ultrasonic thermoforming and welding. Since the heater and sensor wire inside the flow sensor needs to be positioned in a certain position, a specially shaped energy director was designed. This energy director not only served for bonding the two foils but also helped for positioning the integrated heater and sensor wires. It prevented fissuring of the 50 µm thin sensor wire during welding. Besides, fabricated an adaptable focus lens has shown that a foil can be thermoformed in a single step combined with other ultrasonic fabrication techniques. And two welded foils can be used as a single one for further ultrasonic welding process. The welding tool can avoid damaging three-dimensional structures on foils and hence it is indispensable for fabricating microsystems with thermoformed foils. Locating pins and holes allow to align micro structures on different foils.

In order to fabricate complex microfluidics, micro channels and cavities with different dimensions were developed. For this purpose, a special cross-section of micro channels was designed. There were walls with a height of tens of micrometers on both sides of the channels enclosing the channel after welding. Micro channels and cavities with different dimensions on a single foil and their welding to another foil has successfully been shown. Micro channels with different widths down to the smallest one, 30 µm and 90 µm in width and height, respectively, were achieved without polymer melt flow into the micro channels. It is expected that smaller micro channels can also be thermoformed and enclosed without cloging if tools with smaller features are available. This investigation has shown that structures with dimensions ranging from microns to tens of millimeters can be ultrasonically thermoformed into a single foil. Combined with specially designed micro channels and ultrasonic welding, more complex microsystems can be fabricated in a cycle time of tens of seconds.

A 20 µm-thick PEEK membrane was successfully thermoformed with the help of buffer foils. It was also shown that a 16 µm-thick PP membrane can be welded with a thermoformed foil. By welding with a thermoformed foil, a membrane was subdivided into microdiaphragms and resonated in a certain frequency range. But the resonance signal was too weak to be identified. Sputtering a layer of titanium helped obtaining a more intensive resonance signal. The frequency and intensity of the resonance signal were influenced by the thickness of the titanium layer.

References

[1] A. Illig, *Thermoformen in der Praxis*. 2008, München: Carl Hanser Verlag.

[2] J.L. Throne, J. Beine, *Thermoformen*. 1999, München: Hanser Verlag.

[3] S. Giselbrecht, T. Gietzelt, E. Gottwald, C. Trautmann, R. Truckenmüller, K.F. Weibezahn, A. Welle, *3D tissue culture substrates produced by microthermoforming of pre-processed polymer films.* Biomedical Microdevices, 2006. **8**(3): p. 191-199.

[4] C.Y. Chang, C.H. Yu, *A basic experimental study of ultrasonic assisted hot embossing process for rapid fabrication of microlens arrays.* Journal of Micromechanics and Microengineering, 2015. **25**(2).

[5] P. Khuntontong, T. Blaser, W.K. Schomburg, *Fabrication of molded interconnection devices by ultrasonic hot embossing on thin polymer films.* IEEE Transactions on Electronics Packaging Manufacturing, 2009. **32**(3): p. 152-156.

[6] L.Y. Cui, Z. Yang, C.J. Yang, Y.L. Tian, D.W. Zhang, *Fabrication of polymer optical diffusers by buffer-assisted ultrasonic embossing*, in *2015 International Conference on Manipulation, Manufacturing And Measurement on the Nanoscale*. 2015. p. 143-146.

[7] A. Tollkötter, J. Sackmann, T. Baldhoff, W.K. Schomburg, N. Kockmann, *Modular microreactor system made of ultrasonic hot embossed polymer foils.* Chemie Ingenieur Technik, 2015. **87**(6): p. 823-829.

[8] J. Li, C. Gerhardy, W.K. Schomburg, *Polymer circuit boards fabricated by ultrasonic hot embossing.* Journal of Micromechanics and Microengineering, 2013. **23**(7).

[9] J. Sackmann, K. Burlage, C. Gerhardy, B. Memering, S. Liao, W.K. Schomburg, *Review on ultrasonic fabrication of polymer micro devices.* Ultrasonics, 2015. **56**: p. 189-200.

[10] J. Sackmann, A. Barth, B. Memering, C. Gerhardy, W.K. Schomburg, *Ultrasonic fabrication of polymer micro devices*, in*: Proceedings Advances in Plastics Technology*. 2013: Sosnowiec, Poland. p. 550–557

[11] L. Hoehr, F. Reichmann, M. Berndt, J. Sackmann, N. Kockmann, W.K. Schomburg, *Ultrasonic fabrication of polymer plate reactors with a surface coating.* Chemical Engineering & Technology, 2019. **42**(5): p. 971-979.

[12] Y.J. Peng, W.K. Schomburg, *Process windows of ultrasonic thermoforming of micro structures.* Microsystem Technologies, 2020. **26**(9): p. 2777-2784.

[13] H.J. Bae, H.J. Lee, K. Park, *Ultrasonic assisted thermoforming for rapid fabrication of a microspeaker diaphragm.* Microsystem Technologies, 2017. **23**(6): p. 1677-1686.

[14] H.J. Lee, D.J. Shin, K. Park, *Ultrasonic thermoforming of a large thermoplastic polyurethane film with the aid of infrared heating.* Journal of Mechanical Science and Technology, 2017. **31**(12): p. 5687-5693.

[15] R. Truckenmuller, S. Giselbrecht, N. Rivron, E. Gottwald, V. Saile, A. van den Berg, M. Wessling, C. van Blitterswijk, *Thermoforming of film-based biomedical microdevices.* Advanced Materials, 2011. **23**(11): p. 1311-1329.

[16] M. Heilig, M. Schneider, H. Dinglreiter, M. Worgull, *Technology of micro-thermoforming of complex three-dimensional parts with multiscale features.* Microsystem Technologies, 2011. **17**(4): p. 593-600.

[17] H. Mekaru, T. Yano, *Comparative evaluation of detachable mold fixing methods aimed at low energy loss for ultrasonic nanoimprint lithography.* Microsystem Technologies, 2017. **23**(7): p. 2707-2717.

[18] J. Kosloh, J. Sackmann, S. Krabbe, W.K. Schomburg, *Measurement of temperature and pressure distribution during ultrasonic processes by sensor foils from polyvinylidene fluoride.* Microsystem Technologies, 2018. **24**(9): p. 3729-3740.

[19] S.K. Bhudolia, G. Gohel, K.F. Leong, A. Islam, *Advances in ultrasonic welding of thermoplastic composites: a review.* Materials, 2020. **13**(6).

[20] I.F. Villegas, *Ultrasonic welding of thermoplastic composites.* Frontiers in Materials, 2019. **6**: p. 10.

[21] H.P.C. Daniels, *Ultrasonic welding.* Ultrasonics, 1965. **3**(4): p. 190-196.

[22] M.J. Troughton, *Handbook of Plastics Joining : a practical guide*. 2008, William Andrew Inc.: Norwich, NY, USA. p. 15–35.

[23] M.N. Tolunay, P.R. Dawson, K.K. Wang, *Heating and bonding mechanisms in ultrasonic welding of thermoplastics.* Polymer Engineering and Science, 1983. **23**(13): p. 726-733.

[24] Z.B. Zhang, X.D. Wang, Y. Luo, Z.Q. Zhang, L.D. Wang, *Study on heating process of ultrasonic welding for thermoplastics.* Journal of Thermoplastic Composite Materials, 2010. **23**(5): p. 647-664.

[25] A. Levy, S. Le Corre, I.F. Villegas, *Modeling of the heating phenomena in ultrasonic welding of thermoplastic composites with flat energy directors.* Journal of Materials Processing Technology, 2014. **214**(7): p. 1361-1371.

[26] H.J. Lee, K. Park, *Variable wettability control of a polymer surface by selective ultrasonic imprinting and hydrophobic coating.* Colloid And Polymer Science, 2016. **294**(9): p. 1413-1423.

[27] R. Šakalys, G. Janušas, A. Palevičius, E. Čekas, V. Jūrėnas, A. Sodah, *Micro-structures replication using high frequency excitation.* Microsystem Technologies, 2016. **22**(7): p. 1831-1843.

[28] R. Truckenmüller, Z. Rummler, T. Schaller, W.K. Schomburg, *Low-cost thermoforming of micro fluidic analysis chips.* Journal Of Micromechanics And Microengineering, 2002. **12**(4): p. 375-379.

[29] J.H. Liu, X.D. Chen, S.P. Diao, *Ultrasonic vibration technology for the polymer replication of high aspect ratio micro-structured surface.* Microsystem Technologies, 2018. **24**(5): p. 2253-2264.

[30] N. Okulova, P. Johansen, L. Christensen, R. Taboryski, *Effect of structure hierarchy for superhydrophobic polymer surfaces studied by droplet evaporation.* Nanomaterials, 2018. **8**(10).

[31] J. Liu, Z. Wang, P. Zeng, M. Song, W. Huang, Z. Liu, Z. Xu, J. Li, C. Liu, Y. Jiang, *Direct casting of a PDMS substrate holder from a structured polymer film for lab-on-a-foil bonding.* Sensors and Actuators B-Chemical, 2018. **266**: p. 570-576.

[32] V. Kappings, C. Gruen, D. Ivannikov, I. Hebeiss, S. Kattge, I. Wendland, B.E. Rapp, M. Hettel, O. Deutschmann, U. Schepers, *vasQchip: A novel microfluidic, artificial blood vessel scaffold for vascularized 3D tissues.* Advanced Materials Technologies, 2018. **3**(4).

[33] H. Dreuth, C. Heiden, *Thermoplastic structuring of thin polymer films.* Sensors and Actuators A-Physical, 1999. **78**(2-3): p. 198-204.

[34] R. Truckenmüller, S. Giselbrecht, C. van Blitterswijk, N. Dambrowsky, E. Gottwald, T. Mappes, A. Rolletschek, V. Saile, C. Trautmann, K.F. Weibezahn, A. Welle, *Flexible fluidic microchips based on thermoformed and locally modified thin polymer films.* Lab on a Chip, 2008. **8**(9): p. 1570-1579.

[35] M. Focke, D. Kosse, C. Müller, H. Reinecke, R. Zengerle, F. von Stetten, *Lab-on-a-Foil: microfluidics on thin and flexible films.* Lab on a Chip, 2010. **10**(11): p. 1365-1386.

[36] A. Jungmeier, *The effect of pressure and temperature on microthermoforming thermoplastic films integrated in the injection moulding process.* Journal Of Polymer Engineering, 2016. **36**(6): p. 597-605.

[37] P. Nagarajan, D.G. Yao, *Uniform shell patterning using rubber-assisted hot embossing process. I. experimental.* Polymer Engineering and Science, 2011. **51**(3): p. 592-600.

[38] H. Bae, K. Park, *Design and analysis of ultrasonic horn for polymer sheet forming.* International Journal of Precision Engineering and Manufacturing-Green Technology, 2016. **3**(1): p. 49-54.

[39] J.-H. Park, K. Park, *Development of micropatterns on curved surfaces using two-step ultrasonic forming.* Micromachines, 2019. **10**(10).

[40] J. Kosloh, J. Sackmann, R. Šakalys, S. Liao, C. Gerhardy, W.K. Schomburg, *Heat generation and distribution in the ultrasonic hot embossing process.* Microsystem Technologies, 2017. **23**(5): p. 1411-1421.

[41] X. Liang, X.Y. Wu, K. Zeng, B. Xu, S.Y. Wu, H. Zhao, B. Li, S.C. Ruan, *Micro ultrasonic powder molding for semi-crystalline polymers.* Journal of Micromechanics and Microengineering, 2014. **24**(4).

[42] H. Bae, H.-J. Lee, K. Park, *Effect of vibration transmission direction in ultrasonic thermoforming on the formability of micro-corrugations.* International Journal of Precision Engineering and Manufacturing, 2017. **18**(5): p. 697-703.

[43] Y.Z. Chen, H.L. Li, *Effect of ultrasound on the viscoelasticity and rheology of polystyrene extruded through a slit die.* Journal of Applied Polymer Science, 2006. **100**(4): p. 2907-2911.

[44] J. Lu, Y.B. Qiang, W.Q. Wu, B.Y. Jiang, *Effects of the processing parameters on the shear viscosity of cyclic olefin copolymer plasticized by ultrasonic vibration Energy.* Polymers, 2020. **12**(3).

[45] S. Gao, Z.J. Qiu, J.H. Ouyang, *The improvement effect and mechanism of longitudinal ultrasonic vibration on the injection molding quality of a polymeric micro-needle array.* Polymers, 2019. **11**(1).

[46] J. Chen, Y. Chen, H. Li, S.-Y. Lai, J. Jow, *Physical and chemical effects of ultrasound vibration on polymer melt in extrusion.* Ultrasonics Sonochemistry, 2010. **17**(1): p. 66-71.

[47] W. Zou, W.K. Schomburg, *Friction embossing.* Microsystem Technologies, 2020. **26**(8): p. 2729-2737.

[48] T. Runge, J. Sackmann, W.K. Schomburg, L.M. Blank, *Ultrasonically manufactured microfluidic device for yeast analysis.* Microsystem Technologies, 2017. **23**(6): p. 2139-2144.

[49] J. Bavendiek, P. Maurer, S. Graeber, A. Pasch, W.K. Schomburg, W. Jahnen-Dechent, *Rapid calcification propensity testing in blood using a temperature controlled microfluidic polymer chip.* Plos One, 2020. **15**(4).

[50] P. Khuntontong, T. Blaser, W.K. Schomburg. *Ultrasonic micro hot embossing of polymers exemplified by a micro thermal flow sensor*. in *2nd European Conference & Exhibition on Integration Issues of Miniaturized Systems - MOMS, MOEMS, ICS and Electronic Components*. 2008.

[51] W.K. Schomburg, K. Burlage, C. Gerhardy, *Ultrasonic hot embossing.* Micromachines, 2011. **2**(2): p. 157-166.

[52] S.S. Karabeyoglu, O. Ekşi, S. Erdoğan, *An experimental study on wall thickness distribution in thermoforming.* Advances in Science and Technology-Research Journal, 2017. **11**(3): p. 139-142.

[53] E.S. Erdogan, O. Eksi, *Prediction of wall thickness distribution in simple thermoforming moulds.* Strojniski Vestnik-Journal of Mechanical Engineering, 2014. **60**(3): p. 195-202.

[54] J. Canny, *A computational approach to edge detection.* IEEE Transactions on Pattern Analysis and Machine Intelligence, 1986. **8**(6): p. 679-698.

[55] R. McCool, P.J. Martin, *The role of process parameters in determining wall thickness distribution in plug-assisted thermoforming.* Polymer Engineering and Science, 2010. **50**(10): p. 1923-1934.

[56] C.J. Nonhof, G.A. Luiten, *Estimates for process conditions during the ultrasonic welding of thermoplastics.* Polymer Engineering and Science, 1996. **36**(9): p. 1177-1183.

[57] G. Palardy, H.J. Shi, A. Levy, S. Le Corre, I.F. Villegas, *A study on amplitude transmission in ultrasonic welding of thermoplastic composites.* Composites Part a-Applied Science and Manufacturing, 2018. **113**: p. 339-349.

[58] F. Ejeian, S. Azadi, A. Razmjou, Y. Orooji, A. Kottapalli, M.E. Warkiani, M. Asadnia, *Design and applications of MEMS flow sensors: A review.* Sensors and Actuators A, 2019. **295**: p. 483-502.

[59] J. Kim, H. Cho, S.I. Han, A. Han, K.H. Han, *A disposable microfluidic flow sensor with a reusable sensing substrate.* Sensors and Actuators B, 2019. **288**: p. 147-154.

[60] T.E. Miller, H. Small, *Thermal pulse time-of-flight liquid flow meter.* Analytical Chemistry, 1982. **54**(6): p. 907-910.

[61] M. Ashauer, H. Glosch, F. Hedrich, N. Hey, H. Sandmaier, W. Lang, *Thermal flow sensor for liquids and gases*. Micro Electro Mechanical Systems - IEEE Eleventh Annual International Workshop Proceedings. 1998. 351-355.

[62] C. Gerhardy, W.K. Schomburg, *Time of flow sensor with a flow parallel wire.* Sensors and Actuators A, 2012. **186**: p. 105-110.

[63] J.O. Wilkes, *Fluid mechanics for chemical engineers, 2nd ed., with microfluidics and CFD*. 2006, Pearson Education, Inc.: Upper Saddle River, NJ, USA. p. 109–117.

[64] L. Wang, J.P. Duan, B.Z. Zhang, W.J. Wang, *Variable-focus liquid lens integrated with a planar electromagnetic actuator.* Micromachines, 2016. **7**(10).

[65] L.H. Wang, M. Ishikawa, *Dynamic Response of Elastomer-Based Liquid-Filled Variable Focus Lens.* Sensors, 2019. **19**(21).

[66] J.H. Wang, W.P. Tang, L.Y. Li, L. Xiao, X. Zhou, Q.H. Wang, *Hybrid driving variable-focus optofluidic lens.* Optics Express, 2019. **27**(24).

[67] X. Huang, S.Y. Lin, D.D. Gu, Z.X. Bu, W.J. Yi, P.Q. Xie, L.Y. Wang, *Review on progress of variable-focus liquid lens.* Chinese Optics, 2019. **12**(6): p. 1179-1194.

[68] M. Agarwall, R.A. Gunasekaran, P. Coane, K. Varahramyan, *Polymer-based variable focal length microlens system.* Journal of Micromechanics and Microengineering, 2004. **14**(12): p. 1665-1673.

[69] Y. Luo, S.Q. He, L.J. Wang, Z.B. Zhang, *Study on ultrasonic fusion bonding for polymer microfluidic chips*, in *Mems/Nems Nano Technology*, X.H. Wang, Editor. 2011. p. 311-315.

[70] W.K. Schomburg, *Introduction to Microsystem Design*. 2015: Springer Berlin Heidelberg.